Temporal and Spatio-temporal Regimes of Generation of Raman Fibre Lasers

Nikita Stanislavovich Tarasov

Doctor of Philosophy

ASTON UNIVERSITY

September 2015

Aston University

Temporal and Spatio-temporal Regimes of Generation of Raman Fibre Lasers

Nikita Tarasov

Doctor of Philosophy

September 2015

Temporal dynamics of Raman fibre lasers tend to have very complex nature, owing to great cavity lengths and high nonlinearity, being stochastic on short time scales and quasi-continuous on longer time scales. Generally fibre laser intensity dynamics is represented by one-dimensional time-series, which in case of quasi-continuous wave generation in Raman fibre lasers gives little insight into the processes underlying the operation of a laser. New methods of analysis and data representation could help to uncover the underlying physical processes, understand the dynamics or improve the performance of the system.

Using intrinsic periodicity of laser radiation, one dimensional intensity time series of a Raman fibre laser was analysed over fast and slow variation time. This allowed to experimentally observe various spatio-temporal regimes of generation, such as laminar, turbulent, partial mode-lock, as well as transitions between them and identify the mechanisms responsible for the transitions.

Great cavity length and high nonlinearity also make it difficult to achieve stable high repetition rate mode-locking in Raman fibre lasers. Using Faraday parametric instability in extremely simple linear cavity experimental configuration, a very high order harmonic mode-locking was achieved in 2.2 km long Raman fibre laser. The maximum achieved pulse repetition rate was 12 GHz, with 7.3 ps long Gaussian shaped pulses.

There is a new type of random lasers – random distributed feedback Raman fibre laser, which temporal properties cannot be controlled by conventional mode-locking or Q-switch techniques and mechanisms. By adjusting the pump configuration, a very stable pulsed operation of random distributed feedback Raman fibre laser was achieved. Pulse duration varied in the range from 50 to 200 μs depending on the pump power and the cavity length. Pulse repetition rate scaling on the parameters of the system was experimentally identified.

Additional keywords and phrases: Nonlinear optics, turbulence, mode-locking, ultrashort pulses, analysis.

Aknowledgements

I would like to thank my supervisor Professor Sergei Konstantinovich Turitsyn, who gave me this great opportunity to work under his supervision. His strong and charismatic personality was an inspiration for me during these years. He shared his vision, passion, wisdom and experience, which contributed greatly to shaping me as a researcher.

I would also like to thank my co-supervisor Dr. Dmitry Churkin, who guided me through these three years, giving constant feedback, direction, and advice. He has been an exemplary researcher, teacher and colleague.

I would like to thank my friends and colleagues Srikanth Sugavanam and Auro Perego, with whom we worked in the lab and had many productive discussion over the years. My special thanks go to all of the Aston Institute of Photonic Technologies members for the great working environment and help and support provided.

Contents

List of Figures

List of Tables

List of Abbreviations

ACF auto-correlation function. 51, 63–65, 76, 79, 83, 86, 92

CW continuous wave. 24, 49, 59, 94

EDFL erbium-doped fibre laser. 27

FBG fibre Bragg grating. 18, 20, 21, 37, 39, 40, 55, 60, 66–69, 72, 81, 84–87

FWHM full width at half maximum. 55, 71, 73, 76, 77, 87

FWM four-wave mixing. 72

GVD group velocity dispersion. 22, 27, 42

MI modulation instability. 54, 73, 77, 87

MR Mamyshev Regenerator. 35, 79–81, 84–87

NA numerical aperture. 36, 44

NALM nonlinear amplifying loop mirror. 7, 30, 31

NLSE nonlinear Schrödinger equation. 6, 21, 23, 41–43, 45, 48, 54, 57

NOLM nonlinear optical loop mirror. 7, 30, 31

NPE nonlinear polarisation evolution. 7, 31, 32

PDF probability density function. 7, 11, 56, 60, 61, 91–93

PM polarisation maintaining. 40

PSR pulse-shortening rate. 27

RDFL random distributed feedback fibre laser. 7, 36–44, 90, 92–95, 98, 99

RF radio frequency. 10, 11, 25, 50, 72, 79, 83, 84, 88, 92, 93, 96

RFL Raman fibre laser. 58–60, 65, 72

RIN relative intensity noise. 55, 60, 93

SHG second harmonic generation. 74, 82, 86

SPM self-phase modulation. 31, 35, 79, 81

WDM wavelength-division multiplexing. 31, 55, 60, 66, 67, 90

XPM cross-phase modulation. 31, 44, 55

Chapter 1

Introduction

Raman fibre lasers have unique and attractive properties such as the ability to operate at any desired wavelength, high gain bandwidth and quantum efficiency. However, generally a high fibre length is required leading to high total nonlinearity and dispersion, which makes it difficult to achieve and control the desired temporal properties of the radiation. The motivation for this work is to developed methods of analysis and control of the temporal properties of radiation from Raman fibre lasers, to open new possibilities for practical applications.

This work is structured in the following way. In the beginning a general introduction into Raman fibre lasers will be given, with an overview of mode-locking, random distributed feedback Raman fibre lasers, electro-acoustic response in optical fibres and spatio-temporal representation of laser radiation. In the second part spatio-temporal treatment of the laser radiation will be introduced as a method which allows one to follow the evolution of any structures in the radiation over fast time and slow time scales. Using this method various spatio-temporal regimes of generation of Raman fibre lasers were experimentally identified and described. In the third part, novel methods of pattern generation and stabilisation in Raman fibre lasers will be proposed and experimentally demonstrated, with harmonic mode-locking operation in a simple environmentally stable configuration. In the final part temporal dynamics of random distributed feedback Raman fibre lasers, and methods of their control will be presented.

1.1 Raman Fibre Lasers

1.1.1 Raman Gain

Raman scattering is an inelastic scattering process in which a small fraction of incident photons in molecular medium downshift in frequency by the amount dependent on the vibrational levels of the medium. The process was first discovered by Raman in 1928 [2]. The schematic diagram of the process is shown on the Figure 1.1a. The photons with energy $\hbar\omega_{\mathrm{p}}$ excite molecules to the virtual upper state, from which they decay into one of the vibrational modes and emit a so called Stokes photon with the energy $\hbar\omega_{\mathrm{s}}$. It is also possible that a molecule in one of the vibrational states absorbs a pump photon and through a virtual state decays to the ground state emitting an upshifted in frequency anti-Stokes photon with the energy $\hbar\omega_{\mathrm{as}}$. The rate of this process depends on the temperature of the medium as the population of the vibrational states is described by the Boltzmann equation

$$\frac{N_V}{N_G} = \exp\left(-\frac{\hbar\left(\omega_{\mathrm{as}} - \omega_{\mathrm{p}}\right)}{kT}\right) \tag{1.1}$$

where N_V – is the population of the vibrational state, N_G – is the population of the ground state, k – is the Bolzmann constant, and T – is the temperature of the medium.

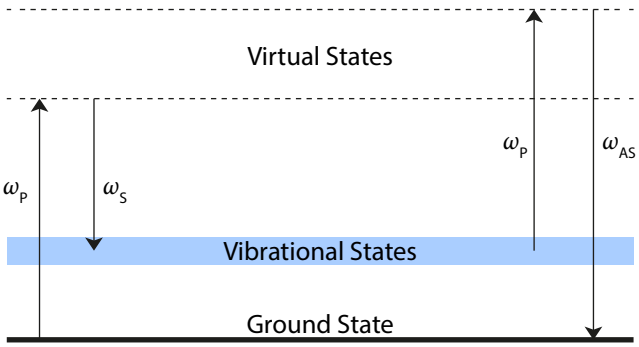

Figure 1.1: a, Diagram of spontaneous Raman scattering. A pump photon with energy $\hbar\omega_{\mathrm{p}}$ excites a molecule from the ground state (for Stokes) or from a vibrational state (for anti-Stokes) to a virtual state, and a Stokes shifted photon with energy $\hbar\omega_{\mathrm{s}}$ or anti-Stokes photon with energy $\hbar\omega_{\mathrm{as}}$ is created when the molecule decays to a vibrational or ground state.

In amorphous materials like fused silica vibrational states broaden and overlap creating

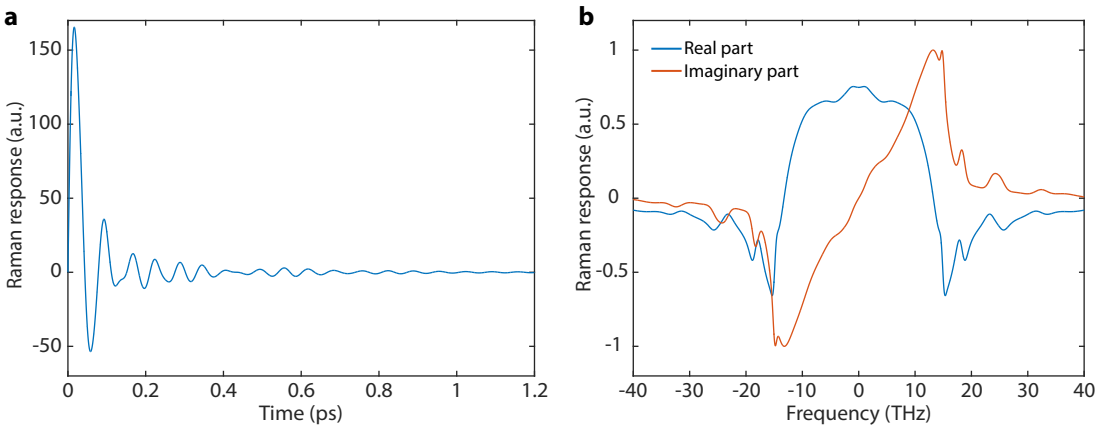

Figure 1.2: a, Raman response function of silica fibre calculated after [1]. **b,** Imaginary (orange) and real (blue) parts of the Fourier transform of the Raman response function. The imaginary part is proportional to the Raman gain spectrum, and the real part to Raman-induced index change.

a continuum [3]. This continuum defines the Raman gain $g_R(\Omega)$ profile [4], where $\Omega = \omega_p - \omega_s$, which unlike in crystalline materials extends over large range of detuning frequencies. It also depends on the composition of the silica glass and can vary significantly depending on the dopants used, defining the frequency shift and the amplitude of the gain. Typical Raman gain spectrum of silica glass fibre is shown on Figure 1.2b. The gain profile has two maxima at frequency shift $\Omega \approx 13$ THz and reaches values up to 2.5 $(\mathrm{W{\cdot}km})^{-1}$. The high bandwidth of the Raman gain in fused silica optical fibres make them suitable for broadband amplifiers.

In the simplest possible case of a pump wave propagating in an optical fibre any spontaneous photons which are detuned by the frequency falling within the Raman gain bandwidth will be amplified by the pump wave. The growth of the Stokes wave in this case can be described by the coupled equations [5]:

$$\frac{\mathrm{d}P_s}{\mathrm{d}z} = g_R P_p P_s - \alpha_s P_s, \tag{1.2}$$

$$\frac{\mathrm{d}P_p}{\mathrm{d}z} = -\frac{\omega_p}{\omega_s} g_R P_p P_s - \alpha_p P_p, \tag{1.3}$$

where α_s and α_p are fibre losses for Stokes and pump frequencies, and g_R is the Raman gain coefficient. In the absence of losses these coupled equations simply mean that the number of photons is conserved in the process of stimulated Raman scattering. If the pump depletion

term is ignored in Equation 1.3, substituting the result in the Equation 1.2 and solving the resulting equation, will give:

$$P_s(L) = P_s(0)\exp(g_R I_0 L_{eff} - \alpha_s L) \tag{1.4}$$

where L is the fibre length and $L_{eff} = \dfrac{1-\exp(-\alpha_p L)}{\alpha_p}$. The solution 1.4 shows that because of the fibre losses the effective length of the fibre is reduced from the length L to L_{eff}. For short fibre lengths effective length is approximately equals to L and for longer spans it asymptotically approaches the value $\dfrac{1}{\alpha_p}$.

Let's consider a simple linear cavity Raman fibre laser Figure 1.3, consisting of a span of optical fibre, two fibre Bragg grating (FBG) mirrors forming a resonator and a pump laser.

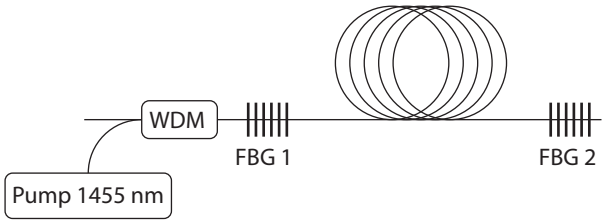

Figure 1.3: A simple Raman fibre laser setup.

The balance equations will change in this case [6]:

$$\frac{dP_p}{dz} = -\frac{\omega_p}{\omega_s} g_R P_p \left(P_s^+ + P_s^-\right) - \alpha P_p, \tag{1.5}$$

$$\frac{dP_s^+}{dz} = g_R P_p P_s^+ - \alpha P_s^+, \tag{1.6}$$

$$\frac{dP_s^-}{dz} = -g_R P_p P_s^- + \alpha P_s^-. \tag{1.7}$$

Where P_s^+ and P_s^- denote forward and backward propagating Stokes waves correspondingly, P_p is the pump wave, α is the loss for Stokes and pump wave, assuming they are equal for simplicity of the following derivations. These equations assume a steady state situation, with the radiation already established in the cavity. The stimulated Raman scattering is the dominant process here, and spontaneous emission is neglected. Considering the laser cavity length is L, the boundary conditions are $P_{s0}^+ = R_1 P_{s0}^-$ and $P_{sL}^- = R_2 P_{sL}^+$, where P_{s0} and P_{sL}

are Stokes waves powers at the input and output ends of the cavity, R_1 and R_2 are the reflectivities of the first and the second mirror correspondingly. As the Stokes wave propagate in the fibre it experience loss $\exp(-\alpha z)$ due to scattering and absorption, and at the same time, it is amplified as $\exp(g_R \int_0^z P_p(z')dz')$ due to Raman gain. From Equations 1.6–1.7 and boundary conditions it follows that $P_{s0}^+/P_{sL}^+ = P_{sL}^-/P_{s0}^- = \sqrt{R_1 R_2}$. This equation specifies the ratio between the end values for the forward and backward propagating Stokes waves. From this equation follows that $P_s^+ = K/P_s^-$, where K is a constant. Considering this, dividing Equation 1.7 by 1.5 and integrating gives [6]:

$$P_p(z)P_s^-(z)\exp\left\{-\frac{g_R\omega_p}{\alpha\omega_s}\left[\frac{\omega_s}{\omega_p}P_p(z)+P_s^+(z)-P_s^-(z)\right]\right\}=C. \tag{1.8}$$

where C is a constant, and the equation relates pump and both forward and backward Stokes waves in any point in the cavity. At the output of the cavity $z = L$ it is reduced to:

$$P_{sL}^+ = \frac{\ln\left[\sqrt{R_1R_2}\dfrac{P_{pL}}{P_{p0}}\right]+g_R\dfrac{P_{p0}-P_{pL}}{\alpha}}{\dfrac{g_R}{\alpha}\dfrac{\omega_p}{\omega_s}\left\{1-R_2-\sqrt{R_1R_2}\left[1-\dfrac{1}{R_1}\right]\right\}}. \tag{1.9}$$

where P_{p0} and P_{pL} are the input and residual pump power, and the output Stokes power is the function of these two. This function has a maximum when $P_{pL} = \dfrac{\alpha}{g_R}$ and equals to:

$$P_{sL}^+ = \frac{\ln\left[\sqrt{R_1R_2}\dfrac{\alpha}{g_RP_{p0}}\right]+g_R\dfrac{P_{p0}}{\alpha}-1}{\dfrac{g_R}{\alpha}\dfrac{\omega_p}{\omega_s}\left\{1-R_2-\sqrt{R_1R_2}\left[1-\dfrac{1}{R_1}\right]\right\}}. \tag{1.10}$$

It can be shown from Equations 1.5–1.7 that:

$$\frac{dv}{dz} = -\alpha u, \tag{1.11}$$

where $v = \dfrac{\omega_s}{\omega_p}P_p + P_s^+ - P_s^-$ and $u = \dfrac{\omega_s}{\omega_p}P_p + P_s^+ + P_s^-$, which is the reflection of the simple fact that the photons are only lost to the absorption by the fibre in the Raman scattering

process. Rewriting Equation 1.8 in terms of u, v and K provides the equation:

$$u = \sqrt{\alpha^2 v^2 + 4\alpha^2 K + 4\alpha^2 \frac{\omega_s}{\omega_p} P_{p0} P_{s0}^- \exp\left[\frac{-g_R \omega_p}{\alpha \omega_s}(v_0 - v)\right]} \tag{1.12}$$

Substituting this into Equation 1.11 and integrating gives:

$$\int_{v(z)}^{v_0} \left(\alpha^2 v'^2 + 4\alpha^2 K + 4\alpha^2 \frac{\omega_s}{\omega_p} P_{p0} P_{s0}^- \exp\left[\frac{-g_R \omega_p}{\alpha \omega_s}(v_0 - v')\right]\right)^{-1/2} \mathrm{d}v' = z. \tag{1.13}$$

This equation together with Equation 1.9 and the boundary conditions allows to find the value of the pump and Stokes waves at any point in the cavity for a given input pump power. For example using Equation 1.10, it is possible to calculate the optimal fibre cavity length for any given pump power.

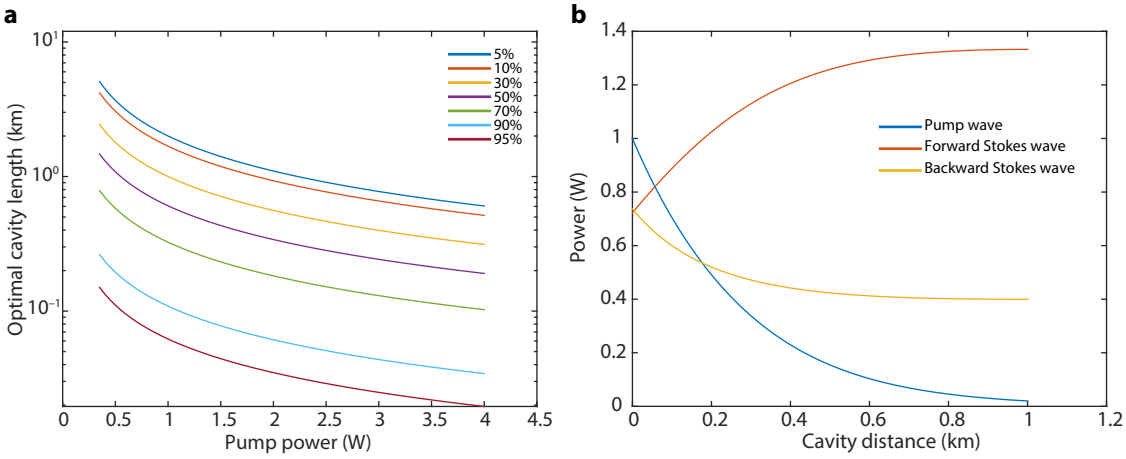

Figure 1.4: a, Dependence of the optimal cavity length on the input pump power for different values of reflectivity of the output mirror. **b,** Pump and Stokes waves power distribution along the resonator of 1 km long fibre laser.

The Figure 1.4a shows numerically calculated dependencies of the optimal cavity length on the pump power for different values of reflectivity of the output FBG mirror. Other parameters were chosen as follows: the pump wavelength 1455 nm, Stokes wavelength 1550 nm, Raman gain coefficient g_R=2.5 (W·km)$^{-1}$ for OFS Raman fibre, R_1=98%, linear loss α=0.05 km^{-1}.

It is also possible to calculate the distribution of pump, forward and back-propagating Stokes waves powers at every point in the fibre cavity. For example when the residual pump power at the end of the fibre $P_{pL} = \frac{\alpha}{g_R}$ the Stokes output P_{sL}^+ at the end of the cavity is

maximum and described by the Equation 1.10. Knowing P_{pL} and P^{+}_{sL}, allows one to find K, ν_0 and ν_L, and substituting $\nu(z)$ in the range from ν_L to ν_0 into Equation 1.13 allows to find the corresponding z. From the Equation 1.12 $u(z)$ could be determined as well. Following this procedure the values of P_p, P^{+}_{s} and P^{-}_{s} could be obtained for each point z in the resonator. As an example, numerical calculations were performed for 1 km long fibre laser with R_2 = 30% and other parameters as described above and presented on the Figure 1.4b. From this graph it is clear that even for low reflectivity output FBG, the pump wave is quickly converted to the Stokes waves.

The first Raman fibre laser operating in continuous-wave regime was demonstrated in 1976 by K. O. Hill, B. S. Kawasaki and D. C. Johnson [7]. In their setup they used fibre as a gain medium and microscopes with dielectric mirrors to form a cavity. Use of the fibre as a gain medium substantially reduces generation threshold and increases efficiency of the laser. An all fibre design employing fibre Bragg gratings as a cavity mirrors was demonstrated much later in 1988 by P. N. Kean *et al.* [8]. This allowed to drastically reduce losses and achieve narrow-band generation. To achieve laser generation at a desirable wavelength, longer than the first Stokes wavelength, in Raman fibre lasers technique called cascading is commonly employed. First cascaded Raman fibre laser was proposed and realised by S. G. Grubb *et al.* in 1994 [9]. In these lasers cascaded pumping is used, realised by the means of encapsulated cavities tuned to wavelengths of orders of Raman scattering.

1.1.2 Modeling Raman Fibre Laser

The balance equations considered in the previous section cannot predict the properties of the laser output, as they do not consider four-wave mixing interactions between the pump and the generation modes, which affects the resulting optical spectrum and power. To describe temporal and spectral properties of Raman fibre lasers, complex numerical modeling based on the NLSE is required [5]:

$$\frac{\partial A_{\mathrm{p}}^{\pm}}{\partial z}+\left(\beta_{1\mathrm{p}}-\beta_{1\mathrm{s}}\right)\frac{\partial A_{\mathrm{p}}^{\pm}}{\partial t}+\frac{i}{2}\beta_{2\mathrm{p}}\frac{\partial^2 A_{\mathrm{p}}^{\pm}}{\partial t^2}+\frac{\alpha_{\mathrm{p}}}{2}A_{\mathrm{p}}^{\pm}$$
$$=i\gamma_{\mathrm{p}}\left(\left|A_{\mathrm{p}}^{\pm}\right|^2+2\left|A_{\mathrm{s}}^{\pm}\right|^2\right)A_{\mathrm{p}}^{\pm}-\frac{g_{\mathrm{p}}}{2}\left(\left|A_{\mathrm{s}}^{\pm}\right|^2+\left\langle\left|A_{\mathrm{s}}^{\mp}\right|^2\right\rangle\right)A_{\mathrm{p}}^{\pm}, \qquad (1.14)$$
$$\frac{\partial A_{\mathrm{s}}^{\pm}}{\partial z}+\frac{i}{2}\beta_{2\mathrm{s}}\frac{\partial^2 A_{\mathrm{s}}^{\pm}}{\partial t^2}+\frac{\alpha_{\mathrm{s}}}{2}A_{\mathrm{s}}^{\pm}$$
$$=i\gamma_{\mathrm{s}}\left(\left|A_{\mathrm{s}}^{\pm}\right|^2+2\left|A_{\mathrm{p}}^{\pm}\right|^2\right)A_{\mathrm{s}}^{\pm}+\frac{g_{\mathrm{s}}}{2}\left(\left|A_{\mathrm{p}}^{\pm}\right|^2+\left\langle\left|A_{\mathrm{p}}^{\mp}\right|^2\right\rangle\right)A_{\mathrm{s}}^{\pm}, \qquad (1.15)$$

where A is the complex field envelope; z is a coordinate; t is the time in a frame of reference moving with the pump wave; $\beta_{1\mathrm{p}}$ and $\beta_{1\mathrm{s}}$ are the inverse pump and Stokes waves group velocities; β_2, α, γ, and g are the group velocity dispersion (GVD), linear attenuation, Kerr, and Raman gain coefficients; "±" denotes the forward and back propagating waves. The intensities of the counter-propagating waves are included as an average value, due to high relative speeds and low interaction times, which results in reduced contribution to the spectral broadening. During the integration the values of counter-propagating waves should be taken from the previous iteration. These equations are derived in the limit of typical structure duration exceeding value of 1 ps, the time scales considerably larger than time scales at which Raman response function changes [10].

Even though polarisation effects are not included here, these equations allow to perform detailed numerical simulation of a Raman fibre laser [11–16], and study the statistics of the output radiation, temporal and spectral properties, effects of cross-phase modulation between the pump and Stokes waves etc. For numerical simulations of mode-locked Raman fibre lasers with pulse durations considerably shorter than 1 ps the effects of Raman response function should be included.

It is also possible to numerically simulate a Raman fibre laser to find the distribution of pump and Stokes waves in the cavity. Using the same parameters of the system as in the example with balanced equations, and additional parameters of real fibre and gratings: dispersion at 1550 nm $D = -20$ ps/nm/km, dispersion at 1455 nm $D = -23$ ps/nm/km, nonlinear coefficient at 1550 nm $\gamma_{\mathrm{s}} = 5.85$ (W·km)$^{-1}$, nonlinear coefficient at 1455 nm $\gamma_{\mathrm{p}} = 7.24$ (W·km)$^{-1}$, the difference between pump and Stokes group velocities was neglected.

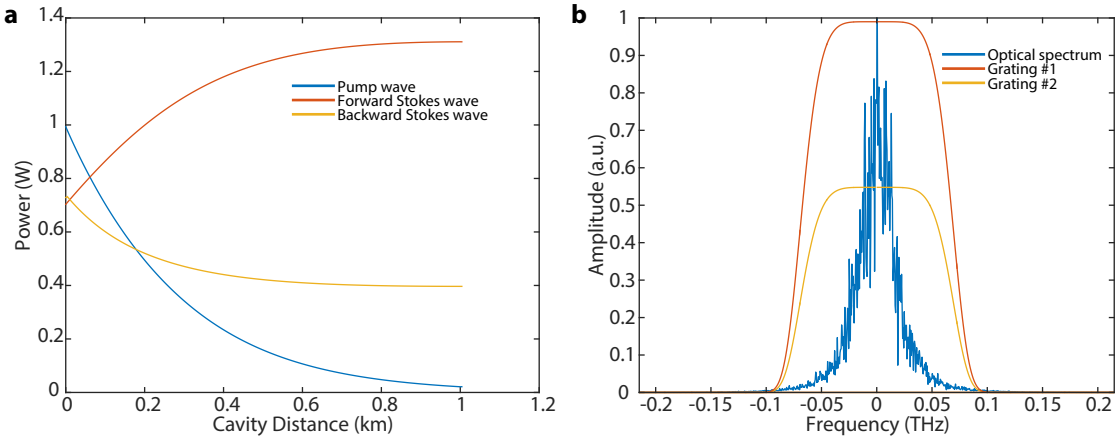

Figure 1.5: a, Pump and Stokes waves power distribution along the resonator of 1 km long fibre laser. **b,** Optical spectrum of the Stokes radiation obtained in the full NLSE model.

The reflectivity of the gratings were chosen the same $R_1 = 98\%$ and $R_2 = 30\%$. Both gratings had width of 1 nm and super-Gaussian profile. The pump wave was modelled as a single frequency.

The results of numerical simulations are presented on the Figure 1.5a and are in perfect agreement with the power distribution predicted by the balanced equations. The optical spectrum of the laser radiation averaged over 4 round-trips obtained in this example is shown on the Figure 1.5b.

1.2 Mode-locking in Fibre Lasers

Ultrashort optical pulses find more and more practical applications in such areas as material processing [17], biomedical applications [18], telecommunications [19, 20], metrology [21–23], supercontinuum generation [24], gas sensing [25], scientific research and others. This growing interest in shorter and more powerful pulses drives the development of new types of lasers capable producing them. Since the development of high-brightness laser-diode pump sources in the 1980s and the demonstration of Erbium-doped fibre amplifiers [26, 27], interest in fibre lasers started to grow. Initially the interest in ultrafast fibre lasers, i.e. fibre lasers generating ultrashort optical pulses, was fuelled by the demand for increasingly shorter pulses in optical telecommunications, as well as their simplicity and compact design. In the last two decades ultrafast fibre lasers have seen continuous development and tremendous amount of research went into new designs, novel fibre types and

geometries, types of dopants used, all of which considerably extended their areas of application and performance capabilities. Most of these ultrafast fibre lasers produce ultrashort pulses by operating in the regime of mode-locking.

Mode-locking – is a group of methods to produce ultrashort optical pulses from lasers. Generally it can be described in terms of either frequency domain or time domain. The term itself comes from frequency domain description. The spectrum of radiation of a laser with cavity length L will consist of many longitudinal modes separated by $\Delta f = \frac{c}{2nL}$, where c – is the speed of light and n – is the refractive index of the media [28]. Generally these modes will have random phases, and interference terms in the total intensity $|E(t)|^2$ will average out and the output of the laser will be of constant power as is the case with multimode continuous wave (CW) lasers. However if the phases of different modes can be controlled, the output temporal dynamics will change. Mode-locking then is a group of methods to introduce fixed constant value of phase difference between adjacent modes. The first indications of mode-locking were observed by Gürs and Müller [29] in ruby lasers. The theory of mode-locking (frequency locking, phase-locking) was first introduced by W. E. Lamb Jr. [30] in the theory of optical maser. If the relative phases of the modes are fixed with respect to each other the output of the laser in time domain will be represented by a train of pulses, with time separation $1/\Delta f$ corresponding to the cavity round-trip time. The minimum temporal duration of the resulting pulse $\tau_p = \left[(2M+1)\Delta f\right]^{-1}$ [31], where $2M+1$ is the number of cavity modes locked, is inversely related to the spectral bandwidth of the laser radiation. The broader the optical bandwidth – the shorter pulse duration can be achieved.

In terms of analytical description, the frequency domain approach becomes unmanageable as in practice ultrashort pulses are produced by mode-locking of large number of modes over wide bandwidth and mechanisms that are involved are generally nonlinear. An early review of frequency-domain analysis was done by Smith *et al.* [32].

There are different methods that can be used to induce such phase relationship between modes, but they can be divided into two categories – passive and active mode-locking.

1.2.1 Active mode-locking

Active mode-locking involves use of external sources of periodic signal to induce a modulation of the amplitude or the phase of the intracavity optical field. The modulation frequency should be equal to or a multiple of the mode spacing in the frequency domain. Depending on whether the amplitude or phase is modulated it is called amplitude or frequency modulation correspondingly. In practice this can be done for example by introducing the acoustic optical modulator into the laser cavity. Modulation leads to sidebands generation which overlap with neighbouring modes and results in phase synchronisation. L. E. Hargrove, R. L. Fork, and M. A. Pollack were first to report active mode-locking in a He-Ne laser [33]. They used a fused quartz block inside the laser resonator as an optical modulator. By exciting it at longitudinal acoustic resonance frequency they were able to produce diffraction orders fluctuating at double the driving frequency, thus coupling optical modes of the laser. Further development of these ideas was done by M. H. Crowell [34]. He was able to substantially increase the pulse repetition rate by astutely adjusting the loss of the cavity. At the same time big theoretical work describing systems analogous to ones built by L. E. Hargrove and M. H. Crowell was done by M. DiDomenico [35].

Another method of active mode-locking – regenerative RF feedback was proposed by G. R. Huggett [36]. The main idea of this method is to measure RF beats between axial modes and use this differential frequency as external feedback to the laser cavity by the means of phase modulator. This system has a few advantages such as ability to track changes in real time and tune parameters to keep system stable. Another advantage is applicability to any laser system where continuous phase-locking is required.

The analytic theory of active mode-locking was established by Kuizenga and Siegman [37]. They studied the process in the frequency domain, with longitudinal modes injection locked by the loss modulator. They predicted and later confirmed the pulse shape to be Gaussian.

The general scheme of an actively mode-locked laser is presented on the Figure 1.6a. The resonator is formed of two mirrors, with gain and amplitude modulator placed inside the cavity. The longitudinal modes are separated by $\Delta\omega = \frac{2\pi}{T_{\mathrm{rt}}}$, where T_{rt} is the cavity round-trip

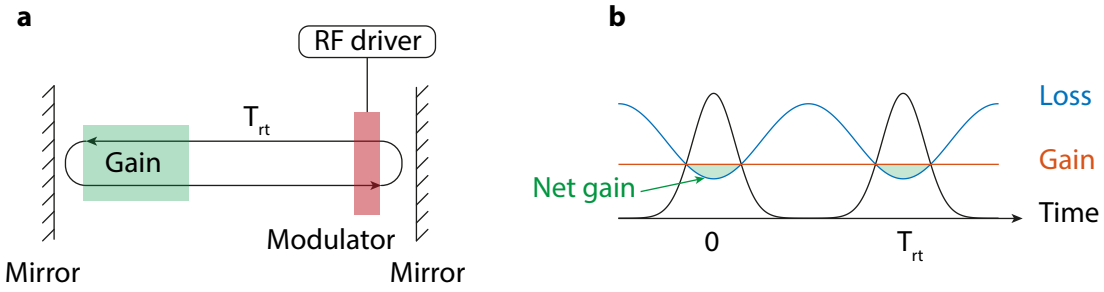

Figure 1.6: a, Schematic of an actively mode-locked laser. **b,** Time dependence of net gain and pulse.

time. The amplitude modulator introduces cosinusoidal loss in the cavity at the frequency $\omega_m = \Delta\omega$. This modulation creates sidebands for the central mode, for which gain is the highest, and these sidebands will injection lock the adjacent cavity modes, which in turn will lock their neighbours. The resulting pulse will have a Gaussian shape:

$$A(\omega) = A_0 \exp\left(-\omega^2\tau^2\right) \tag{1.16}$$

where

$$\tau^4 = \frac{2g}{(M\omega_m^2\omega_g^2)} \tag{1.17}$$

where peak gain is $1 + g$ and $g \ll 1$, M is the modulation depth, and $2\omega_g$ is the gain bandwidth. Figure 1.6b shows the active mode-locking in time domain. The modulation provides a time dependant loss, and whenever the loss dips below the gain level the curvature of the pulse envelope is negative. In the time domain the pulse shape is [38]:

$$A(t) = A_0 \exp\left(-\frac{t^2}{2\tau^2}\right) \tag{1.18}$$

Active mode-locking does not allow one to achieve the shortest possible pulses, as the modulation frequency cannot be raised arbitrarily. However, by driving the modulator at frequency an integer multiple of the round-trip frequency it is possible to make multiple pulses circulate in the laser cavity. This will increase pulse repetition rate proportionally to the increase of the driving frequency, and reduce the pulse duration, however the pulse

energy will not be as high as in fundamental mode-locking. The first experimental and theoretical results on harmonic mode locking were presented by M. F. Becker, D. J. Kuizenga and A. E. Siegman [39]. They were able to drive the modulator five times the fundamental frequency of the laser resonator, thus increasing repetition rate fivefold.

By the year 1989 soliton pulses as short as 4 ps were generated in a actively mode-locked ring cavity erbium-doped fibre laser (EDFL) with extra 2 km of fibre with anomalous GVD [40]. Further improvements in active harmonic mode-locking resulted in development of the system with pulse-repetition rate as high as 40 GHz using a high-speed $LiNbO_3$ modulator [41].

The main problem with active harmonically mode-locked fibre lasers is the stability of the pulse train generated over extended periods of time. Different stabilisation techniques are required such as phase-locking, or use of high-finesse Fabry-Perot filter with a free spectral range equal to pulse repetition rate. To eliminate environmental factors modulation frequency should be matched to longitudinal mode spacing. This can be achieved by the use of the technique of regenerative mode locking [42], where the electrical signal for the modulator is generated from the laser output by a clock-extraction system, amplifier and a phase controller.

One of the biggest disadvantages of active mode-locking is that the pulse-shortening rate (PSR) for active mode-locking decreases significantly as the pulse circulating in the cavity gets shorter. To achieve shorter and more stable pulses some other mode-locking techniques should be employed, which in contrary to active are called passive mode-locking techniques.

1.2.2 Passive mode-locking

The main difference between active and passive mode-locking is that passive mode-locking does not require external sources of periodic signal to produce pulses. Since the first picosecond pulses were generated with the help of passive saturable absorber [43], it has been the main method for obtaining the shortest pulses. Passive mode-locking techniques rely on some intracavity element, or group of elements, called saturable absorber, which will

introduce changes in the light circulating in the cavity. Saturable absorbers can be broadly separated into two classes: slow saturable absorbers and fast.

Slow Saturable Absorber

Saturable absorber is a lossy element with loss dependent on the optical intensity. Loss is reduced at higher optical intensities thus permitting only short pulses with high peak power to exist in the laser cavity. Slow saturable absorber cannot recover it's absorption on the timescale of an ultrashort pulse. It is however possible to generate picosecond pulses with slow saturable absorbers, which was demonstrated in the early experiments on passive mode-locking was done by E. P. Ippen, C. V. Shank, and A. Dienes [44]. It was the first continuous-wave mode locking with dye saturable absorber. In a later experiment with flashlamp-pumped dye lasers with dye saturable absorber [45] it was demonstrated that recovery time of the dye saturable absorber was in an order of nanoseconds. Surprising at the time, but it was later explained by New [46], who suggested that it was possible due to dynamic saturation of gain.

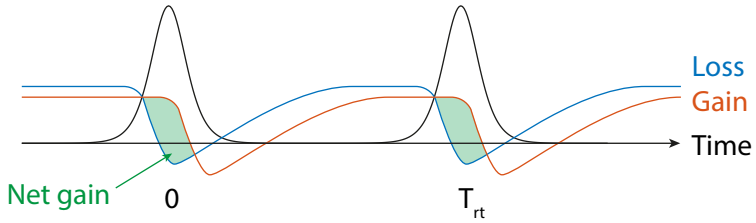

Figure 1.7: Pulse-shaping time dependant gain and loss dynamics for slow saturable absorber mode-locking.

As demonstrated on the Figure 1.7, the absorber would quickly saturate and absorb the leading edge of the pulse, while gain depleted by the peak of the pulse would cause loss for the trailing edge of the pulse, with both gain and saturable absorption recovering before the arrival of the pulse on the next round-trip. The resulting pulse have a simple hyperbolic secant shape [47]:

$$A(t) = A_0 \mathrm{sech} \frac{t}{\tau} \tag{1.19}$$

where

$$\frac{1}{\tau^4} = \frac{\omega_g^2 A_0^4}{4}\left(\frac{l_0}{W_l^2} - \frac{g_0}{W_g^2}\right). \tag{1.20}$$

For slow saturable absorber to successfully mode-lock the laser one important condition should be met: $\frac{l_0}{W_l} > \frac{g_0}{W_g}$, where l_0 is unsaturated loss, g_0 is initial undepleted gain, before arrival of the pulse, W_l is the saturation energy of the saturable absorber, and W_g is the saturation energy of the gain. This condition simply mean that the saturable absorber should saturate more strongly than the gain for the net gain to be positive.

One of the most important applications of slow saturable absorber is the passively mode-locked semiconductor laser [48], where integrated saturable absorbers have been created by defects or inhomogeneous excitation with tandem contacts. Pulse repetition rates up to 1.54 THz were achieved [49] in such lasers. The main application of passively mode-locked semiconductor lasers is fibre optic telecommunication systems, where they are used as pulse sources. Another frequently used type of slow passive saturable absorber is semiconductor saturable absorber mirror (SESAM) [50, 51], which is a mirror structure with incorporated saturable absorber, all made in semiconductor technology, but could be used to mode-lock a wide range of different types of lasers. Some more exotic designs include semiconductor saturable absorbers which are based on quantum dots embedded in glass [52].

More recent developments include thin layers of carbon nanotubes used as saturable absorbers [53]. Carbon nanotubes proved to exhibit very versatile absorption features desirable for passive mode-locked lasers, such as high bandwidth of absorption [54].

In most real, or material saturable absorbers the shortest achievable pulse duration is limited by the material response and recovery time [55]. Even for carbon nanotubes, which have recovery time of approximately 750 fs [56], the shortest pulses reported are of an order 100 fs [57]. The advantage of real saturable absorbers is simplicity, but to achieve the shortest and most powerful pulses, artificial fast saturable absorbers should be used.

Fast saturable absorbers

A fast saturable absorber is an element or a group of elements that based on the fastest optical nonlinearities, which are reactive and nonresonant. For example the index of refraction in glass has response time of a few femtoseconds [58], and has a very large bandwidth. As it's response and recovery are almost instantaneous compared to the duration of the pulse, they do not rely on gain saturation for the pulse formation. The mechanism of action is very simple and shown on the Figure 1.8. The saturable absorber is fast enough to shape both leading and trailing edges of the pulse.

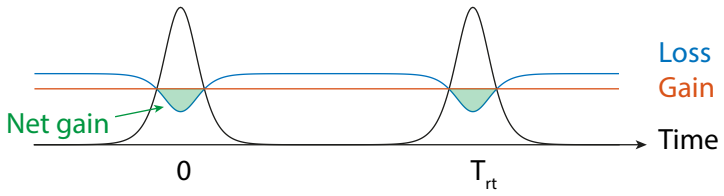

Figure 1.8: Pulse-shaping time dependant gain and loss dynamics for fast saturable absorber mode-locking.

There are some devices capable of exhibiting properties very similar to saturable absorbers but not actually exploiting saturable absorption. For example a NOLM [59, 60], which mechanism is based on interferometric or additive-pulse mode-locking. In simple configuration shown on Figure 1.9 two output ports of a non-50/50 coupler joined by a piece of fibre. The input pulse is split into two counterpropagating parts, and after propagating in the nonlinear media, the acquired phase shift will depend on the intensity of the field as $\phi = \frac{2\pi n_2 |E|^2 L}{\lambda}$. Depending on the phase shift the field will be either reflected back or transmitted, which leads to transmission of higher intensity central part of the pulse and reflection of lower intensity wings. Non-symmetric coupler could be replaced with 50/50 coupler and asymmetrically placed gain within the loop, in which case such device is called NALM [61]. In this configuration the pulse propagating in counter-clockwise direction is immediately amplified in doped fibre placed close to the coupler, while clockwise propagating part of the pulse is amplified after propagating through the fibre, thus two parts acquire different nonlinear phase shift. If NALM is adjusted such that the phase shift in the central

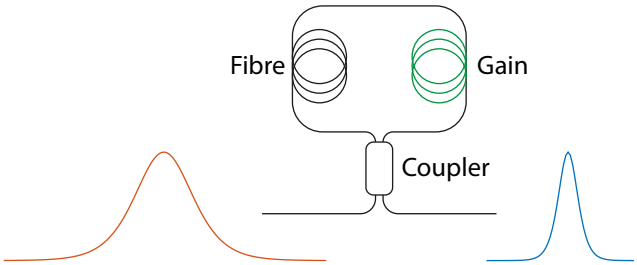

Figure 1.9: Pulse shortening by the NOLM with unbalanced non-50/50 coupler or NALM with asymmetrically placed gain and nonlinear medium.

part of the pulse is close to π, this part of the pulse will be transmitted while wings will be reflected. As a result pulse will be amplified and shortened after leaving NALM. First lasers utilising NALM as a mode-locking element were reported in 1991 [62–64]. Pulses as short as 98 fs were obtained in later experiments [65]. Using external amplifiers and linear dispersive compressors it was possible to produce 30 fs pulses.

Another nonlinear mode-locking technique that is used in fibre lasers is nonlinear polarisation rotation or NPE [66]. The physical mechanism involved is rather simple and relies on nonlinear birefringence. Conceptually it is similar to NALM, but in this case differently polarised components of the same pulse are used instead of counter propagating waves. The most simple setup is a ring cavity that consists of doped fibre, output coupler, wavelength-division multiplexing (WDM) and polarising isolator placed between two polarisation controllers. The mechanism of action can be explained as follows. A linearly polarised pulse after the polarising isolator enters the polarisation controller where its polarisation is changed to elliptical Figure 1.10. During propagation in the fibre polarisation components experience different phase shifts due to self-phase modulation (SPM) and cross-phase modulation (XPM) effects which result in nonuniform state of polarisation across the pulse. The second polarisation controller is adjusted to change the polarisation of the central high amplitude part of the pulse to linear, which allows central part to pass through the isolator, while the wings of the pulse get attenuated. This effectively shortens the pulse. The first passively mode-locked lasers employing the technique of NPE were developed in 1992 [67] and by year 1993 77 fs pulses with 90 pJ energy were generated in normal group velocity dispersion ring cavity laser [68].

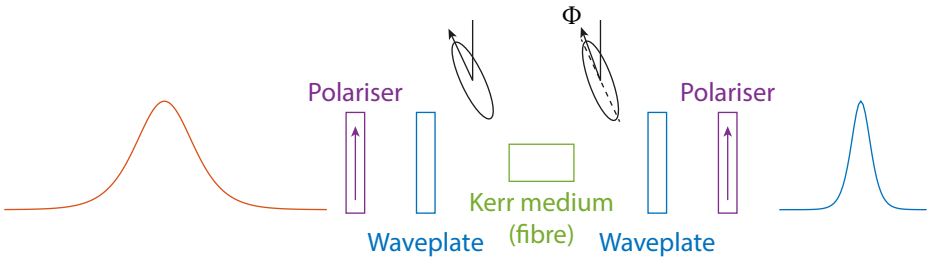

Figure 1.10: The mechanism of pulse shortening by NPE.

One considerable drawback of lasers mode-locked by NPE is environmental stability. In long length cavities required to induce sufficient phase shift ambient temperature variations can lead to birefringence fluctuations that can significantly affect the mode-locking process. This problem can be addressed by reducing the cavity length or introducing polarisation maintaining fibre into the cavity so that linear birefringence is not affected by temperature variations.

There are other less widespread interesting passive mode-locking techniques. In one experiment dual-core fibre with one core doped with Erbium played roles of both gain medium and saturable absorber [69]. Mechanism of action is relatively simple and relies on nonlinear directional coupling. At high powers most of the energy is confined in the doped fibre while at low powers energy is transferred to the second undoped core, resulting in pulse shortening. Another simple design uses three fibre Bragg gratings to create coupled-cavities and relies on additive-pulse mode locking [70]. One of the equal parts is doped with Erbium while another is standard single-mode fibre. Even though cavity lengths were not exactly matched the laser produced mode-locked pulses. This can be explained by wavelength self-tuning when different spectral components are reflected at different depth in the fibre Bragg grating, which effectively matches cavity lengths. Another interesting recent development very promising for mode-locked fibre lasers is an array of waveguides exhibiting nonlinear coupling [71].

1.2.3 Mode-locked Raman Fibre Lasers

As it was described in the previous section, passive mode-locking enables higher repetition rates and shorter pulse durations compared to active mode-locking, but in both cases the

shortest possible pulse duration will depend on the gain bandwidth available. In fibre lasers gain bandwidth and the wavelength of operation depend on the gain mechanisms which is usually provided by fibres doped with ions of various rare-earth metals. The first fibre laser was demonstrated in 1961 [72] and used a Nd doped fibre as a gain medium, but it was only in the late 1980s that fibre lasers saw extensive development with the demonstration of Erbium-doped fibre amplifiers [26, 27].

Mode-locked fibre lasers based on Erbium doped fibre are one of the most widespread types of ultrafast fibre lasers. Erbium doped fibre have a broad gain bandwidth, high efficiency and can operate at very high output powers [73]. The operating wavelength of such lasers lies in 1535–1560 nm spectral region. Another popular dopant of choice is Ytterbium. Fibre lasers based on Ytterbium operate in 1000–1100 nm [74] spectral region and pulse duration is comparable to Erbium based lasers, but achievable output powers can be somewhat higher [75]. Other dopants can also be used such as Neodymium, which can be conveniently pumped by GaAs semiconductor lasers at 800 nm, with operating wavelength at 1060 nm. It can also operate near 920 nm and 1350 nm. In the early 1990s a lot of development went into Praseodymium doped fibre to make lasers and amplifiers on ions Pr^{3+} that can operate at 1.3 μm and 1.05 μm. Thulium doped fibre lasers operating in 1.71 μm to 2.1 μm spectral region were developed in mid 1990s because of their potential applications. Thulium doped fibre lasers can also operate at 481 nm using up conversion pumping scheme. Holmium doped fibre lasers pumped at 800 nm and operating in 2 μm spectral region are used for medical and eye-safe applications.

Although high repetition rates exceeding 100 GHz [76] and pulse durations as short as 47 fs directly from the laser [77] were obtained from lasers based on rare-earth metals doped fibres, they exhibited comparably low output powers limited to nJ range of energies per pulse. Furthermore, wavelength of operation and gain-bandwidth is dependant on the dopant used. This makes the Raman laser a good platform of choice for passive mode-locking as it provides operation wavelength tuneability and wide enough bandwidth to support femtosecond pulses [78], which can possibly be further extended by appropriate combination of pump sources. It is also proved to be capable of high output powers [79].

Compared to other types of mode-locked lasers, fibre lasers have much more pronounced

nonlinear and dispersive effects, and even though they also allow incorporation of different types of fibre for dispersion compensation, which can be very difficult in case of solid state bulk lasers, these effects severely limit the performance of mode-locked fibre lasers, especially pulse power, pulse duration and shape of the pulse. Various methods were employed to fight these problems, such as nonlinearity [80] and dispersion [81] management. Alternatively nonlinearity and dispersion can be used as a mean to increase the pulse energy by operating laser in similariton regime.

Any pulse propagating in a normal dispersion amplifier will asymptotically evolve into a parabolic pulse [82]. The resulting parabolic pulse will propagate further in self-similar manner, with spectral and temporal width growing exponentially with positive linear chirp being preserved. Such parabolic pulses allow similariton mode-lock lasers.

Similariton mode-locking proved to be a promising technique for obtaining high power pulses without wave-breaking in fibre lasers as similaritons can tolerate strong nonlinearity [83], unlike dispersion managed and soliton based mode-locked fibre lasers [84, 85], in which wave breaking due to excess of nonlinear phase is the main limiting factor for pulse energy. Furthermore as similaritons contain linear chirp they can be easily dechirped to nearly Fourier transform limited pulses [82,86]. Pulse energies as high as 61 nJ and as short as 55 fs were achieved in different similariton mode-locked lasers recently [87–90].

Different approaches and architectures were proposed to obtain similaritons. Two main ways are parabolic amplifiers and lasers. In parabolic amplifiers initial input pulse from an external source evolves self-similarly into parabolic pulse in the normal dispersion amplifier while in similariton lasers parabolic pulses are formed in the cavity and maintained by spectral filtering and gain. Reported systems can be categorised by gain media, cavity geometry and mode-locking element used. As a gain media Ytterbium [86, 91–93], Erbium [94] were widely used. Raman proved to be versatile mechanism for similariton generation as it does not rely on any particular wavelength and provide wide enough bandwidth to support femtosecond pulses [15,83,95–98]. To take advantage of the broad Raman gain bandwidth, the pulse must experience large gain per round trip [92]. Some authors used free-space optics [86, 90–92, 99], and though very good results can be achieved, free-space optics has problems with environmental stability and simplicity of tuning. On the other hand all-fibre

lasers are much more stable, robust and show comparable performance. By cavity design reported all-fibre lasers can be generally divided to ring cavity [15, 81, 90, 96, 97], linear cavity [92] and gamma-shaped cavity [100] type.

Recently a new concept of mode-locked laser was proposed combining the use of optical similaritons and Mamyshev Regenerator (MR) [101]. First proposed in the context of regeneration of telecommunication signals, Mamyshev optical regenerator relies on the SPM-induced spectral broadening of the degraded signal and following subsequent shifted spectral filtering. A transmission line consisting of concatenated double-stage MRs have a particular eigenpulse preserving both intensity profile and phase along the line. In the proposed concept a ring resonator consisted of a piece of Ytterbium doped fibre, optical filter, a piece of standard single-mode fibre, and another optical filter, which combined constituted a single double-stage MR. The pulse in such cavity experience constant transformation between parabolic shape in the amplifying part of the cavity and Gaussian pulse after the second optical filter. The output pulse had linear chirp which can be easily compensated to achieve subpicosecond pulses.

In conclusion mode-locked Raman all-fibre lasers operating in similariton regime are a very promising platform for generation of high energy ultra-short pulses.

1.3 Random Distributed Feedback Raman Fibre Lasers

A basic laser design requires a gain medium to provide amplification, and a positive feedback mechanism, usually represented by a cavity. The lasing is achieved once the total gain overcomes the total losses in the cavity. While gain mechanisms could be different, the feedback is usually provided by point-action reflectors, i.e. mirrors. The lasing properties of a laser such as frequency modes composition and temporal dynamics are then defined by the gain mechanism used, the geometry and arrangement of the cavity. There are, however, other possible feedback mechanisms, such as random distributed feedback. In this case the feedback is provided by the random scattering events, which effectively increase the mean optical path, resulting in higher amplification and ultimately lasing. The spectrum and temporal dynamics in this case would be determined by the spatial arrangement of the

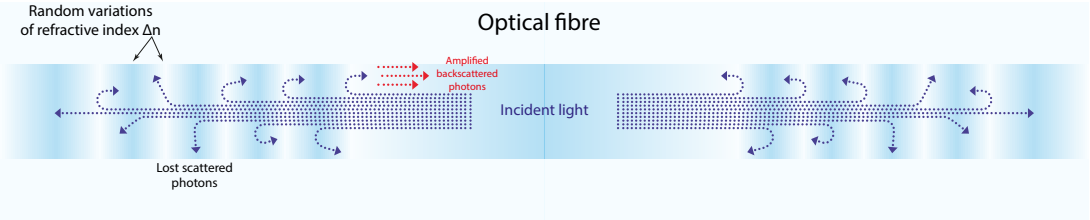

Figure 1.11: The concept of a random distributed feedback fibre laser.

random scatterers. The main concept behind the random laser – the process of multiple scattering in amplifying media leading to coherent radiation – was originally proposed by Letokhov in the context of astrophysics [102] and experimentally realised later by different groups [103, 104]. Since then this area of research developed into a separate field of laser physics. In practice random lasers can be realised in many different configurations, e.g. nano-particles of titanium oxide TiO_2 in dye, where nano-particles play the role of random reflectors and dye acts as an amplifying media.

While simplicity of the design of random lasers is an attractive feature, their sometimes unpredictable complex lasing properties limit their widespread practical application. Directionality, spectral and temporal dynamics are more difficult to control, compared to conventional design, although some of the unusual properties of random lasers are unique and can be indispensable in some applications. One particular design however attracts a lot of attention and show great promise – RDFL [105]. In the most basic design an RDFL consists only of a piece of conventional passive telecommunication optical fibre and a pump laser diode, directly connected to the fibre. Being effectively a one-dimensional system, it solves the problem of directionality for a random laser. The mechanisms involved in operation of a RDFL laser are demonstrated on the Figure 1.11.

The gain is provided by the stimulated Raman scattering, described in the section 1.1.1 and the random feedback is provided by the Rayleigh scattering, which is an elastic scattering process. While propagating in the fibre, the light scatters on small randomly distributed variations of refractive index Δn, which are an inherent consequence of the fibre manufacturing process. Only a small fraction of light is backscattered into the cavity due to fibre geometry and small numerical aperture (NA) which limits the number of scattered photons that can be accepted. Hence the backscattering coefficient is very small, with typical

values $\varepsilon = \alpha_s \cdot Q \sim 4.5 \cdot 10^{-5}$ km^{-1} [106,107], where Q is defined by the numerical aperture and geometry of the fibre used. As a result backscattered radiation is very small, even for very long fibre lengths.

Even though Rayleigh scattering is extremely small it can be detected which is used in optical time domain reflectometry since the late 1970s [108]. If the fibre is long enough the effect of double Rayleigh scattering could be observed, which was reported in long-haul fibre-optic transmission lines [109]. The effect manifested itself as irregular spikes of lasing which occurred at high values of the distributed Raman gain in the system. Later, in the work studying the generation properties of ultra-long fibre laser, with the cavity length of an order 270 km [110], it was predicted that in such long cavities the Rayleigh scattering based random feedback could be sufficient for lasing. At fibre lengths greater than 270 km the Rayleigh scattering provides higher levels of feedback than high reflectivity FBG mirrors at the end of the fibre, which effectively lowers the laser generation threshold in RDFL compared to a conventional laser.

1.3.1 Design

There are three possible basic configurations of the random distributed feedback fibre laser. First, is the backward-pumped configuration, in which the pump wave counter-propagates with the Stokes wave Figure 1.12a. This configuration could be symmetrical double-arm Figure 1.12a, or single-arm Figure 1.12c, where the FBG acts as a mirror and reflects forward propagating Stokes radiation back into the fibre making it effectively equivalent to the double-arm configuration, which was experimentally confirmed in [106]. Similarly, the forward-pumped configuration could be double- or single-armed, with the difference that the Stokes wave co-propagates with the pump wave. In double-arm configurations, due to complete symmetry of the configuration, both outputs of the laser are identical, providing similar output powers and generation properties. Single-arm variation has the advantage in the reduced required fibre length and number of other components, most importantly the pump laser, having almost identical performance, which was confirmed in [106]. In the third possible configuration shown on the Figure 1.12e a span of optical fibre is pumped

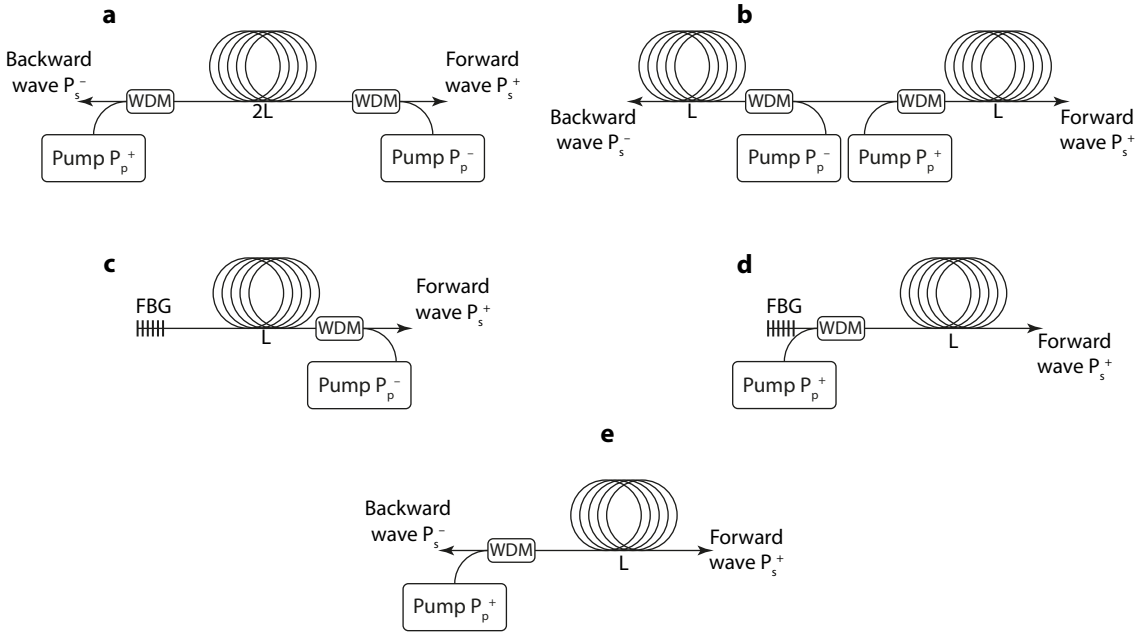

Figure 1.12: Random distributed feedback fibre laser configurations. Equivalent double **a,** and single-arm **c,** backward pumping configurations. **b, d,** Forward pumping configurations. **e,** Single-arm single pump configuration.

from one end and the Stokes radiation freely escapes from the both ends of the fibre, while feedback provided only by Rayleigh scattering.

1.3.2 Generation Properties

In every configuration described previously the Raman RDFL has a clear generation threshold. The power performance of a double-arm backward pumped laser with fibre lengths 27.1, 48.7 and 72.9 km is shown on the Figure 1.13. The lasing threshold of 0.6 W of power per one pump is clearly seen for all fibre lengths. The laser exhibits linear output power growth above the lasing threshold and efficiency slope of approximately 50%. The combined output power from both ends reached 3.3 W at 7 W of pump power in this particular configuration.

The optical spectrum of the radiation below the lasing threshold power is broad and corresponds to the amplified spontaneous emission spectrum, which is defined by the Raman gain profile of the given fibre. Above the generation threshold the spectrum narrowing is observed from typical for Raman gain ~10 nm to ~1 nm, which is an important criteria of the transition from amplified spontaneous emission to lasing regime. However, there is a difference in the mechanisms of narrowing. In a conventional laser with cavity modes, the

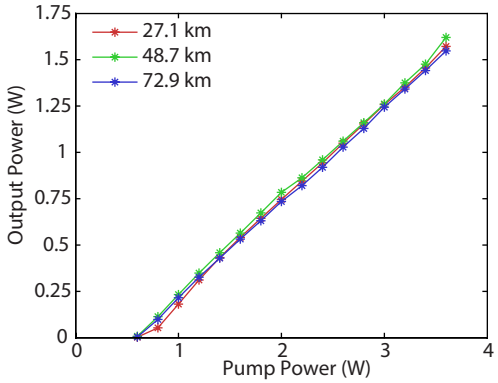

Figure 1.13: Typical output power performance of the double-arm backward pumped Raman RDFL.

narrowing of each individual mode is achieved after many round-trips and multiple reflections from the cavity mirrors, while in Raman RDFL the narrowing is defined by the gain profile. Effectively, this makes RDFL a single mode laser with a continuous spectrum. As the Raman gain profile of a typical telecommunication grade fibre has a double-peak structure with two maxima near 1555 nm and 1565 nm (given 1455 nm pump), the lasing could be achieved at two wavelengths, either separately or simultaneously depending on the system configuration and the pump power level. Generally the spectrum tends to broaden with pump power increase, which is similar to spectral broadening observed in conventional Raman fibre lasers [111].

1.3.3 Control of the Spectral Properties of the Radiation

Broadband Raman gain and Rayleigh scattering based random feedback, together with the Stokes power distribution in the fibre in forward-pumped double-arm configuration [105, 112, 113] allows to safely incorporate spectral filters Figure 1.14, and make it possible to control the spectral properties of the output radiation. For example a Fabry-Pérot etalon can be used to achieve multiple narrow spectral lines within the Raman gain bandwidth [114]. The spectral linewidths and separation is determined by the finesse and the free spectral range of the etalon in this case. Interestingly enough the power distribution between the lines is flatter compared to the case without the spectral filter. This could be explained by the reduced gain competition between the spectral components. It is also possible to use a FBG or an array of FBGs at required wavelengths as a spectrally selective component,

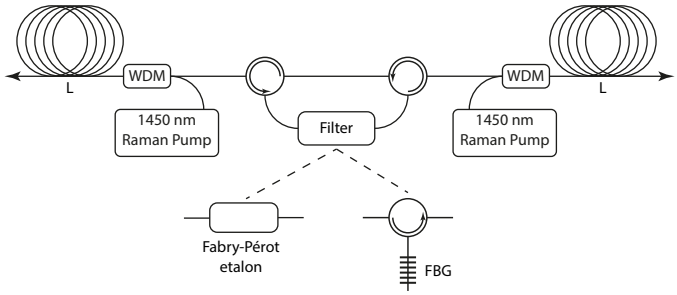

Figure 1.14: The setup configuration which provides control over spectral properties of the RDFL radiation.

with the help of an additional circulator. In all cases the linewidth follows the width of the spectral filter at lower pump powers up to ~1.2 W, and broadens considerably at higher powers. Multiwavelength operation can also be achieved by incorporation of all-fibre Lyot filter in the central part (without the circulators shown on the Figre 1.14) [115]. An all-fibre Lyot filter may be made of two 45° tilted FBGs written in a polarisation maintaining (PM) fibre along it's principle axis and a piece of PM fibre forming the cavity [116,117]. The bandwidth and free spectral range of the filter depend on the PM fibre length and could be easily adjusted. Raman RDFL incorporating such all-fibre Lyot filter was experimentally realised [115], with multiwavelength generation achieved in the whole range of Raman gain spectral profile. The laser had flat power distribution between the lines, with only 0.5 dB power variation across 8 lines in 4 nm region. Each line was almost three times narrower than the bandwidth of the Lyot filter used.

Another possibility is to use a tunable filter to tune the wavelength of the output radiation. In [118] a tunable acousto-optic filter of spectral width 1.5 nm was used, to change wavelength in the range 1530–1575 nm. Impressively, the output power variation in the experiment did not exceed 3% within the whole tuning range, which is much better compared to the conventional linear or a ring cavity, where the power flatness is around 20% within the similar tuning range [119,120].

In principle RDFL can combine any tunable, multiwavelength or narrowband generation properties in any combination, providing great flexibility in terms of design and requirements. For example, in [121] the authors used Mach-Zehnder interferometer based on two long-period FBGs as a tunable broadband filter, in combination with a Fabry-Pérot fil-

ter, to achieve tunable multiwavelength generation with small spectral width of individual lines. The laser operated at 12 different wavelengths and was tunable in the range 1553.9–1565.4 nm, with spectral width of each individual line of only 0.034 nm.

1.3.4 Modeling Random Distributed Feedback Fibre Laser

Since the demonstration of a random distributed feedback fibre laser [105] many different configurations were developed and demonstrated [113, 118, 122–127], operating in different spectral bands [118, 122–124], providing tuneability over a large range of wavelengths [118], cascaded regime [106, 125] and multi-wavelength output [123, 124]. Particularly interesting for telecommunication applications is the noise level of RDFLs, which can be lower than of conventional lasers [128]. Such a broad range of designs and practical applications require a comprehensive theoretical and numerical description, which proved to be very challenging [129]. Power generation performance of an RDFL can be described by a simple power balance model [105, 118], giving a good prediction of the generation threshold, longitudinal power distribution [113], providing tools for optimisation of the power performance [130] and estimation of the noise properties of an RDFL [128].

However, a simple power model does not allow for the description of spectral and temporal properties of different designs of random lasers and so various other models are used. The random generation can be represented in terms of sets of modes of an active or passive cavity, extended or localised [129, 131–135]. Some systems could also be described by Maxwell's equations combined with the rate equations [136,137]. Different numerical methods are employed to treat such systems ranging from Monte-Carlo simulation of a random walk of photons [138], to the transfer matrix method [139, 140], to the finite difference time domain method [141–143]. It is particularly difficult to apply these methods to description of fibre random lasers due to generally great cavity lengths. To investigate numerically power, spectral, temporal and statistical properties of an RDFL's radiation a modified NLSE could be used [144], which takes into account only average energy feedback via random Rayleigh backscattering.

Let's consider a symmetrical forward pumping RDFL configuration shown on the Fig-

ure 1.12b. To describe it a set of generalised NLSEs with additional terms describing random Rayleigh scattering [144] can be used. The equations can be z-averaged over dispersion walk-off length of the pump and Stokes waves which nullifies the phase cross-modulation term [13]:

$$\frac{\partial A_{\mathrm{p}}^{\pm}}{\partial z^{\pm}} + \left(\beta_{1\mathrm{p}} - \beta_{1\mathrm{s}}\right)\frac{\partial A_{\mathrm{s}}^{\pm}}{\partial t} + \frac{i\beta_{2\mathrm{p}}}{2}\frac{\partial^2 A_{\mathrm{p}}^{\pm}}{\partial t^2} + \frac{\alpha_{\mathrm{p}}}{2}A_{\mathrm{p}}^{\pm} = i\gamma_{\mathrm{p}}\left|A_{\mathrm{p}}^{\pm}\right|^2 A_{\mathrm{p}}^{\pm} - \frac{g_{\mathrm{p}}(\omega)}{2}\left(\left\langle\left|A_{\mathrm{s}}^{\pm}\right|^2\right\rangle + \left\langle\left|A_{\mathrm{s}}^{\mp}\right|^2\right\rangle\right)A_{\mathrm{p}}^{\pm}, \tag{1.21}$$

$$\frac{\partial A_{\mathrm{s}}^{\pm}}{\partial z^{\pm}} + \frac{i\beta_{2\mathrm{s}}}{2}\frac{\partial^2 A_{\mathrm{s}}^{\pm}}{\partial t^2} + \frac{\alpha_{\mathrm{s}}}{2}A_{\mathrm{s}}^{\pm} - \frac{\Delta A_{\mathrm{s}}^{\mathrm{Rayleigh}}}{\Delta z} = i\gamma_{\mathrm{s}}\left|A_{\mathrm{s}}^{\pm}\right|^2 A_{\mathrm{s}}^{\pm} + \frac{g_{\mathrm{s}}(\omega)}{2}\left(\left\langle\left|A_{\mathrm{p}}^{\pm}\right|^2\right\rangle + \left\langle\left|A_{\mathrm{p}}^{\mp}\right|^2\right\rangle\right)A_{\mathrm{s}}^{\pm}, \tag{1.22}$$

where A is the complex field envelope, t is the time in a frame of reference moving with the pump, $\beta_{1\mathrm{s}}$ is a difference between pump and generation Stokes waves inverse group velocities, β_2, α, γ and g are GVD, linear attenuation, Kerr and Raman coefficients, ω stands for angular frequency. Note that operator g is applied in the frequency domain. Sign "±" denotes counter-propagating waves, indices "s" and "p" denote Stokes and pump waves, z is a longitudinal coordinate ($z = 0$ for starting point and $z = L$ at the other end of the fibre). In these coordinates every coordinate value z for "+" wave corresponds to the value $L - z$ for "−" wave and vice versa. White noise should be used as an initial condition to take into account spontaneous Raman emission [145]. Unlike in conventional lasers, where the spectral properties of radiation are mostly defined by the spectral profile and group delay of the mirrors forming the cavity, in Raman RDFLs Raman gain profile should be taken into account to correctly model the spectral properties. This could be done by explicitly defining the Raman gain profile of a given fibre or by some approximation. For example parabolic: $g_i(\omega) = g_i - k\omega^2$, where k is in ps²/W/km and i = "s" or "p" for Stokes and gain wavelength correspondingly. Rayleigh scattering is the scattering on sub-micron scale refractive index inhomogeneities, so the scattering strength is changed randomly on micrometer scale dis-

tances over the longitudinal coordinate. It is a real challenge to take into account micron scale random scattering over tens of kilometres of fibre length. This requires an enormous number of numerical integration steps, with the total duration of only one run of laser simulation taking 10^6 days if done in a straight-forward way. However, NLSE-based description of an RDFL which operates via random Rayleigh scattering, including spectrum properties of the generation is still possible, if only an average energy income is taken into account, and results in good quantitative description of an RDFL power performance within the power balance model [113, 130]. Indeed, from the power balance model it is known that the generation power of a real RDFL is well described by the average backscattering coefficient ε without taking into account random strength of the scattering on a micrometer scales [113]. The NLSE approach has to provide good predictions of the generation power at first, and provide spectral and statistical properties in addition.

To numerically implement this approach in a straight-forward way, one should save the spectra of the counter-propagating wave in each z-point and use these spectra for the next iteration when counter-propagating wave transmission is modelled. However such an "idealistic" approach requires quite big operative memory to save spectra at each step of numerical simulation. For example, for a typical number of numerical steps over the fibre length of 35000, one needs over 32 Gb of operative memory. The higher the generation power the lower the nonlinear length, and, consequently, the lower the integration step, so even bigger memory is needed. To meet this technical challenge, the spectra of the generated waves are saved at a small number N of equally spaced z-points, during each iteration. Since the counter-propagating wave is saved only in small number of points, a staircase function $z_{\text{prox}}(z)$ which approximates z with a set of N steps, each of them is a z-coordinate of the closest point where spectra of "$-$" wave is saved in the previous iteration. The number N is chosen so at higher values the spectrum of the generation does not change. In such a way a random fibre laser of any length operating at any practical power could be effectively simulated.

The next step of random fibre laser description is to take into account the correlation properties of the Rayleigh scattering [146]. Correlation properties could be important and could potentially change the overall statistical properties of the radiation, and, probably,

provide some correction to spectral properties, however they are not treated within this model, and only a random phase factor $e^{i\phi_0+i\omega\tau_0}$ with random phase ϕ_0 and time shifts τ_0. The Rayleigh term $\Delta A_s^{\text{Rayleigh}}$ is given by the equation:

$$\Delta A_s^{+\text{Rayleigh}} = \left(\varepsilon \Delta z \frac{\int_{-\infty}^{+\infty} d\omega \left| A_s^- \left(L - z^+ \right) \right|^2}{\int_{-\infty}^{+\infty} d\omega \left| A_s^- \left(L - z_{\text{prox}}^+ \right) \right|^2} \right)^{1/2} A_s^- \left(L - z_{\text{prox}}^+ \right) e^{i\phi_0+i\omega\tau_0} \tag{1.23}$$

where $\varepsilon = 4.5 \cdot 10^{-5}$ km^{-1} is Rayleigh scattering coefficient, which depends on fibre NA and fabrication method [147], Δz is an integration step.

Even though Raman scattering is a polarisation dependant effect, it has been known from previous works on long Raman fibre lasers that scalar models could describe their operation very well. There are vector models [148] used to describe the Kerr effect and birefringence induced instabilities in Raman fibre lasers, but generally use of such much more complicated models is not justified. Described above scalar numerical model could give good qualitative and quantitative results, however it should be noted that there are some effects that are not considered within this model, but which can affect laser properties in some cases:

- Raman gain response time, which is really important in supercontinuum generation. As the response time is of an order of 100 fs, this model cannot describe any time dynamics faster than 1 ps
- XPM with pump wave (despite XPM-induced noise transfer from pump to Stokes wave is experimentally observed in radio frequency beating spectrum in conventional Raman fibre lasers, so it tends to be important for noise properties of RDFLs also)
- Stimulated Brillouin scattering which is observed in experiments near the generation threshold [105]
- Parasitic reflection from fibre ends (it is known from experiments that reflections as low as 10^{-4} could substantially change RDFL's power [130])

1.4 Acoustic Response in Optical Fibres

The electric field of any pulse propagating in an optical fibre deforms the fibre material through the electrostriction process. This deformation excites an acoustic wave, which propagates outward from the fibre core to the cladding. Fibre material density variation associated with the deformation causes small variations of the refractive index. The optical field following the initial pulse will experience these variations and change its speed due to dispersion, which will result in pulse interaction and repositioning in the cavity. This effect can be very important for stability of mode-locked and particularly harmonically mode-locked fibre lasers and timing jitter of optical pulses in soliton communication systems.

The excitation of an acoustic wave by a short light pulse and consequent perturbation of the refractive index was first derived by Dianov *et al.* [149], and later repeated by others [150, 151]. Jaouën *et al.* were the first to include the response into an NLSE [152]. The derivation of the refractive index perturbation induced by optical pulses and mediated by transverse acoustic waves will closely follow that of Dianov *et al.* [149] and Jang *et al.* [150,151].

The material density variation caused by electrostriction leads to a change in the dielectric constant ε, which maps into a change of the refractive index:

$$\Delta n(t,x,y) \approx \frac{1}{2n}\frac{\partial \varepsilon}{\partial \rho}\rho(t,x,y) \tag{1.24}$$

where n is the unperturbed material refractive index and ρ is the density variation from the average density ρ_0 of the fused quartz. Taking into account only dominant pure radial acoustic modes and neglecting mixed torsional-radial modes, the density variation $\rho(t,x,y)$ can be found by solving the radially symmetric acoustic wave equation:

$$\frac{\partial^2 \rho}{\partial t^2} - v^2\nabla^2\rho - 2A\nabla^2\frac{\partial \rho}{\partial t} = -\frac{\gamma_e I(t)}{2cn}\nabla^2\left[\psi^2(r)\right]. \tag{1.25}$$

Here v is the longitudinal speed of sound, ∇^2 is the transverse Laplacian, A is the sound viscous attenuation constant, $\gamma_e = \rho_0\dfrac{\partial \varepsilon}{\partial \rho}$ is the electrostrictive constant and $I(t)$ is the time dependence of the optical intensity. We can neglect the longitudinal gradients of light, be-

cause longitudinal dimensions of the light pulse is much larger than the transverse size. For example 1 ps pulse in single mode fibre has longitudinal dimension of approximately 200 μm and field mode diameter of 3–6 μm. The spatial profile of the radially symmetric fundamental fibre mode $\psi(r) = \exp\left(\frac{-r^2}{w^2}\right)$ we assume to be Gaussian with w mode-field radius.

Since the right hand side of Equation 1.25 depends only on the modulus of r, the solution can be expressed as the sum of acoustic eigenmodes:

$$\rho(t, r) = \sum_{m=1}^{\infty} A_m(t)\psi_m(r), \tag{1.26}$$

where the radial acoustic wave functions have the form $\psi_m(r) = M_m J_0(\mu_m r)$, with J_0 the zeroth-order Bessel function. Assuming that the displacement vector on the cladding boundary and the corresponding stress tensor components are continous, the condition for the eigenvalues μ_m is:

$$(1 - \alpha^2)J_0(\mu_m R_{\text{clad}}) - \alpha^2 J_2(\mu_m R_{\text{clad}}) = 0 \tag{1.27}$$

where R_{clad} is the fibre cladding radius, J_2 is the second order Bessel function, and $\alpha = v_s/v$ with v_s the acoustic shear velocity. The coefficients M_m are defined with the help of normalisation condition:

$$\int_0^R \int_0^{2\pi} \psi_n(r)\, \psi_m(r) r \, \mathrm{d}r \, \mathrm{d}\phi = \delta_{nm}. \tag{1.28}$$

The time-varying part of the acoustic eigenmodes $A_m(t)$ is obtained by Fourier transforming Equation 1.25 and integrating over the spatial profiles:

$$A_m(t) = \frac{\gamma_e B_m}{2cn} \mathcal{F}^{-1}\left[\frac{\tilde{I}(\omega)}{\omega^2 - v^2\mu_m^2 - i2A\omega\mu_m^2}\right], \tag{1.29}$$

where $\tilde{I}(\omega)$ is the Fourier transform of the optical intensity, and B_m are the overlap integrals

showing effectivity of the m-th acoustic mode excitation by the optical radiation:

$$B_m = \int_0^R \int_0^{2\pi} \nabla^2 \left[\psi^2(r)\right] \psi_m(r)\, r\, \mathrm{d}r\, \mathrm{d}\phi \tag{1.30}$$

rewriting Equation 1.29 as a convolution in the time domain:

$$A_m(t) = \frac{\gamma_e B_m}{2cn} \left[I(t) \star \delta A_m(t)\right], \tag{1.31}$$

where $\delta A_m(t)$ is calculated using the residue theorem and is given by:

$$\delta A_m(t) = -\frac{\sin(\Omega_m t)}{\Omega_m} \exp(-\Gamma_m t) H(t), \tag{1.32}$$

with $\frac{1}{\Gamma_m}$ and $\Omega_m = \sqrt{v^2 \mu_m^2 - \Gamma_m^2}$ are, respectively, the decay time and the frequency of the m-th acoustic mode, and $H(t)$ the Heaviside step function. Substituting all the quantities into Equation 1.26 and combining with the Equation 1.24, we obtain:

$$\Delta n(t, r) = \frac{\gamma_e^2}{4cn^2\rho_0} \sum_{m=1}^{\infty} B_m \left[I(t) \star \delta A_m(t)\right] \psi_m(r). \tag{1.33}$$

The perturbation of the refractive index of the fibre material leads to a change in the propagation constant and can be evaluated using the perturbation theory [153]:

$$\delta n_{\mathrm{eff}}(t) = \frac{1}{D} \int_0^{2\pi} \int_0^{\infty} \Delta n(t, r) \psi^2(r) r\, \mathrm{d}r\, \mathrm{d}\phi = \tag{1.34}$$

$$= \frac{\gamma_e^2}{4cn^2\rho_0 D} \sum_{m=1}^{\infty} B_m C_m \left[I(t) \star \delta A_m(t)\right], \tag{1.35}$$

where D:

$$D = \int_0^{2\pi} \int_0^{\infty} \psi^2(r) r\, \mathrm{d}r\, \mathrm{d}\phi \tag{1.36}$$

and C_m is the overlap integral showing effectivity of light scattering by the m-th acoustic

mode:

$$C_m = \int_0^{2\pi} \int_0^R \psi^2(r)\psi_m(r) r \, \mathrm{d}r \, \mathrm{d}\phi \tag{1.37}$$

By introducing a complex field pulse envelop $A(t)$ such that $|A(t)|^2 = I(t)D$ is instantaneous power, we can rewrite Equation 1.35:

$$\delta n_{\text{eff}}(t) = |A(t)|^2 \star \delta n(t) \tag{1.38}$$

where $\delta n(t)$ is the instantaneous response function of electrostrictional interaction:

$$\delta n(t) = -\frac{\gamma_e^2}{4cn^2\rho_0 D^2} \sum_{m=1}^{\infty} B_m C_m \frac{\sin(\Omega_m t)}{\Omega_m} e^{-\Gamma_m t} H(t). \tag{1.39}$$

On the Figure 1.15 the numerically calculated response function $\delta n(t)$ is presented, with the following fibre parameters used: $\rho_0 = 2210$ kg/m^3 is the density of silica [154], $\Gamma_m = 3 \cdot 10^7$ s^{-1} is the acoustic dumping coefficient which is assumed the same for all modes [149], $w = 3.2$ µm is the field mode radius, $v = 5996$ m/s and $v_s = 3740$ m/s is the longitudinal and shear velocity of sound [155,156], $\gamma_e = 0.902$ is the electrostrictive constant [154], $R_{\text{clad}} = 62.5$ µm is the fibre cladding radius, and $n = 1.47$ is the refractive index. It is worth noting that the strength of the effect is more than 3 orders of magnitude lower than the Kerr-induced index change and even smaller than the longitudinal index variations frozen into the fibre during the manufacturing. However, the effect still can play an important role in mode-locked laser dynamics, as it will be shown later.

The calculated instantaneous response function of the electrostrictive interaction can be easily incorporated into NLSE [5,152,157]:

$$\frac{\partial A}{\partial z} + i\frac{\beta_2}{2}\frac{\partial^2 A}{\partial t^2} + \frac{\alpha}{2}A = i\gamma_K |A|^2 A + i\frac{2\pi}{\lambda}\left[|A|^2 \star \delta n(t)\right] A, \tag{1.40}$$

where A is the complex field envelop, γ_K is the Kerr nonlinearity, and λ is the carrier wavelength.

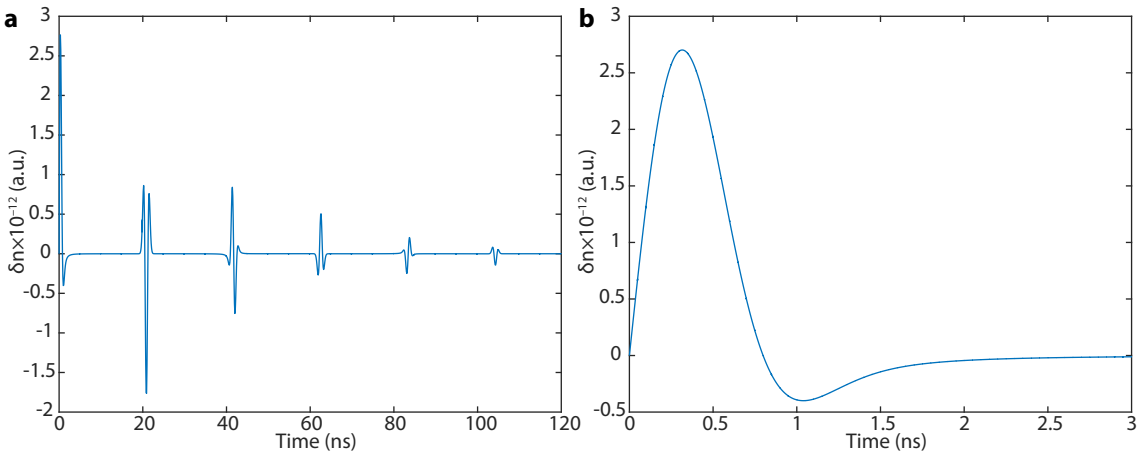

Figure 1.15: a, Theoretical impulse response of the refractive index acoustic perturbation. **b,** The first peak of the acoustic response.

1.5 Spatio-temporal Representation of Laser Generation

Analysis of the properties of lasers plays an important role in understanding the underlying physical mechanism. Novel methods for investigation are being developed everyday. One well known representation of laser dynamics – spatio-temporal representation, or $I(t, z)$. It has been a standard tool in numerical simulations, as it is very straightforward to construct, but presented a fairly difficult technological challenge for experimental data. In this section the methods of construction of spatio-temporal representation from an experiment will be described.

To understand how to present the output laser dynamics as a spatio-temporal evolution, we need to look at the laser design Figure 1.16a. Most of the laser designs have an intrinsic characteristic periodicity in their output dynamics associated with the boundary conditions, i.e. the length of the cavity. In case of fundamentally mode-locked lasers it is the pulse repetition rate, the reciprocal value of the round-trip time in the cavity for the pulse. For pulsed lasers it is fairly obvious and a simple experimental task – to construct the spatio-temporal representation, or round-trip picture. All is required just to trigger the oscilloscope with the front of the pulse. Although it is technically simple, it can lead to imprecisions and lost information, such as the jitter figure. The change in amplitude or shape of the pulse will affect the triggering also. All these factors make the applicability of this method quite limited, and impossible for the CW, and harmonically mode-locked lasers. To solve this problem we need to exclude the triggering problem. To do this, we trigger the

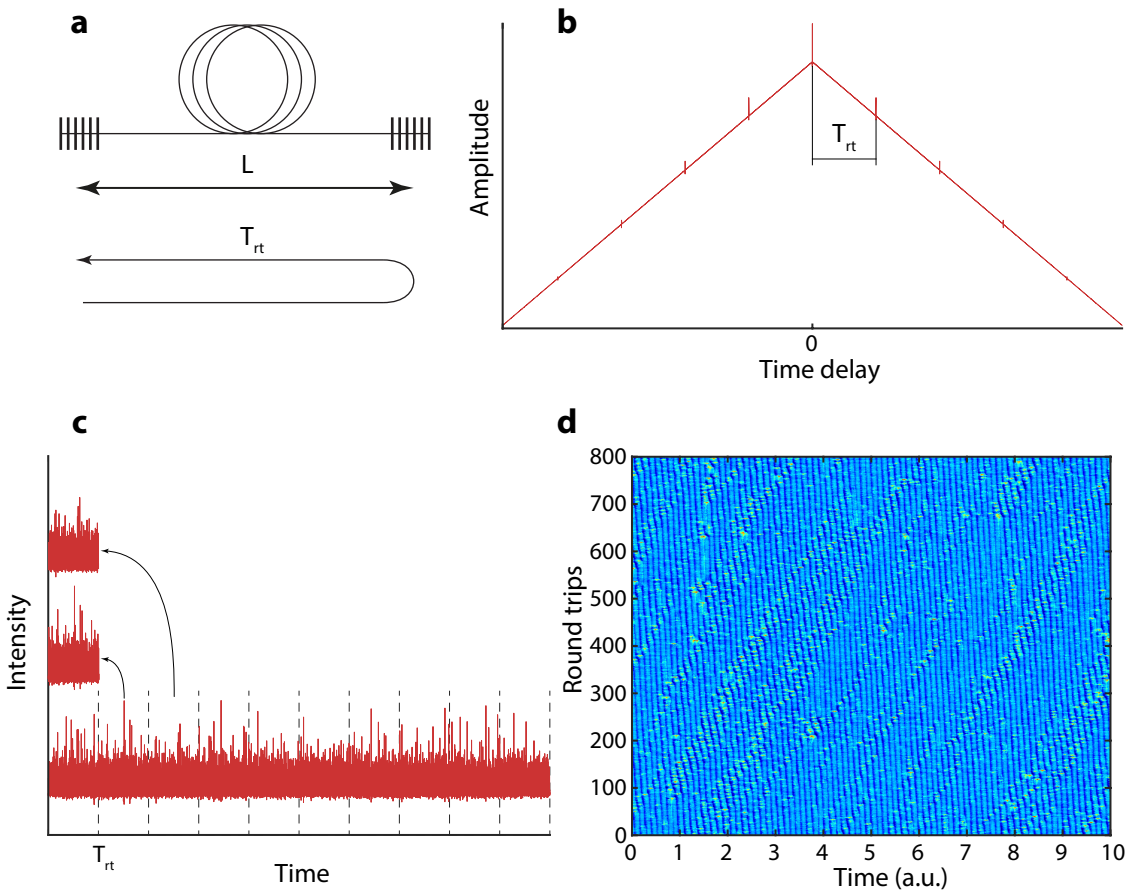

Figure 1.16: a, Schematic representation of a laser cavity length L. **b,** The autocorrelation function. **c,** Time trace sliced into pieces T_{rt} long. **d,** The resulting spatio-temporal representation of experimental time trace.

oscilloscope once and record the time trace as long as it is technically possible. The number of round-trips we can reconstruct from such time trace would depend on the following factors: the cavity length L, the sampling rate of the oscilloscope in samples per second S, and the memory depth in samples M. The number of the round-trips we can reconstruct is $N = \frac{2cM}{nSL}$, where c is the speed of light, and n is the refractive index of the media (optical fibre in this case). As we can see from the formula for lasers with high cavity length, longer memory depth is required for the same sampling rate, which is directly connected to the chosen bandwidth of our measurements.

To construct the round-trip picture we first need to find the round-trip time. Even though it seems to be a simple task, there are some nuances than can drastically change the final picture. For example measuring mode distance from RF measurements of the

laser intensity and taking its reciprocal would give us a round-trip time, but this might not always give us the desired result. When round-trip time expressed in terms of number of sampling points of the given oscilloscope, even 1–2 point error over 700000 points long round-trip would give us a skewed distorted picture. The much easier and more precise way to do it is to calculate an auto-correlation function (ACF) of a time trace 4–10 round-trips long Figure 1.16b. The distance between zero-delay central peak and the next highest peak will correspond to the cavity round-trip time. Another convenience of this method is that we obtain the result in terms of sampling points, which simplify further processing.

After finding the number of points K corresponding to the round-trip time we cut our long time trace into blocks K points long, and stack them together into a matrix. This matrix will then represent the spatio-temporal dynamics of the laser. Due to limited bandwidth of scopes, and correspondingly low sampling rate, we can't always express a cavity round-trip time in integer number of points. Most of the time this will manifest itself in skewed, angled picture. Basically it just means that we are travelling in the time-frame which speed is higher or lower than that of a group velocity of the structures under study. One should always consider this measurement limitation when study the experimental spatio-temporal representation of laser radiation.

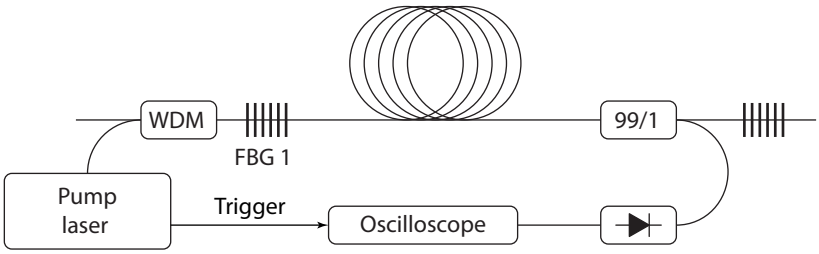

Figure 1.17: Switch-on technique

The power of this technique is in its versatility. Any laser radiation with intrinsic periodicity can be represented in spatio-temporal domain. Another important fact is that there is no "dead" time, no information is lost, compared to the case where the oscilloscope is triggered by the front of the periodic structure. This allows us to follow any structure present in the cavity, or observe transitions in the laser dynamics. For example "switch-on" dynamics Figure 1.17, where the pump power activation and following intra-cavity radiation build-up

is registered in all details. This allows us to study complex interactions and formation of structures in the laser radiation.

Chapter 2

Spatio-temporal Regimes of Generation of Raman Fibre Lasers

The experimental technique of construction of spatio-temporal dynamics described in the previous section allows us to define "space" and "time" coordinates in one dimensional systems such as a fibre laser [158]. Indeed, as a light packet with duration t travels inside a resonator, the radiation corresponding to this packet outcoupled from the resonator will be periodical with the period corresponding to the round-trip time τ_{rt}. Following the evolution of this light packet we can construct a function of continuous variable within the time frame moving with the light packet denoted t, and a discrete variable $T = N \times \tau_{\mathrm{rt}}$, where N is the number of round trips. The fastest process in linear propagation with the speed of light c, so the t dependence by the transform $t - \frac{x}{c}$ represents the dependence on the spatial coordinate x along the resonator. In this form slow evolution coordinate T has the meaning of time, while the fast evolution coordinate t is equivalent to the longitudinal spatial coordinate x. Treated in such a way it allows to draw meaningful comparisons between fibre optics and for example hydrodynamics, which will be discussed in the following section.

2.1 Laminar and Turbulent Regimes of Generation

The problem of coherence destruction has importance beyond optics and photonics. Laminar flow destruction in a pipe has huge practical implications. The sudden transition radi-

cally changes transport efficiency, which can incur increased transportation costs and even damage. The problem of studying such laminar-turbulent transition is the practical difficulty of measuring the parameters of the flow in a real pipe. Experiments can take years to gather high enough statistics and obtain viable experimental results [159]. Studying the radiation properties of a one dimensional laser system is much more amenable problem. Huge statistics and data sets can be acquired in a matter of days. This makes it an invaluable tool for study of processes and transitions in a laser bearing similarities with other physical systems. The apparent similarity between NLSE and Navier-Stokes equation further allow us to draw reasonable comparisons between the laser dynamics and a pipe flow and greatly simplify modeling, as NLSE is much more susceptible to numerical treatment.

In normal dispersion fibres, a coherent monochromatic wave is stable with respect to modulation instability (MI) [5], so it is theoretically possible to achieve a classical wave condensation in the limit of low four-wave mixing interaction between cavity modes. However, in long fibre lasers the number of cavity modes can reach 10^6–10^7, and due to even slight variations in amplitude and phase of these modes the quasi-CW operation mode has stochastic nature. Considering the huge number of modes interacting in the laser cavity, the description of such interactions should be done in terms of wave turbulence [16, 160].

2.1.1 Experiment and Results

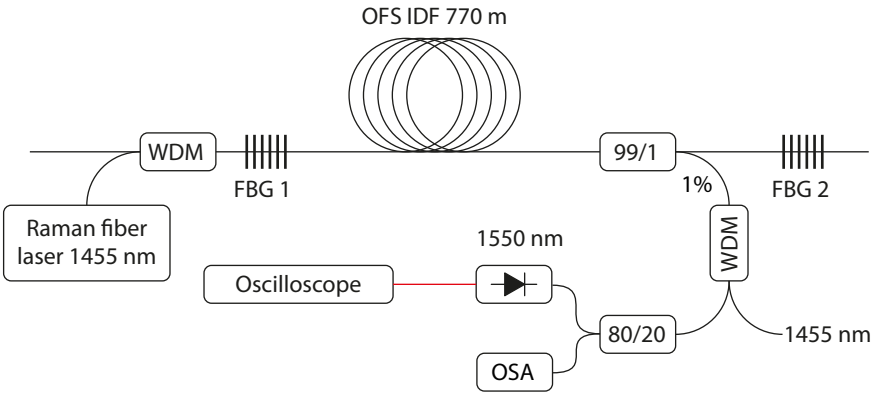

Figure 2.1: The experimental setup.

To study the laminar-turbulent transition an experimental setup was proposed and re-

alised Figure 2.1. The laser cavity consisted of 770 m normal dispersion ($D = -44\frac{\text{ps}}{\text{nm}\cdot\text{km}}$) OFS IDF fibre and two super Gaussian FBGs, which profiles are shown of the Figure 2.2. The gratings were specifically designed for this experiment, with full width at half maximum (FWHM) of 1.2 nm, and flat group delay. The minimal dispersion of the gratings is very important to minimise the phase scrambling with each reflection from the mirrors. The radiation coming from the cavity was monitored from the 1% port of 99/1 coupler, with residual pump filtered out by a 1455/1550 WDM coupler. A 50 GHz DC photodetector and 36 GHz digital sampling oscilloscope were used to register the temporal dynamics, and a grating based optical spectrum analyser Yokogawa AQ6370C registered the output optical spectrum. The cavity was pumped by a 1455 nm low relative intensity noise (RIN) Raman fibre laser capable of delivering up to 5 W of optical power.

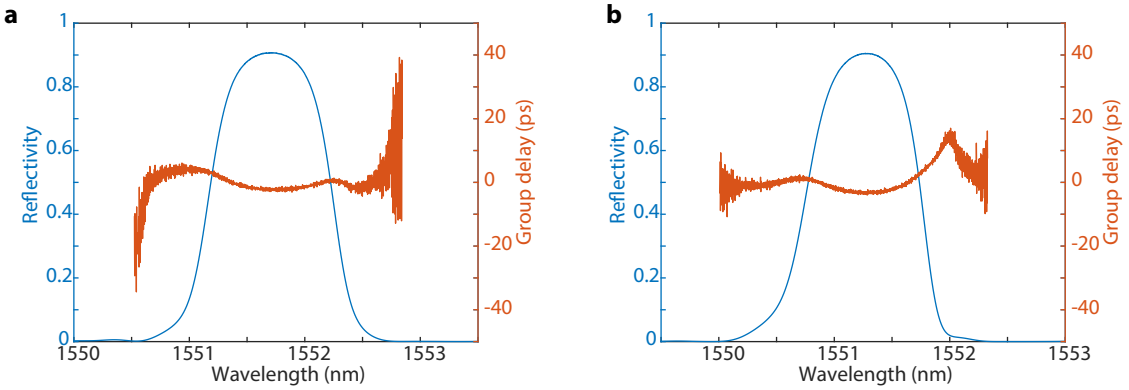

Figure 2.2: The reflection spectra and group delay profiles of the first **a,** and the second **b,** specially made second order super Gaussian gratings.

To observe the laminar-turbulent transition the pump power was changed in the region of 0.8–1.9 W. At lower pump powers, 0.8–1.1 W the laser operated in the laminar regime, which was characterised by the narrow spectrum (Figure 2.3) and narrow field intensity probability distribution function as expected for the coherent state Figure 2.4a inset. It is important to note that the low RIN of the pump played a crucial role in achieving the laminar regime of generation, as RIN is transferred to the Stokes radiation through the XPM process. Immediately after the transition into turbulent regime, which occurs once the pump power crosses 1.1 W threshold and corresponds to the reduction of the coherence in the system, the optical spectrum becomes twice as broad compared to the laminar regime Figure 2.3, and broadens further as the pump power increases.

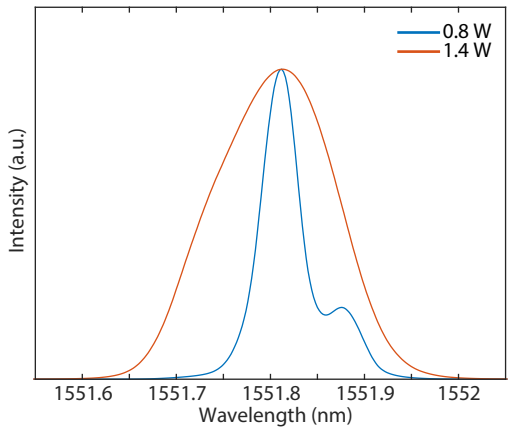

Figure 2.3: The optical spectra for the laminar (blue 0.8 W) and the turbulent (red 1.4 W) regime of generation.

In the temporal domain a well defined mean level with Gaussian distributed fluctuations could be seen for the laminar regime of generation (Figure 2.4a). High intensity events were still present in the cavity due to residual polarisation fluctuations, which contributed to the phase scrambling. Even though the setup was in a temperature and noise stable environment, it is a very difficult task to completely eliminate the polarisation noise in a single mode non polarisation maintaining fibre 770 m long cavity. The temporal dynamics in the turbulent regime (Figure 2.4b) are characterised by high intensity events, which reflected in a near exponential long tail of the PDF, while the mean value of the distribution almost doesn't change. The increased intensity fluctuations can be attributed to the more effective four-wave mixing process between the cavity modes at higher powers.

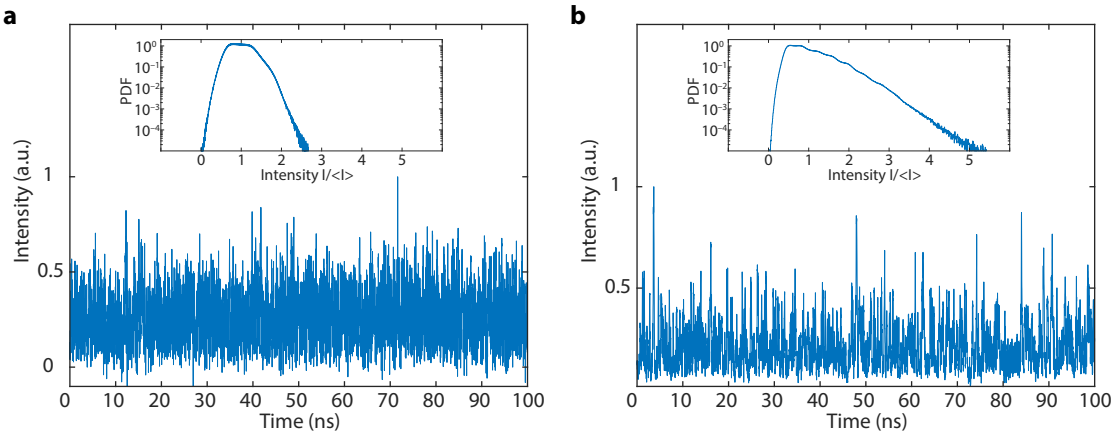

Figure 2.4: Temporal dynamics and corresponding intensity PDFs for the **a,** laminar and **b,** turbulent regimes of generation.

In the spatio-temporal domain the transition is even more pronounced (Figure 2.5). In

the laminar regime (Figure 2.5a) dark coherent structures can be seen travelling at different speeds across a relatively uniform laminar background. These structures are in fact dark and grey solitons, which are analytical solutions of the one-dimensional NLSE in the case of normal dispersion. In the laminar state these dark solitons survive in the cavity for many hundreds of round-trips, which is equivalent to a propagation distance of hundreds kilometres. In the turbulent regime (Figure 2.5b) the lifetime of the dark solitons is reduced to tens of round-trips, as they accelerate and bunch together. Indeed the destruction of the coherent state can be explained by the proliferation and clustering of the dark solitons, which is clearly evidenced in the spatio-temporal representation. The coherent laminar background is broken into bright puffs by the clusters of dark solitons. These puffs have characteristic rhombic shape, and decrease in size, as pump power increases.

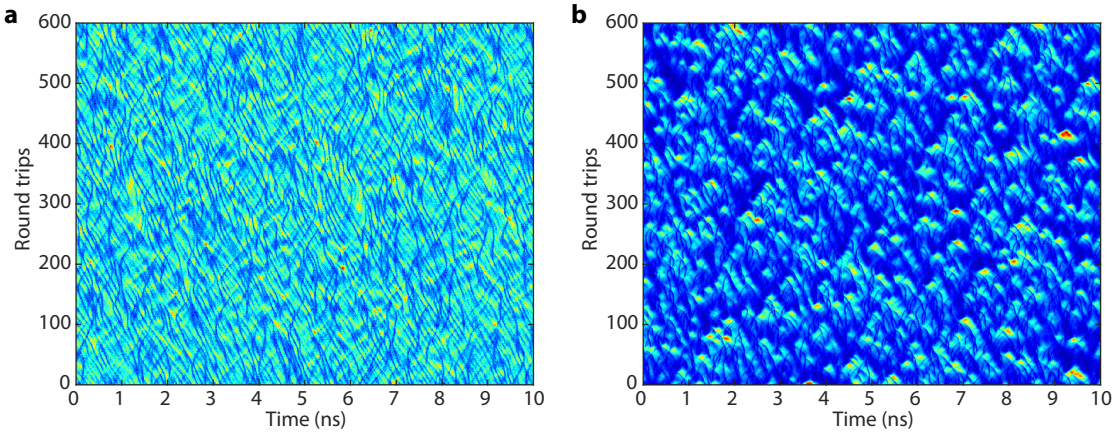

Figure 2.5: a, The spatio-temporal representation of the laminar, and **b,** turbulent regime of generation.

If we switch the pump power instantly (in less than 200 ns in experiment) we can observe the switch-on build-up of the radiation in the cavity for both laminar and turbulent regime of generation. For laminar Figure 2.6a regimes it takes about 50 round-trips for radiation to build-up, and after that we can see brighter more intense regions for another 50 round-trips, with regular picture after that. There is no gradual transition or emergence of dark solitons. Similarly in the turbulent regime (Figure 2.6b), with the only difference that radiation builds-up in the cavity much faster due to higher pump power and correspondingly gain.

In conclusion, fibre lasers, and Raman fibre lasers in particular provide an invaluable

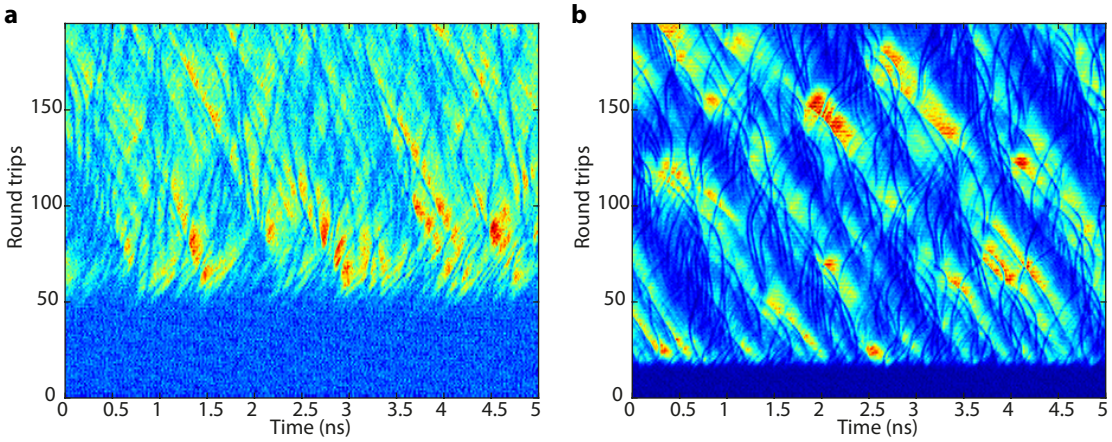

Figure 2.6: a, Switch-on dynamics for of the laminar, and **b,** turbulent regime of generation.

platform for observation of states and transitions which are similar to the states and transitions in other fields of physics, such as hydrodynamics. Providing a highly flexible comparatively inexpensive platform for studying complex processes and interactions. In this particular experiment two distinctive regimes of generation – laminar and turbulent, allow to study the transition which is similar to destruction of the laminar flow in a pipe. The mechanisms responsible for the condensate destruction were identified.

2.2 Power Dependence of Spatio-Temporal Regimes of Raman Fibre Laser

As was discussed in the section 2.1 – the Raman fibre laser (RFL) is a great platform for the demonstration of nonlinear physics. High Raman gain and cavity lengths from hundreds of meters up to tens of kilometres create perfect conditions for nonlinear effects to develop. Even the slightest variation of the parameters can lead to a qualitative change in the generation regime of the laser. In this section we will look into other possible regimes of generation of RFLs with a normal dispersion cavity. As it was shown in the laminar and turbulent regimes of generation, spatio-temporal dynamics can uncover processes that are impossible to observe from time intensity dynamics alone, such as dark soliton interactions and clustering. This raises a question, if other regimes of generation can be distinguished from the spatio-temporal point of view. As nonlinear interaction depends on the intensity of the co-propagating waves, the spatio-temporal dynamics of laser radiation would change with

power, in which case we can talk about power dependence of the spatio-temporal regimes of generation of RFLs.

Raman fibre lasers have stochastic time dynamics, and while they are CW on millisecond time scales, on sub-ns time scale the properties of quasi-CW radiation are defined by the coexistence of large number on longitudinal modes. All these modes have independent fluctuating amplitudes and phases [13] and interact through four-wave mixing process, generating new spectral components, contributing to the broadening of spectrum. These fluctuations can be described in the limit of Gaussian statistics within the model of optical wave turbulence [16]. This approach proved to be very powerful [161] and found many applications, being capable to describe complex processes such as supercontinuum generation [162], the operation of random feedback Raman fibre lasers [163], and the emergence of optical rogue waves in the generation of quasi-CW lasers [12, 161, 164, 165]. Turbulent-like generation in fibre lasers could be also modelled within the Ginzburg-Landau equation [166].

The real statistical properties of radiation of quasi-CW RFLs could differ from Gaussian statistics [13]. Residual mode correlations result in deviations of statistics from Gaussian making the intensity dynamics not completely stochastic. Residual mode correlations could also lead to partial mode-locking in RFLs. In [167] a pulsed laser is demonstrated. The laser was reported to be very hard to adjust and unstable. Another work [168] reported a partially mode-locked RFL generating noise-like pulses of 2.5 ns width which are filled by an irregular bunches of shorter pulses. Intermode beating harmonically mode-locked RFLs generating tens of nanoseconds long noise-like pulses was reported in [169,170]. Properties of such partially mode-locked regimes are usually hard to assess in temporal measurements. The concept of spatio-temporal evolution was used to experimentally study various systems including observation of long-range interaction of solitons [151], specific dynamics in passively mode-locked lasers [171–174].

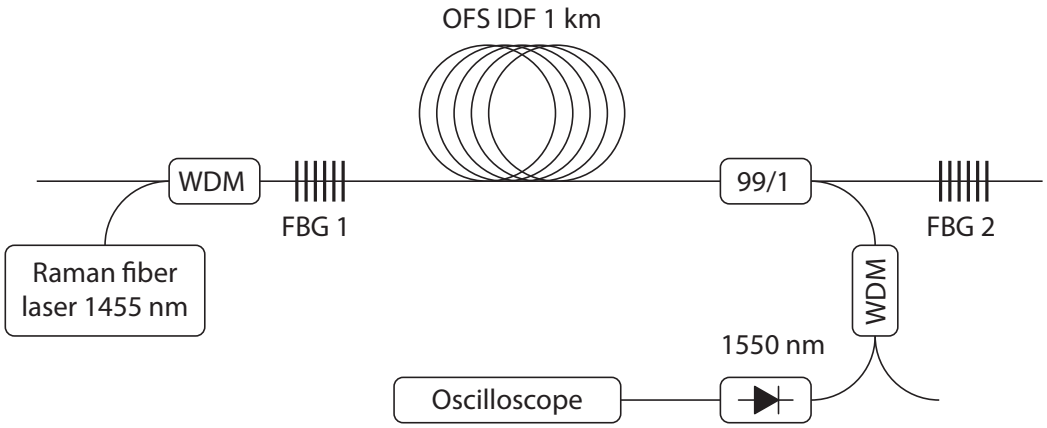

Figure 2.7: The experimental setup used for observation of power dependence of spatio-temporal regimes of generation.

2.2.1 Experiment and Results

To investigate other spatio-temporal regimes of generation a Raman fibre laser was constructed Figure 2.7. The cavity was formed of 1 km of OFS IDF fibre with normal group velocity dispersion $D = -44\frac{\text{ps}}{\text{nm}\cdot\text{km}}$, and two highly reflective FBGs with spectral width of 1.2 nm and super Gaussian profile Figure 2.2. The pump radiation at 1450 nm from an IPG RFL was coupled into the laser cavity through a WDM coupler. The setup lases at 1550 nm owing to the Raman gain. The output intensity dynamics were registered from the 1% rejection port of 99/1 coupler by 50 GHz DC photo-detector and 6 GHz digital sampling oscilloscope. The setup is unchanged from the experiment on observation of laminar-turbulent transition for the most part, apart from cavity length and the pump source. These changes however make it impossible to observe laminar regime of generation in this experiment, as higher RIN figure of the pump and greater interaction length contribute to the destruction of the condensate.

In the experiment very long time traces $I(t)$ of length up to 128 million points were measured, which corresponds to 3.2 ms in time, i.e. more than 320 round-trips. The intensity dynamics of the quasi-CW RFL depend on the pump power, (Fig. 2.8). At all pump power levels the time dynamics look irregular, only near the generation threshold some periodicity could be seen (Figure 2.8a).

From such intensity dynamics alone, it is impossible to distinguish the difference in the generation regimes of the laser if any exists. The measured intensity PDF could provide ad-

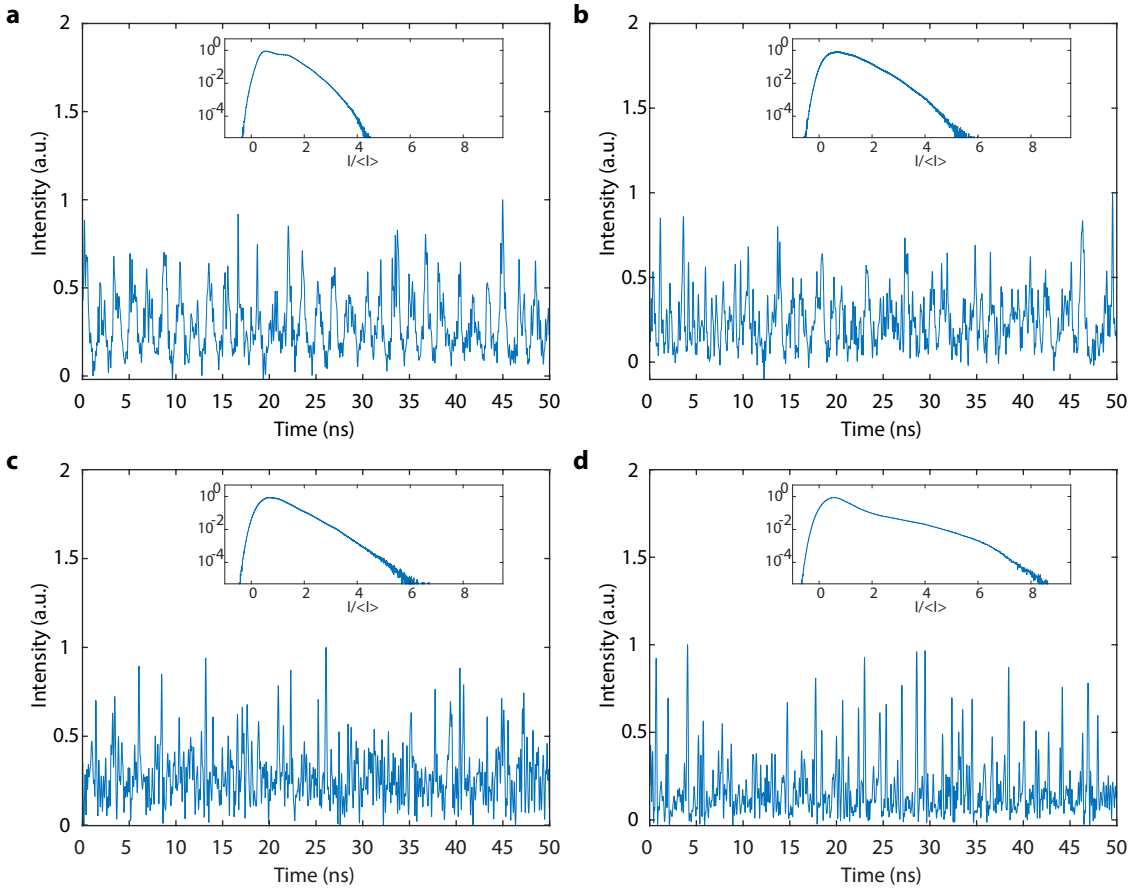

Figure 2.8: Temporal dynamics and probability density functions for different pump powers. All traces presented show stochastic nature of the output radiation, with the mean level of the signal being the only visually discriminable parameter, but not clear enough to determine the operational regime of the laser. **a,** 1.5 W of pump power, **b,** 2.0 W, **c,** 3.0 W, and **d,** 3.25 W

ditional information about the details of the generation regime, see insets in Fig. 2.8. Intensity PDF gradually develops an exponential tail when pump power increases and becomes broader revealing the generation of more intense events. The combination of intensity PDF measurements and intensity dynamics measurements, $I(t)$, still do not allow clearly reveal the difference in the generation regimes over power. It is worth mentioning that the limited electrical bandwidth of the measurement setup could influence quantitatively the observed time dynamics and statistical properties, but does not affect the measurements in qualitative way [175].

2.2.2 Two-dimensional Auto-correlation Analysis

The situation is completely different if the laser dynamics are analysed in the spatio-temporal domain, (Figure 2.9). In this case we can clearly distinguish between the generation regimes.

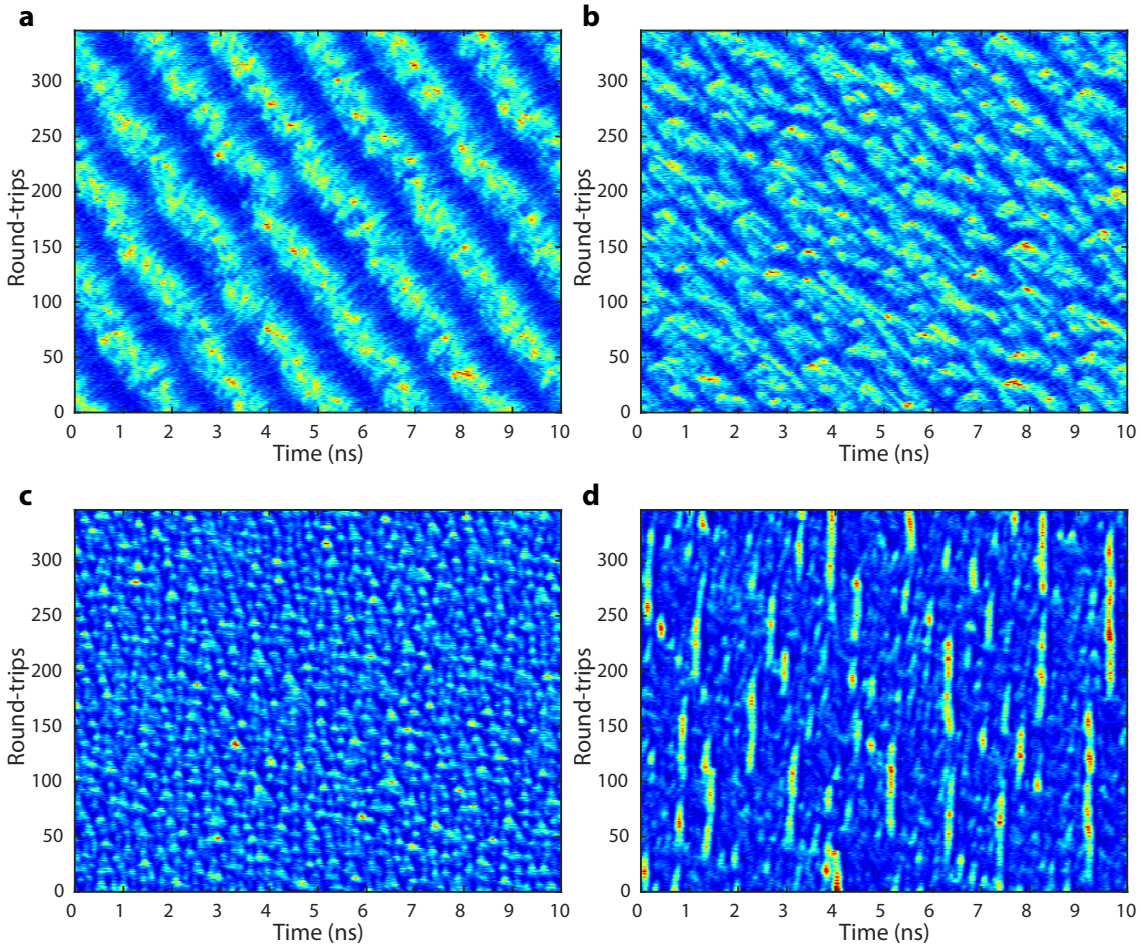

Figure 2.9: Spatio-temporal dynamics at different pump power levels. **a,** Partial mode-locking at 1.5 W. **b,** and **c,** Turbulent generation with of different spatio-temporal properties, at 2.0 W and 3.0 W respectively. **d,** Emergence of short-lived pulsed at 3.25 W.

Periodic modulation of the intensity observed at lower pump powers forms a distinctive spatio-temporal picture Figure 2.9a of clear dark and bright stripes. The angle of the picture can be attributed to the uncertainty of the measured round-trip time, which is the limitation of the oscilloscope used in the experiment. This pattern is the signature of partial mode-locking present in the system. Indeed, bright stripes indicate that structures of certain temporal width survive in the cavity over many round-trips. Well defined pulse repetition rate could be identified, even though the pulses are of noise-like structure. Despite the low bandwidth of the oscilloscope, dark solitons could be visible running across pulses. The mechanism responsible for this particular modulation frequency is not entirely clear, but it is possible that this regime could be potentially developed into a high-quality mode-locked regime if the cavity is designed in a specific way or additional appropriate saturable absorption mechanism is introduced into the cavity. Note that lasers operating

in similar temporal regime of partial mode-locking were previously reported in the literature [167–170, 176], however the spatio-temporal dynamics have not been analysed.

At higher power, the spatio-temporal dynamics change drastically, Figure 2.9b, as there is no periodicity present in temporal dynamics over fast time, or indeed over slow evolution coordinate. Despite the stochastic time dynamics $I(t)$, some localised bright structures are clearly visible in the spatio-temporal domain. It does resemble the turbulent regime observed previously in laminar-turbulent transition experiment, but they differ in one important moment – there is no clustering of dark solitons responsible for the turbulence. The transition to turbulence is not from laminar state, and so the mechanism is different. However the shape of the bright structures is similar to the previously observed. Further increase of the pump power leads to the change of spatio-temporal pattern and to the narrowing of bright structures both over temporal and evolution coordinates, Fig. 2.9c.

At the highest pump power of 3.25 W, completely different spatio-temporal regime is observed, Fig. 2.9d. The radiation is filled with some short-lived intense pulses which change the overall intensity statistics, see Fig. 2.8d. Such pulses are non-stationary and eventually dissipate, but they are quite-stable if compared to the round-trip time, surviving for up to a hundred round-trips. It is possible that the gain in the laser cavity with total normal dispersion becomes high enough to develop short high intensity pulses into parabolic structures similar to systems reported in [82, 84, 177, 178]. The mechanism of the formation of such pulses is described in more details in the chapter dedicated to the mode-locked Raman fibre lasers.

Measurements of the intensity spatio-temporal dynamics allow to perform more advanced analysis of the generation properties. For example, additional information about generation regime can be extracted from the two-dimensional auto-correlation analysis, $G_I(\tau, \xi) = \langle I(t, z) I(t + \tau, z + \xi) \rangle$, Fig. 2.10. The conventional one-dimensional intensity ACF, $G_I(\tau) = \langle I(t, z) I(t + \tau, z) \rangle$, is actually a cross-section of two-dimensional autocorrelation function $G_I(\tau, \xi)$ at fixed evolution coordinate z, see graphs on the top of panels on Fig. 2.10. One can also calculate the one-dimensional ACF function over evolution coordinate by fixing the fast time t in the way $G_I(\xi) = \langle I(t, z) I(t, z + \xi) \rangle$ to reveal periodicity properties and typical life-time of the structures, see graphs on the left of panels on Fig. 2.10.

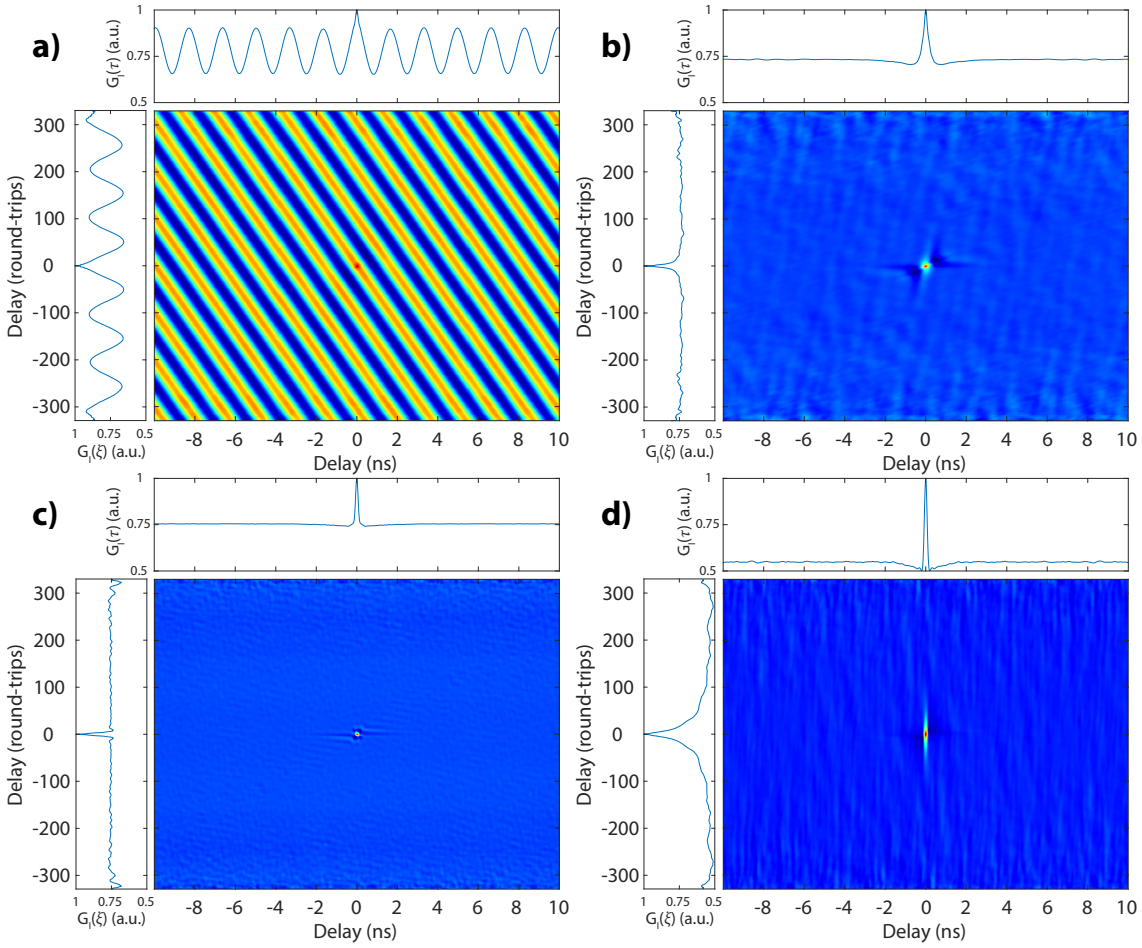

Figure 2.10: Two-dimensional auto-correlation functions $G_I(\tau, \xi)$, calculated from the measured intensity spatio-temporal dynamics for **a,** 1.5 W, **b,** 2 W, **c,** 3 W, and **d,** 3.25 W of pump power.

For the lowest used in the experiment pump power of 1.5 W, the two-dimensional ACF is stripe-like revealing well established periodicity in partially mode-locking regime, Fig. 2.10a. As was mentioned before the angle of the stripes is due to round-trip time measurement error and could be ignored. It does not affect the ACF calculated over the fast evolution time. The ACF period corresponds to the modulation frequency in time domain. The average width of the noise-like pulse could be well measured from 2D ACF: pulses are of 0.85 ns width which is a half of the period of the envelope. Note the red round dot at zero delay, which corresponds to the short sub-structure with very short lifetime. The width of the zero-delay peak (~100 ps) indicate the duration of the fast irregular sub-pulses structure. For turbulent regimes no obvious periodicity over evolution coordinate can be observed Fig. 2.10b–c. The width of the central peak over evolution coordinate provides an average lifetime of the structures which decreases while pump power increases. The temporal

width of a typical structure, ~300 ps at 2.0 W, Fig. 2.10b, is surprisingly larger than in partially mode-locking regime despite the generation power is higher. So the stochastic filling could be of different nature in these two regimes. At further pump power increase, the typical width of stochastic structure becomes smaller, down to 150 ps at 3.0 W, Fig. 2.10c, as one could expect as nonlinearity becomes stronger. However, even though the sampling rate of the oscilloscope is 40 GS/s, which means points are 25 ps apart, the bandwidth is just 6 GHz, which limits the duration of a structure that could be resolved to 160 ps. Note that there is still some background pattern in both turbulent regimes which properties were not analysed. Finally, at the highest observed power the two-dimensional ACF has a very different shape: there is a stripe-like central peak which width over evolution coordinate gives an average lifetime of the emerged pulses, Fig. 2.10d. Pulses live on average about 50 round-trips (which corresponds to the propagation length of 100 km) and are still ~150 ps wide over the fast time.

In conclusion different types of spatio-temporal dynamics were observed in the quasi-CW RFL. The regimes are varied from partial mode-locking to almost stochastic generation of different spatio-temporal patterns to emergence of short-lived pulses on the stochastic background. Despite intensity dynamics are very similar in temporal domain, the generation regimes differ substantially in their spatio-temporal properties, which means that the same laser depending on the pump power generates in a regime of noise-like pulses, in irregular turbulent regimes and in a regime of random short-lived intense pulses emerging from the stochastic background. The two-dimensional auto-correlation analysis allows to reveal periodicity properties both over time and evolution coordinate and track the changes in the average temporal width and life-time (over evolution coordinate) of emerged typical spatio-temporal structures over the pump power.

Chapter 3

Temporal and Spatio-temporal Dynamics of Mode-locked Raman Fibre Lasers

In this chapter some of the regimes described in the previous chapter will be looked into in more details. In particular the regimes where mode correlation were observed, which lead to periodic or pulsed dynamics in the temporal or spatio-temporal domain. In the first section the influence of the FBGs, which play the role of cavity mirrors, on spatio-temporal regimes of generation will be described. In the second section the spatio-temporal dynamics of mode-locked regimes achieved with these gratings will be presented.

3.1 Experimental setup

To simplify the description of each experimental fibre laser setup, some common parameters and components will be described briefly here and later referenced in the following sections. First of all the diagram of the experimental setup with all the equipment used in different configurations is shown on the Figure 3.1. This diagram covers every possible configuration described in this chapter, with some of the parts missing in one or another experiment. Most generally, the linear cavity was formed of two fibre Bragg gratings and a piece of single mode normal dispersion fibre. The pump radiation at 1455 nm was coupled into the cavity with the help of a WDM coupler, and the residual unabsorbed pump was decoupled out of the cavity after the fibre and before the output FBG to minimise the stress

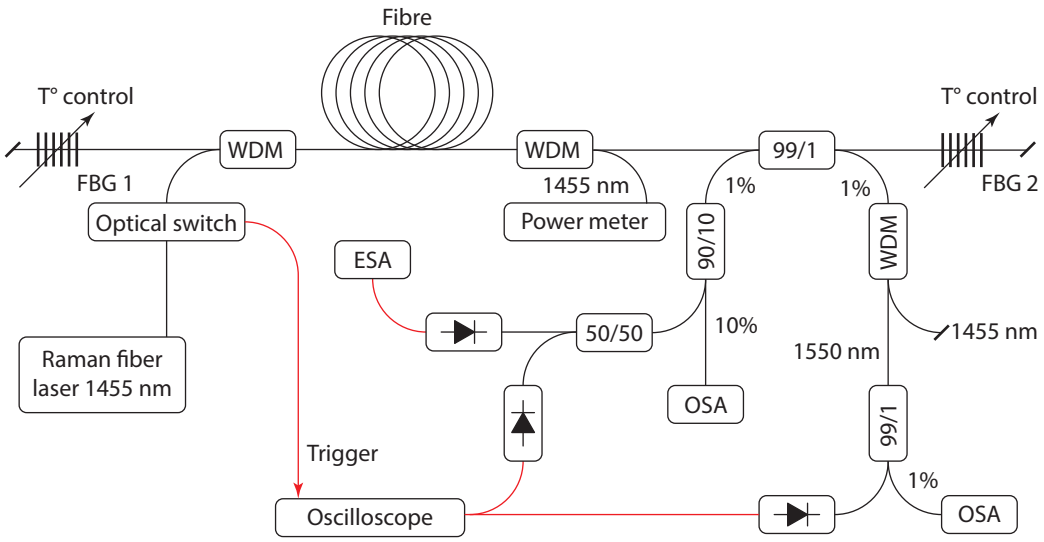

Figure 3.1: The complete setup. In some experiments only part of the measurement equipment was used. This picture will be referenced for simplicity, with comments on the actual arrangement used.

on the optical components and measurement equipment, with a power meter monitoring the levels of the unabsorbed pump. This could be used as an indirect measure of cavity quality in the experiments, where the spectral position of the gratings was changed. The output radiation was monitored not after the output FBG, but from a 1% ports of 2×2 99/1 coupler placed after the second WDM, but before the output FBG. In this configuration the radiation coming from the cavity, after propagating in the fibre and radiation reflected by the output FBG back into the cavity can be monitored simultaneously. The FBGs were temperature controlled by Peltier elements to prevent them from detuning at higher optical power or environmental temperature variations, and to allow some control over their relative spectral position.

As a pump source an IPG Raman fibre laser with a maximum output power of 5 W at 1455 nm was used, with a 1 nm linewidth. By the design, the IPG pump laser only allows slow gradual increase in the output power, so in some experiments it was connected to the input WDM through the optical switch, which allowed to quickly, with the rise time around 200 ns, increase the pump power coupled into the cavity to the operational level. Controlling the switch with a signal generator and synchronising the oscilloscope trigger

could allow, for example, to gather "switch-on" statistics to study transition dynamics of the radiation build-up stage, or look closely into the processes of pulse formation and interaction.

The intensity dynamics from the 99/1 coupler were registered by a 50 GHz DC coupled photodetector and 33 GHz real-time digital sampling oscilloscope with 2 GSa memory depth. Using two input channels of the oscilloscope makes possible to align two temporal or spatio-temporal pictures, for example before and after the reflection from the output grating, to study the effects of spectral filtering and dispersion compensation, and add another control point for comparison with the numerical simulations. No processing was performed directly on the oscilloscope. Complete 2 GSa traces were stored during the experiment, with most of the processing done in MatLab offline, due to the high computational intensity. The radio-frequency power spectrum was also recorded in some experiments with the same 50 GHz photodetector and 13.6 GHz electrical spectrum analyser, or used to find the optimal position of the FBGs detuning in real time during the experiment. The optical spectrum was recorded by a gratings based Yokogawa AQ6370C optical spectrum analyser.

Table 3.1: Parameters of the fibres used in the experiments

Fibre Parameter	OFS IDF	OFS Raman Fibre
Length (m)	988	2200
Refractive index n @1550	1.472	
Dispersion @1550 nm (ps/nm/km)	−44	−20
Dispersion slope @1550 nm (ps/nm^2/km)	−0.14	0.031
Mode field diameter (μm)	6.4	4.9
A_{eff} (μm^2)	31	18.7
Raman gain (W·km)$^{-1}$	1.5	2.5
Attenuation @1550 nm (dB/km)	0.234	0.33
Attenuation @1450 nm (dB/km)		0.43
n_2 (10^{-20} m^2/W)	2.36	
Nonlinear coefficient γ @1550 nm (W·km)$^{-1}$	3.08	5.85
Nonlinear coefficient γ @1450 nm (W·km)$^{-1}$	3.77	7.24
Polarisation mode dispersion (ps/$\sqrt{}$km)	< 0.04	0.05

Parameters of the fibres used in the experiments are combined in the Table 3.1, available from the manufacturer. Only two different spools were used – 988 m of OFS IDF and 2200 m of OFS Raman fibre, both with high normal dispersion. The total dispersion

for both spools was almost the same β_2 = 56 ps^2/km, which allowed to compare the laser dynamics for the same total cavity dispersion, but different nonlinearity and Raman gain coefficients.

The whole setup was assembled using connectors, which allowed to quickly rearrange the configuration, or exchange different components, but increased the total loss of the cavity. Although usually undesirable, increased cavity losses could play a stabilising role in some observed regimes, as was confirmed by numerical simulations.

3.2 Impact of Gratings on Spatio-temporal Regime

To investigate the origin of the partial mode-locked and intermittent pulse regime in the previous setup, the effects of FBG's shape and spectral detuning were examined in more detail. The results are described in this section.

3.2.1 Super-Gaussian Zero Dispersion Gratings

The setup was largely unchanged, except for measuring equipment. The gratings used (Figure 2.2) were quite wide at 1.1 nm, or 137 GHz, and had high reflectivity of 93%. The group delay was designed to be as flat as possible over the grating profile to minimize the chirp. The cavity was formed of 1 km of OFS IDF fibre (see table 3.1). The lasing regime of interest started at 2 W and extended to over 3.5 W of pump power at 1450 nm, with transition to turbulent regimes at higher pump powers. With no direct method to confirm the spectral position of the gratings, their alignment was optimised by monitoring the intracavity power. The higher the power the better the alignment. In this setup the 50 GHz DC coupled photodetector was used with the 33 GHz digital sampling oscilloscope to resolve the structure of the pulses observed in the partial mode-locked regime described previously.

The temporal dynamics in this case were monitored simultaneously from the cavity, and reflected from the output grating (see Figure 3.1), and are shown of Figure 3.2a. The laser produced a train of noise-like pulses with the duration of an order of a nanosecond. This lasing regime can also be viewed as a stochastic radiation modulated with a sinusoidal amplitude envelope. The signal from both channels is very similar, which indicates that

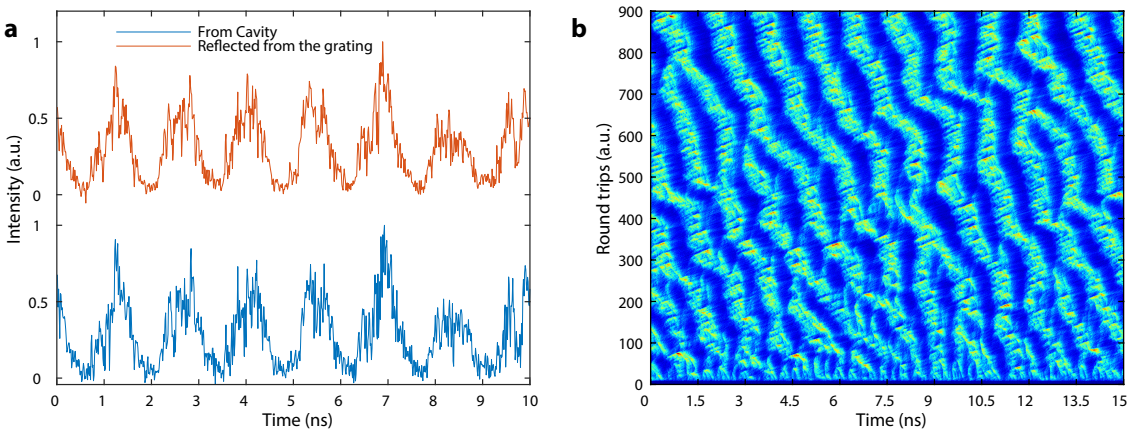

Figure 3.2: a, Simultaneous temporal dynamics for the radiation registered coming from the cavity (please refer to the Figure 3.1) and reflected from the output grating, and **b,** spatio-temporal dynamics of the laser registered in the switch-on regime, showing radiation build-up at the initial stages of laser operation.

the broadening was not strong and gratings filter a very small part of the radiation. The laser was also operated in "switch-on" regime, with the pump power switching quickly to the required power levels. This allowed to look into initial stages of pattern formation. The spatio-temporal dynamics in switch-on regime reveal the processes in the initial stages of radiation build-up Figure 3.2b. After 5–10 round-trips the power at Stokes wavelengths builds-up and lasing starts with highly stochastic output. The smaller bright and dark structures start to cluster effectively reducing the modulation frequency. After approximately 1000 round-trips the repetition rate stabilises, with no further collisions or splitting of the noise-like pulses.

The spatio-temporal dynamics in the stable regime, long after the power switch and measured after reflection from the output grating are shown on Figure 3.3. The round-trip time was chosen so the reference frame moves slower, to improve the visibility of the dark solitons which form the trough between the noise-like pulses. These solitons move considerably slower than the bright structures, when they move between pulses and change their speed when they run across the bright structures. Some of the solitons accelerate quickly to the speed of the pulses and slowly decay, while other travel across without much change. This difference can probably be attributed to the different polarisation of the dark solitons, i.e. some dark solitons are scalar and some are vector type [179, 180]. To investigate the nature of these solitons further experimental investigation is required, with careful control

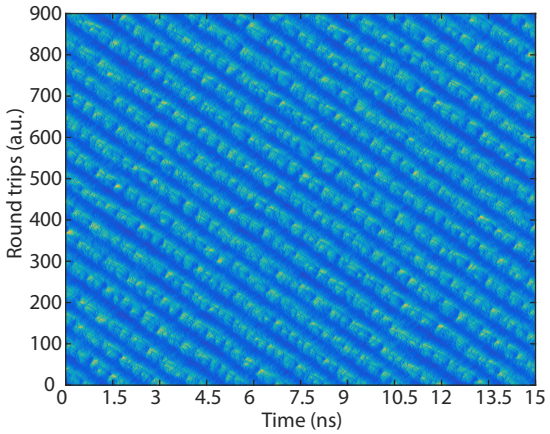

Figure 3.3: Round-trip picture for super-Gaussian gratings in stable regime.

of the polarisation evolution of radiation within the cavity and polarisation resolved measurements. It is hard to estimate the lifetime of the dark solitons from the spatio-temporal pictures due to low contrast between pulses and multiple collisions. The lifetime measurements could help to determine the type of the dark solitons.

The intensity auto-correlation function for this generation regime was calculated from the time traces. On the Figure 3.4a a small peak is visible at zero delay, which indicates the presence of short substructures in the radiation – dark solitons. The modulation period of 1.4 ns can be clearly seen which corresponds to the repetition rate of the noise-like pulses. It is not clear by what system parameters this repetition rate is defined, but could be related to the pump and Stokes wave interaction, such as pump and Stokes waves walk-off distance over the cavity propagation length. The Figure 3.4b shows additional modulation with the period of approximately 7 ns. Incidentally third peak of this modulation and the 15th period of pulse repetition rate corresponds to the 21.4 ns acoustic echo, which might suggest that the electrostrictive interaction mediated through acoustic waves can stabilise the repetition rate [181], although the peak powers in the cavity are relatively low to induce a strong acoustic wave. The background level is reduced slightly after reflection from the output grating, due to filtering of the spectral wings.

The optical spectrum measured from the cavity has close to parabolic shape in the central part and exponential spectral wings Figure 3.5a, with the FWHM of 0.5 nm at 3.5 W of pump power. The spectral shape in the central part is defined by the spectrum of the pulses propagating in normal dispersion and evolving towards asymptotic parabolic shape,

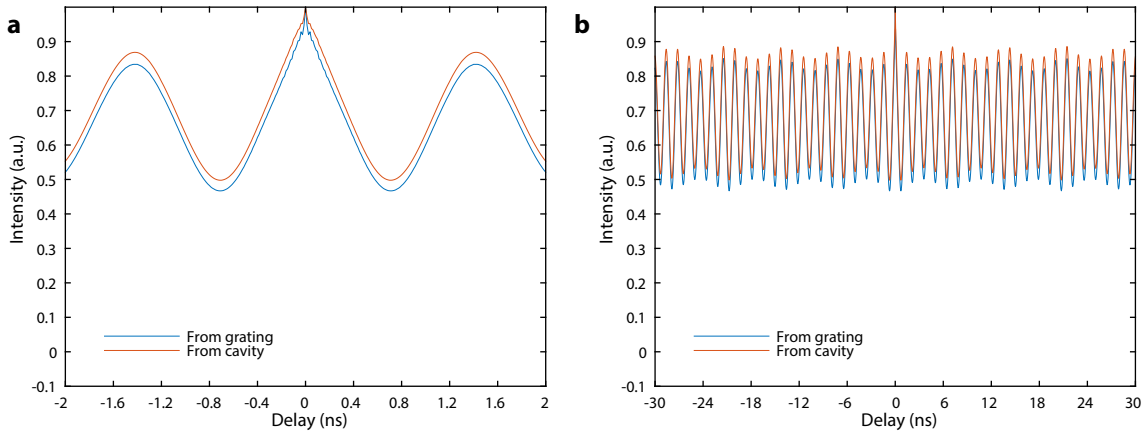

Figure 3.4: Intensity auto-correlation functions calculated from the temporal dynamics at different time scales for the case of second order super Gaussian fibre Bragg gratings centred at the same wavelength.

with linear upchirp, while energy in the background radiation through four-wave mixing (FWM) is transferred into the spectral wings. The RF power spectrum (Figure 3.5b) shows some interesting features. A relatively narrow line corresponding to the repetition rate of 700 MHz and consisting of tens of cavity modes has a contrast of 40 dB. The noise envelope increases from zero frequencies, reaches the plateau extending from around 500 MHz to 2 GHz and quickly decreases reaching the minimum at 10 GHz. From the shape of this envelope we can estimate that the average duration of a random fluctuation within the pulse envelope is 100–130 ps [182]. The amplitude of harmonics of the repetition rate decrease quickly, disappearing after 9th, with odd harmonics having higher amplitude than even harmonics, indicating that the spectral modes decorrelate quickly from central part towards the wings. Considering the relatively good 40 dB contrast for this partial harmonic mode-lock it is reasonable to assume that with the help of some additional mode-locking mechanism it would be possible to achieve pulsed regime in this configuration.

3.2.2 Uniform Fibre Bragg Gratings

To further investigate the impact of the FBGs shape, width and dispersion on the generation dynamics of all normal dispersion RFL, two simple uniform gratings, which reflectivity and group delay profiles are shown on the Figure 3.6 were used as the cavity mirrors, while the rest of the setup was kept the same. The gratings had high reflectivity of 92% and 98%

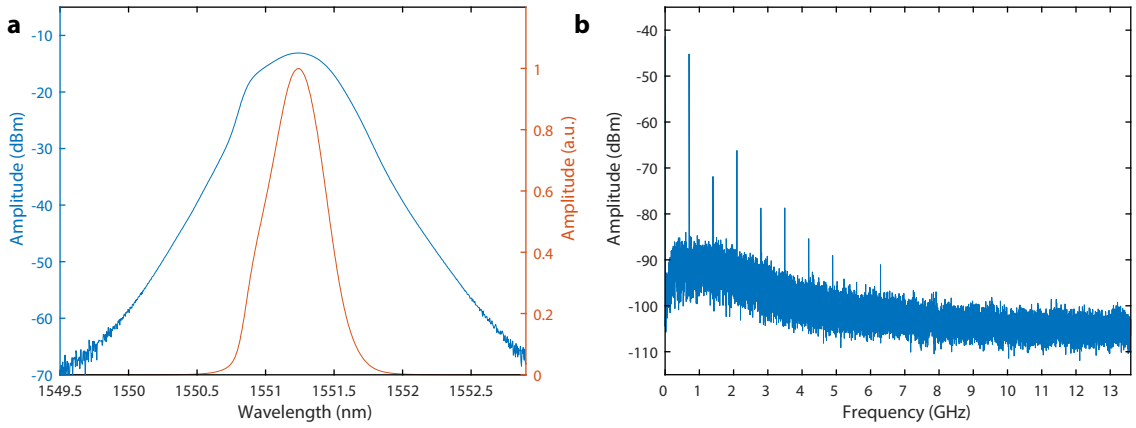

Figure 3.5: a, Optical spectrum in linear and logarithmic scale and **b,** RF power spectrum of the output radiation.

with FWHM approximately 0.09 nm, or 11 GHz. The group delay profile is standard for uniform gratings and has a parabolic shape, which translates into group delay dispersion of 60 ps^2/nm. The reflection spectrum exhibits strong side lobes, with reflectivity as high as 20%, due to the simple unapodised design, which means that the strength of the refractive index modulation drops abruptly outside of the grating length. The spectral position of the gratings, as in previous experiment was adjusted by monitoring the level of unabsorbed pump radiation at the end of the cavity. In this setup the total cavity dispersion is normal, and so no MI should take place, and we should not expect any pulse formation in this simple configuration.

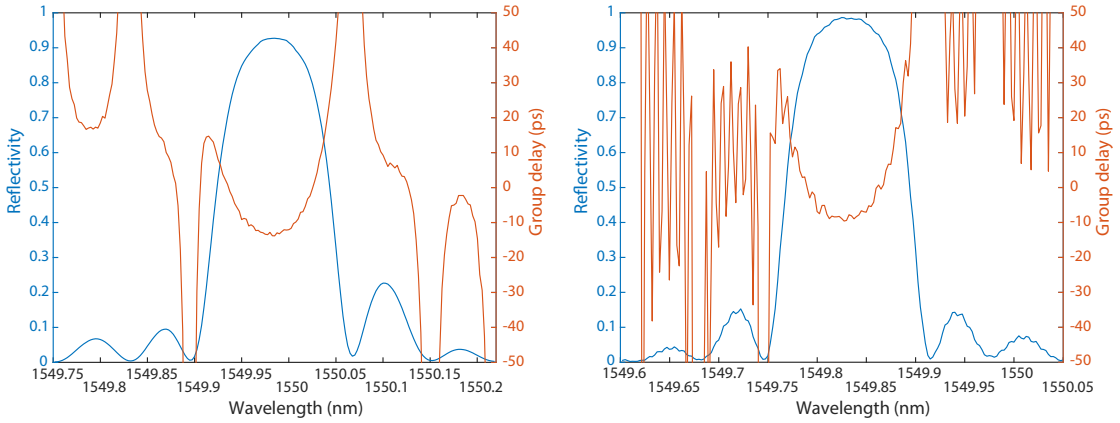

Figure 3.6: The reflection spectrum and group delay of regular fibre Bragg gratings used in the experiment. The spectral position of the gratings was controlled by the Peltier temperature controller and was adjusted during the experiment to ensure that the central wavelength of the gratings coincide.

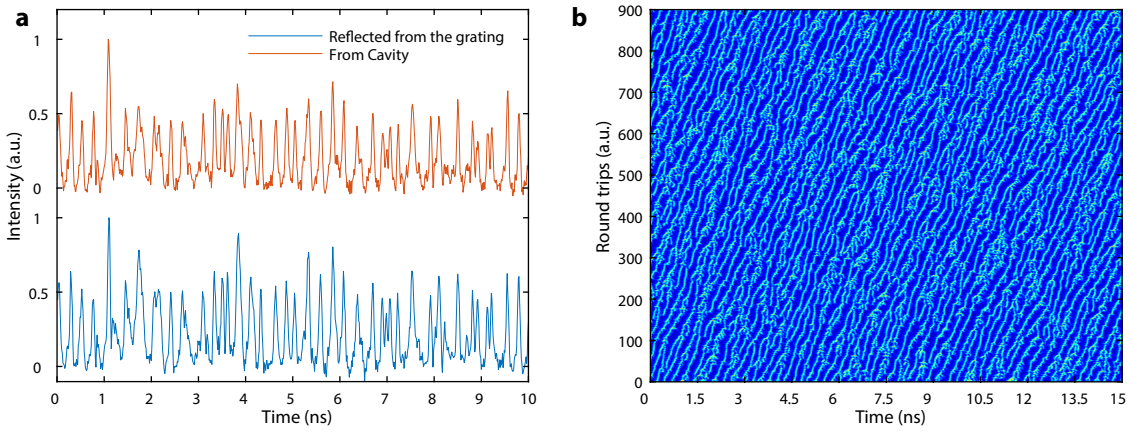

Figure 3.7: a, Simultaneous temporal dynamics for the radiation registered coming from the cavity (please refer to the Figure 3.1) and reflected from the output grating, and **b,** spatio-temporal dynamics of the laser radiation.

From Figure 3.7a we can see that starting from 1.5 W of pump power the laser generates a pulse train with unstable amplitude, pulse duration and repetition rate. Again, like in the case with wider gratings, the radiation coming from the cavity and reflected from the output grating looks very similar, which indicates that there is no significant spectral broadening at this pump power level, and the spectrum of the pulses is well within the profile of the gratings. Looking at the output dynamics in spatio-temporal representation Figure 3.7b we can see that pulses appear and survive in the cavity for tens of round-trips before merging or colliding with each other, or disappearing altogether. The level of interaction is very high, as it is clearly seen from how pulses change their group velocity, which is evidenced from different angle at which pulse propagate in spatio-temporal representation. The events of pulse bifurcation and subsequent merging, sometimes only after few roundtrips, are very common. The picture does not change qualitatively at higher pump powers and look almost exactly the same for the radiation coming from cavity and reflected from the grating.

The pulse power was not high enough to perform intensity auto-correlation measurements using second harmonic generation (SHG) auto-correlator, and so intensity auto-correlation of the time trace was calculated from the data obtained with a 50 GHz photodetector and a 33 GHz real time oscilloscope. The bandwidth of the oscilloscope allowed to resolve structures as short as 30 ps. On Figure 3.8a the central peak of the auto-correlaction function is shown, from which we can estimate that the average pulse duration is approxi-

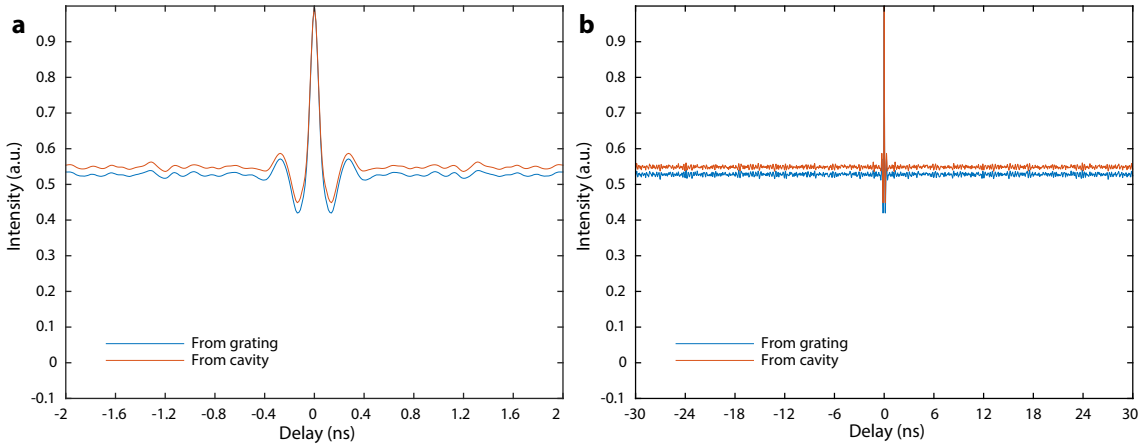

Figure 3.8: Intensity auto-correlation functions calculated from the temporal dynamics at different time scales for the case of standard narrow fibre Bragg gratings centred at the same wavelength.

mately 60–90 ps, however it is impossible to resolve the pulse structure at such short duration. The second peak indicates that the average pulse separation time is around 300 ps, but the low amplitude and lack of other autocorrelation peaks suggests very high timing jitter, which indeed is clear from the spatio-temporal dynamics Figure 3.7b. The background level of the auto-correlation before and after the reflection from the grating is almost unchanged and close to 0.5. The Figure 3.8b illustrates that there is no peak at 21.4 ns, which means there is no measurable electro-acoustic interaction between pulses [149, 151], or that it is suppressed by strong background radiation.

The optical spectrum of the output radiation in linear and logarithmic scales is shown on the Figure 3.9a. The spectral width is 0.09 nm, which corresponds to the width of the gratings. The spectrum does not exhibit the same features as in the case with broader super-Gaussian gratings, in particular the central part does not approach the parabolic shape, but rather slightly asymmetric, tilted towards longer wavelengths hyperbolic secant. The width of the spectrum of the radiation coming from the cavity and reflected back from the output gratings is almost the same, indicating that there is not much spectral broadening after propagating in the cavity.

The radio-frequency spectrum is shown on the Figure 3.9b. A small wide peak at 3.5 GHz, corresponding to the pulse repetition rate is visible on the noise background. The nature of this frequency, as in the case of wider super-Gaussian gratings is not clear, but the mech-

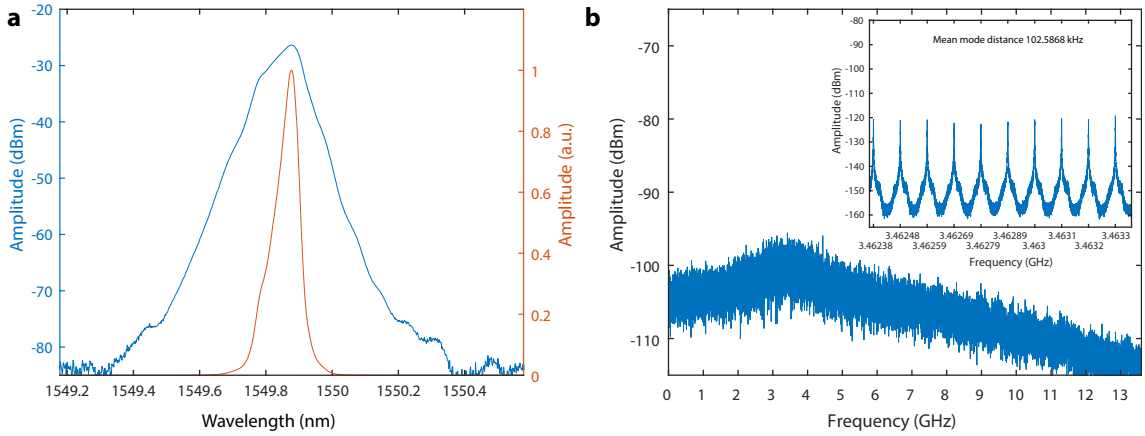

Figure 3.9: a, Optical spectrum in linear and logarithmic scale for 1.5 W of pump power and **b,** RF power spectrum of the output radiation with the longitudinal cavity modes resolved on the inset.

anism seems to be completely different from what was observed in the previous configuration. Low signal to noise ratio and large width of the peak indicate very large jitter and background noise, which is consistent with measurements from the ACF. The cavity modes resolved at the peak position are shown on the inset of the Figure 3.9b. From the power spectrum of the noise pulse train we can see that the frequency width of the noise bands is almost half of the intermodal distance [182]. It is worth noting, however, that the bandwidth of the electrical spectrum analyser was much lower than the average bandwidth of the pulse, which contributed to the peak broadening in the power spectrum.

In conclusion, these simple uniform narrow gratings change the temporal and spatio-temporal regime of generation of the laser drastically. Considering the high normal dispersion of the fibre, which makes formation of solitons impossible, and simplicity of the setup, the nature of these low quality pulses, surviving in the cavity for many roundtrips without broadening and dissipation, is not clear, and requires further investigation. However, the regime shows some promise in terms of mode-locking potential.

3.2.3 Dispersion Compenstating Super-Gaussian Gratings

The last set of gratings that was tested in the configuration described above is an identical pair of specially made super-Gaussian gratings of 3rd order (Figure 3.10). The gratings have FWHM of 0.98 nm, high reflectivity of 97% and linear chirp 41 ps/nm or -53 ps^2. The

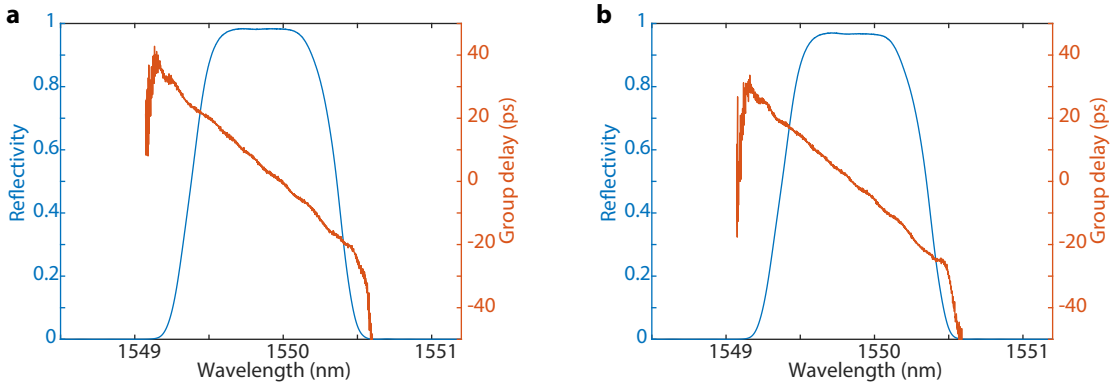

Figure 3.10: The reflection spectrum and group delay of regular fibre Bragg gratings used in the experiment. The spectral position of the gratings was controlled by the Peltier temperature controller and was adjusted during the experiment to ensure that the central wavelength of the gratings coincide.

gratings were oriented to partially compensate the normal dispersion $\beta_2 = 56$ ps^2 accumulated during the propagation in the fibre, leaving the total cavity dispersion slightly normal. While this makes the system linearly stable with respect to MI, high cavity length, and correspondingly large number of longitudinal modes together with the relatively high pump powers would likely cause the system to operate in a stochastic, turbulent regime. Periodic modulation of dispersion could also impact the stability of the system [183].

The spectral shape of the gratings and compensation of the accumulated dispersion change the temporal dynamics of the laser radiation significantly (Figure 3.11a). Contrary with what was observed in the case of other sets of gratings, there are no noise-like or short pulses in this case. The time trace looks stochastic on all time scales. Looking at the trace after the reflection by the grating, we can see that the chirped gratings compress random structures from an average 300 ps down to 100 ps. The optical spectrum has FWHM of 1 nm which equals to the width of the gratings, while exhibiting rather unexpected and unusual spectral shape. The central part of the spectrum is well approximated by Gaussian shape $\exp\left(\frac{(\lambda-1549.84)^2}{0.08}\right)$, while the spectral wings are better approximated with a bit shifted and much wider function $\exp\left(\frac{(\lambda-1549.98)^2}{0.3}\right)$ which is 10 dB lower in amplitude.

Although in previous experiments spatio-temporal dynamics helped to reveal interesting hidden dynamics, it is not the case in this instance. Bright structures present in the radiation tend to merge together before dissipating into the background, the process that in spatio-temporal domain (Figure 3.12) is represented by triangular shaped puffs, that live

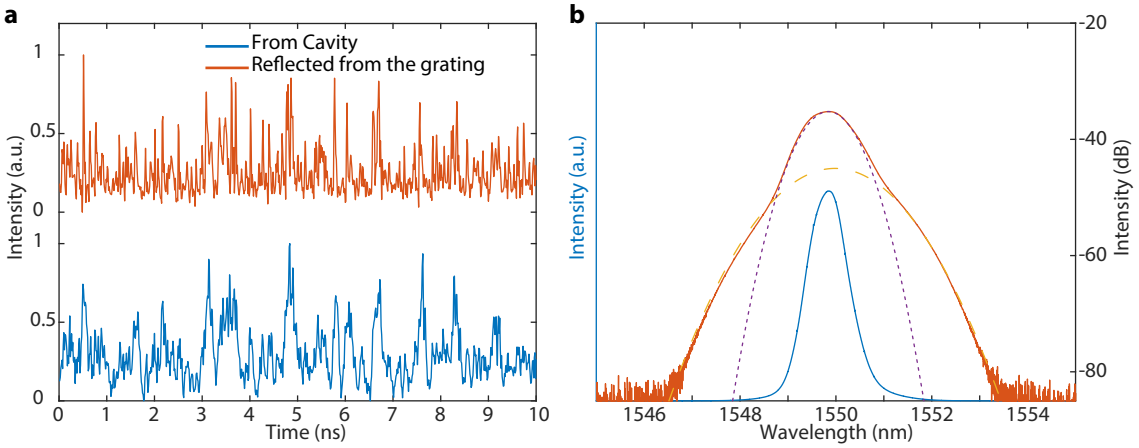

Figure 3.11: a, Simultaneous temporal dynamics for the radiation registered coming from the cavity (please refer to the Figure 3.1) and reflected from the output grating, and **b,** optical spectrum in linear and logarithmic scale for 1.5 W of pump power.

in the cavity for 5–10 round-trips. The compression of these structures by the gratings is even more evident when radiation from the cavity (Figure 3.12a) is compared to the radiation reflected from the grating (Figure 3.12b). The process of merging of bright structures is also more apparent on this picture. Very short, on the limit of resolution of the oscilloscope, pulses tend to quickly cluster into broader brighter structure, which quickly narrows and dissipate. This process, although very similar in the shape of bright puffs, is very different from turbulent regime observed in laminar-turbulent transition in mechanism of formation of bright triangular structures. In addition, dark and grey solitons are not observed in this regime.

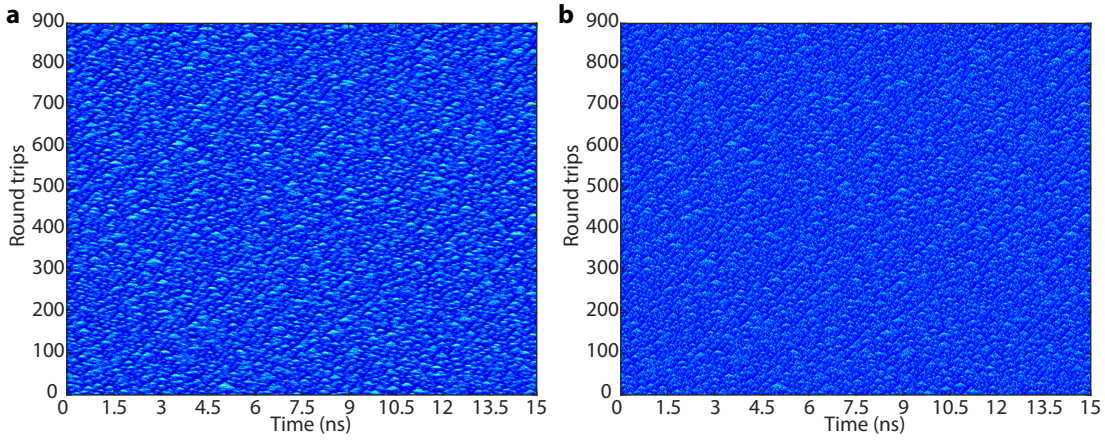

Figure 3.12: a, Simultaneous spatio-temporal dynamics for the radiation registered coming from the cavity (please refer to the Figure 3.1) and **b,** reflected from the output grating.

In conclusion, wide super-Gaussian gratings with linear chirp which almost compen-

sate the normal dispersion of the fibre, lead to stochastic operation of the laser both in temporal and spatio-temporal domains. There is no well defined modulation frequency visible in RF spectrum or ACF, which is different from previous regimes, however dispersion modulation in fibre ring cavities has been shown to lead to pattern formation in theory [184], so it is possible that such patterns could be excited under certain conditions.

3.3 Spatio-temporal Dynamics of Mode-locked Regime

The regimes described in the previous section showed some promise in terms of mode-locking. However, to develop weak mode correlations present in the systems into well defined pulses some pulse reshaping mechanism is required.

Mamyshev's optical regenerator is a pulse regeneration technique, which relies on the SPM-induced spectral broadening of the degraded signal followed by subsequent offset spectral filtering [185]. As a mode-locking technique MR was proposed by Pitois *et al.* [101]. In their theoretical work they proposed a ring cavity fibre laser with dual stage Mamyshev's optical regenerator and Ytterbium doped fibre as an amplifying media. In a linear cavity MR can be easily implemented by simple detuning of the gratings, which makes this mode-locking technique a simple and elegant solution for the setup configuration described in the previous section.

3.3.1 Super-Gaussian Gratings

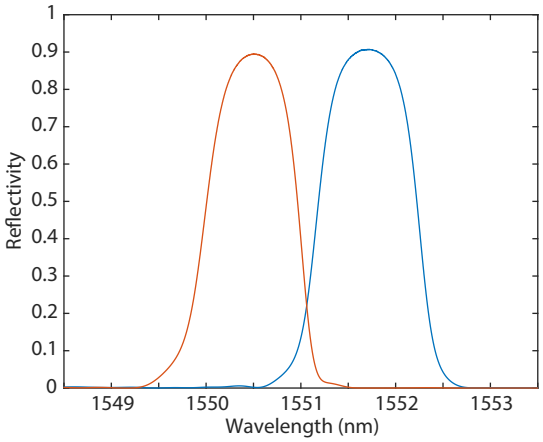

Figure 3.13: The spectra of two super-Gaussian gratings spectrally shifted by Peltier elements.

To implement MR in experiment, super-Gaussian gratings Figure 2.2 were detuned by 1.2 nm by Peltier temperature controller. As a result the lasing threshold is significantly increased due to decreased cavity quality, but the laser readily mode-locks as soon as the pump power is above threshold 3.5 W, which is expected for mode-locking by MR, as the transfer function in this case is Hevyside function with a clear threshold [101]. The repetition rate is not clearly defined by the parameters of the regenerator, i.e. shift of the gratings, but rather by all other parameters of the system, such as Raman gain, dispersion, cavity length etc. This is evidenced by the fact that the pulse repetition rate is almost the same for the case of shifted and unshifted gratings. This means that the relative positions of the pulses in the cavity can be random or defined by the other mechanisms of pulse creation and interaction, like it was mentioned in the section describing the configuration with unshifted gratings by the pump and Stokes waves interaction, while MR provides the saturable absorption mechanism required for the pulse reshaping.

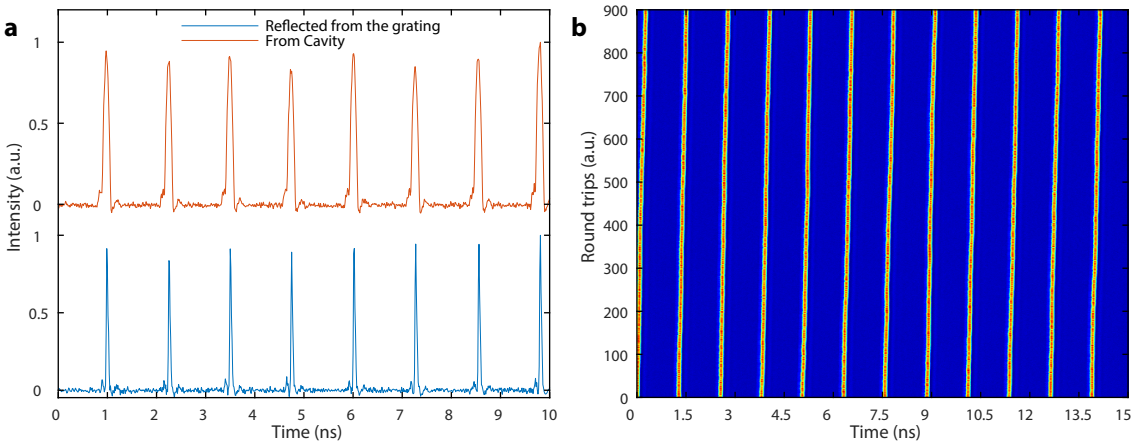

Figure 3.14: a, Simultaneous temporal dynamics for the radiation registered coming from the cavity (please refer to the Figure 3.1) and reflected from the output grating, and **b,** spatio-temporal dynamics of the laser radiation for the case of spectrally shifted second order super Gaussian profile gratings with zero chirp.

The trains of pulses from the cavity, and reflected from the grating back to the cavity are shown on the Figure 3.14a. The laser operated in a harmonic mode-locking regime with more than 7500 pulses circulating in the resonator. The pulses coming from the cavity had linear up-chirp after propagating 1 km in the fibre with normal dispersion, which was confirmed by temporal compression after propagating pulses through a external 5 km long span of anomalous dispersion ($D = 16\frac{\text{ps}}{\text{nm}\cdot\text{km}}$) fibre. The pulses reflected from the output

grating had shorter duration, as expected for spectrally filtered pulses with linear chirp, which is the manifestation of pulse reshaping mechanism provided by strongly detuned FBGs. It is also clear from this figure (the pulses are synchronised) that the pulse amplitude variation is visibly reduced by the spectral filtering, which is again expected for the MR – any pulse above the threshold will be filtered to the same spectral, and correspondingly temporal shape and energy due to linear chirp of the incoming pulses.

The spatio-temporal dynamics of the mode-locked regime for the pulses coming from the cavity is shown on the Figure 3.14b. Each pulse is breathing in duration and amplitude, and slightly moving relative to the reference frame, which means that the laser have a very large jitter figure. This is the consequence and reflection of the fact that each pulse is regenerated over consecutive round-trips in the process of SPM induced spectral broadening, amplification and filtering.

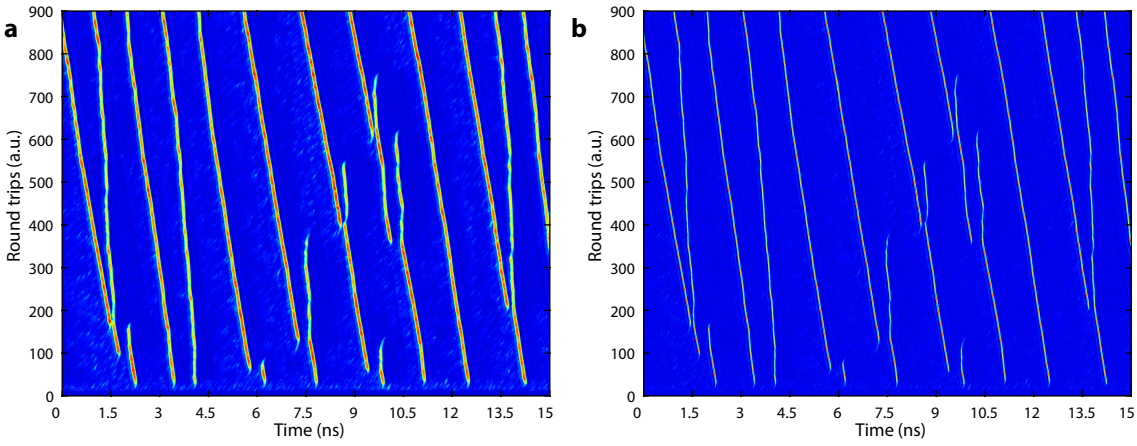

Figure 3.15: Spatio-temporal dynamics registered in the switch-on regime showing mode-locking initiation process and pulse repositioning for the case of shifted gratings registered from **a,** cavity and **b,** after reflection from the output grating.

To look into the pulse formation and rearrangement mechanisms the initial stages of radiation build-up in the laser cavity were studied in the spatio-temporal domain. The pump power was switched over time much shorter than the cavity round-trip time to the operating power by the optical switch. The radiation from the cavity and reflected from the output grating was registered simultaneously to capture the effect of strong spectral filtering, with spatio-temporal dynamics for both cases shown on Figure 3.15. At 3.5 W of pump power it takes around 10–15 round-trips for radiation to build-up after the pump

power is switched on. After that from stochastic noisy background developing at random time spacing pulses develop in 5–10 round-trips with power and duration growing quickly, which is clearly seen for the case of radiation registered from the cavity (Figure 3.15a). The speed of the background noise is lower that the speed of the pulses developing, which means that the pulses forming from this background spectrally broaden into longer wavelengths. The pulses keep appearing where noise levels are high enough, usually in the region 1–1.2 ns behind the previous pulse, which could be explained by the gain depletion. If the time separation between pulses is shorter than ~1.2 ns two possible scenarios for the trailing pulse are possible. It will either quench due to low gain, or it will drift slowly back to the region of higher gain where it will fully develop, being lower in amplitude than the first pulse in the process. This self-rearranging process takes very long time, up to 20 ms, which equals to 2000 cavity round-trips for 1 km long cavity or the propagation distance of more than 4000 km. Strong spectral filtering by the output gratings not only reduces pulse duration, but also suppresses the background noise, Figure 3.15b.

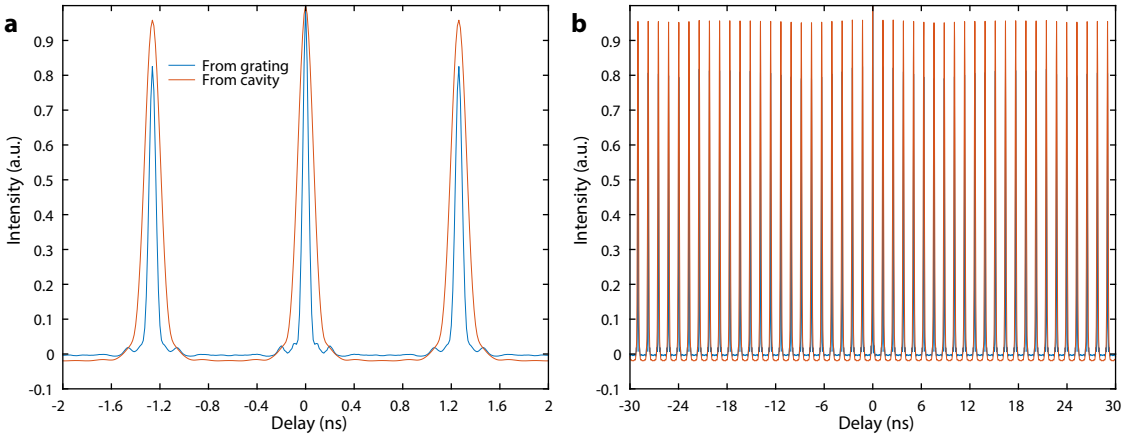

Figure 3.16: Intensity auto-correlation functions calculated from the temporal dynamics at different time scales for the case of spectrally shifted second order super Gaussian fibre Bragg gratings.

As in the case of unshifted gratings the pulse power was not high enough to perform intensity auto-correlation measurements using a SHG autocorrelator, and so intensity auto-correlation of time trace was calculated from the data obtained with the 50 GHz photodetector and the 33 GHz real time oscilloscope. The bandwidth of the oscilloscope was enough to resolve the pulse duration, and even some of the smaller features. On the Figure 3.16a

the central peak of the ACF is shown, from which we can estimate that the average pulse duration is approximately 160 ps assuming parabolic shape after propagating in the cavity, and ~80 ps after reshaping by the output grating. On the Figure 3.16b we can see the next 23 peaks of the ACF with almost unchanged amplitude, which indicates that the repetition rate and the amplitude of pulses is quite stable, however the RF spectrum would provide more information. Figure 3.16b also illustrates that the 17th peak of the ACF at 21.4 ns is only slightly higher than the neighbouring peaks, which means there is weak electro-acoustic interaction between pulses mediated by the acoustic echo from the cladding [149, 151] which is involved in pulse self-rearranging mechanism.

The optical spectra of the pulses before and after the filtering by the output grating in linear and logarithmic scale is shown on Figure 3.17a. Pulses propagating in the cavity broaden threefold from 1 nm which corresponds to the gratings width, to almost 3 nm. In agreement with conclusions made from spatio-temporal dynamics of the initial stages of operation of the laser, broadening of the pulse spectrum is stronger in the longer wavelengths. The spectrum itself is flat top shape which is typical for parabolic pulses in all normal dispersion systems, where pulses broaden more than there is gain available to support self-similar propagating without affecting the shape of the spectrum [82, 89, 178, 186, 187]. This affects the chirp, which is no longer completely linear, and as a consequence affects the compressibility and the quality of the pulse.

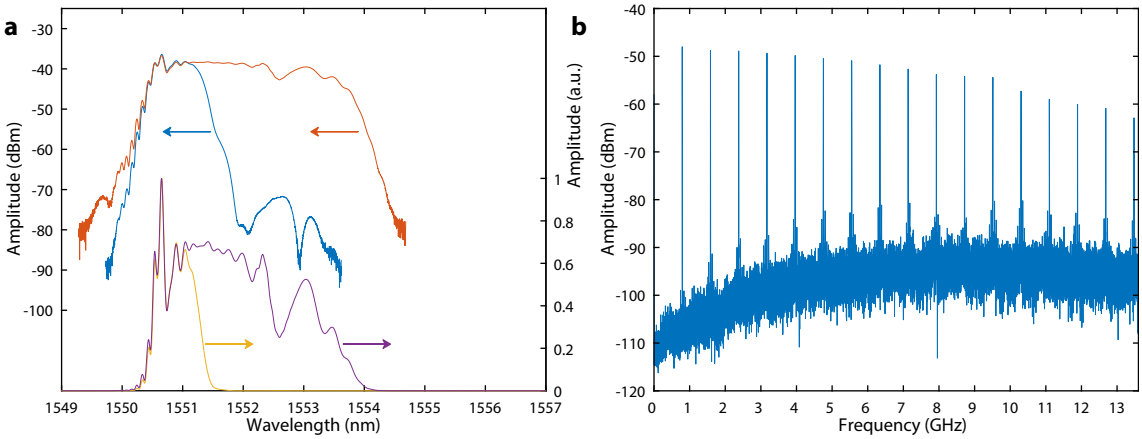

Figure 3.17: a, Optical spectrum in linear and logarithmic scale for the radiation coming from the cavity (magenta and orange) and reflected from the output grating (yellow and blue). **b,** RF power spectrum.

Although in the RF power spectrum, the laser shows relatively good, for harmonically mode-locked laser, supermode noise suppression ratio of 50 dB Figure 3.17b, in closer inspection each line in this spectrum consists of tens of cavity modes, which means the laser oscillates on different mode sets. In time domain this manifests in high timing jitter, which is consistent with the regeneration mechanism of strong spectral filtering of chirped pulses, and observations from spatio-temporal dynamics. The bandwidth of synchronised modes extends well beyond the 13.6 GHz bandwidth of the RF spectrum analyser. The noise-floor has an unusual hump-like shape, raising from low frequencies to 8–9 GHz by 15 dB and then slowly decreasing. This noise-floor shape could be explained by the pulse duration variation.

3.3.2 Parametric Instability

It has been shown [184, 188] for the systems with average normal dispersion and periodic modulation of dispersion that the modes of light which are in parametric resonance with the wavevectors of the dispersion modulation would experience growth. If the parameters of a system are modulated with the longitudinal period L, corresponding to the wavenumber $k = \frac{2\pi}{L}$, then the growing unstable mode oscillates with the wavenumber $k/2$, i.e. the double period. The pattern itself, in terms of retarded time, occurs with the frequency $\omega/2$ related to the wavenumber $k/2$, via the dispersion relation $\omega(k)$. It was predicted that these growing modes could form a pattern in the temporal domain with the period satisfying the parametric resonance condition. For a linear cavity fibre laser with chirped FBG mirrors this parametric resonance condition is automatically satisfied, as light experiences dispersion modulation twice over one round-trip. In the experiment with unshifted chirped super-Gaussian gratings, however, no pattern formation was observed, or, indeed, any periodicity in the temporal or spatio-temporal domain. The situation becomes a bit more interesting when chirped super-Gaussian gratings are detuned by 0.72 nm or 90 GHz, to introduce the MR mechanism (Figure 3.18).

On Figure 3.19a the dispersion map of the setup is presented. The dispersion is modulated twice over a round-trip, at each end of the cavity by the chirped gratings. The total

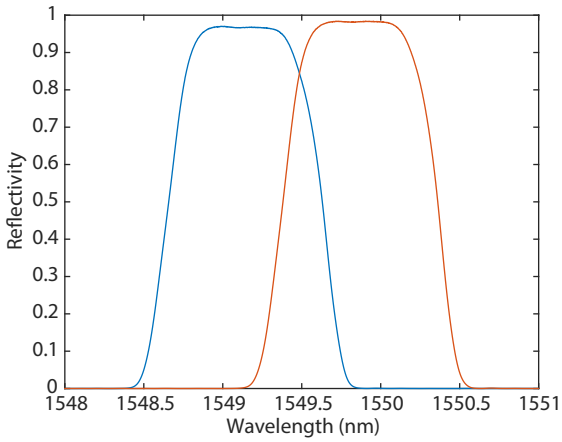

Figure 3.18: The spectra of two 41 ps/nm gratings spectrally shifted by Peltier elements.

dispersion accumulated over one round-trip is slightly normal. Unlike in the systems reported previously the growth of unstable modes is not continuous, but synchronised with the period of dispersion modulation. The pulse repetition rate, as expected for parametric instability, is the reciprocal to the length of the cavity and square root of pump power. The pattern formed is stabilised by the pulse regeneration mechanism of MR, described previously. Pulses propagating in the fibre with high gain and normal dispersion broaden self-similarly in spectral and temporal domain, acquiring linear upchirp. The filtering action of the gratings, suppresses background noise (Figure 3.19b), reshape the pulses and partially compensate the acquired chirp, regenerating the pulse.

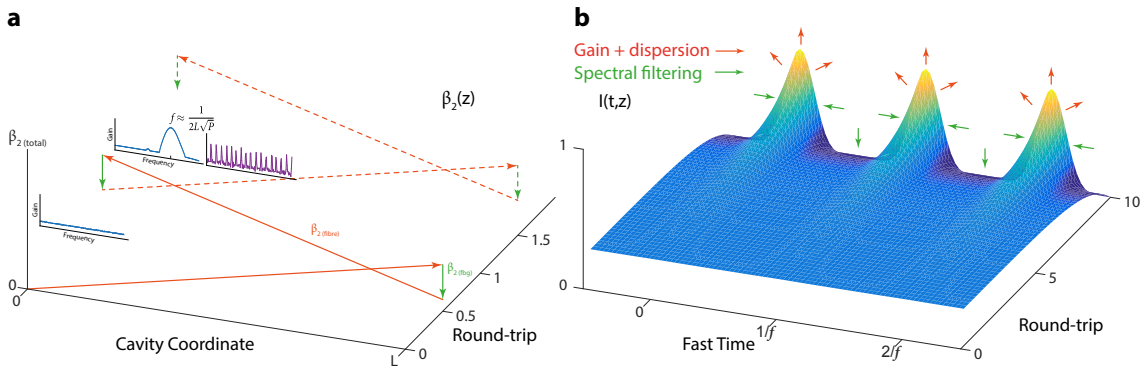

Figure 3.19: Faraday instability through parametric spatial modulation of the group velocity dispersion. **a,** The map of periodic dispersion modulation for the light propagating in a linear cavity. **b,** The parametric modulation of dispersion excites the Faraday instability in temporal domain.

The experimental data were obtained for 2.2 km long Raman fibre with high normal dispersion (see table 3.1) and two chirped FBGs which were shifted by 0.72 nm or 90 GHz

(Figure 3.18) in the range of pump powers from 0.9 to 2.5 W. The time traces registered from the cavity and after reflection from the output FBG are shown on Figure 3.20a. Despite the relatively low bandwidth of the oscilloscope it could be seen that the pulses coming from the cavity have near parabolic shape, with pulse wings overlapping. However, after filtering by the chirped grating the pulse duration is reduced and the shape is changed. Small side lobes on both sides of each pulse could be distinguished. The temporal duration and amplitude vary strongly from pulse to pulse, with some pulses having an amplitude almost twice as high as average. In the spatio-temporal domain (Figure 3.20b) we can see that despite the fact that the pulses are quite stable over evolution coordinate, they still interact with the background, shifting their position and increasing the gap to the following pulse, allowing a small structure to develop from the background in this position, which in turn affects the positions of the following pulses. This "ripple" effect back-propagates until the pulses find a stable separation distance. These interactions and shifting affect the stability of mode-locked regime, increasing the timing-jitter.

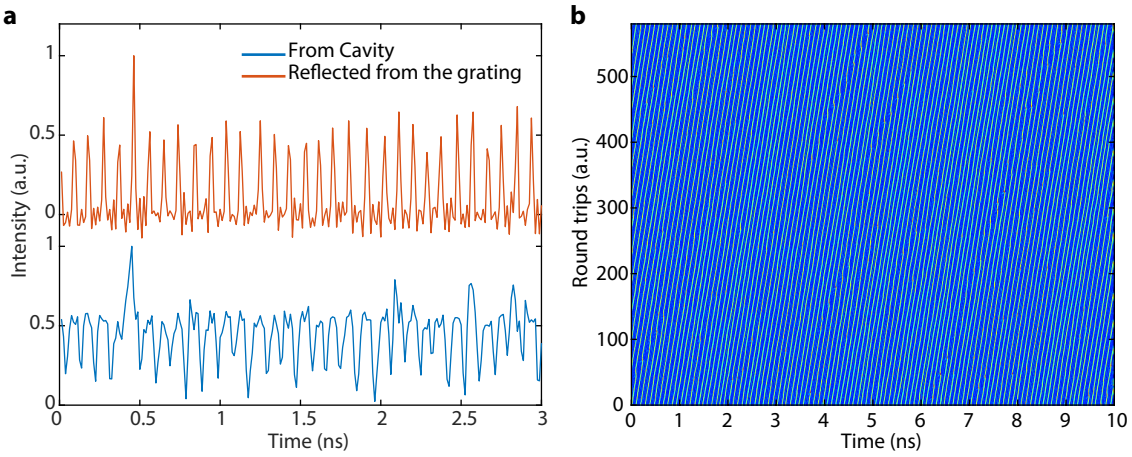

Figure 3.20: a, The temporal intensity dynamics of the output radiation and **b,** corresponding spatio-temporal representation.

The shape of the pulses reflected from the output FBG was measured by the SHG intensity auto-correlator Femtochrome 103-XL and is shown on Figure 3.21a. The pulse shape is well approximated by the Gaussian fit (red line), which is the asymptotic pulse shape for the MR [101], with the duration 7.3 ps. The ACF also features small side lobes observed on the time traces, separated by 16 ps from the main pulse. The nature of these side lobs is not clear. The intensity auto-correlation was also calculated from the time traces and is shown

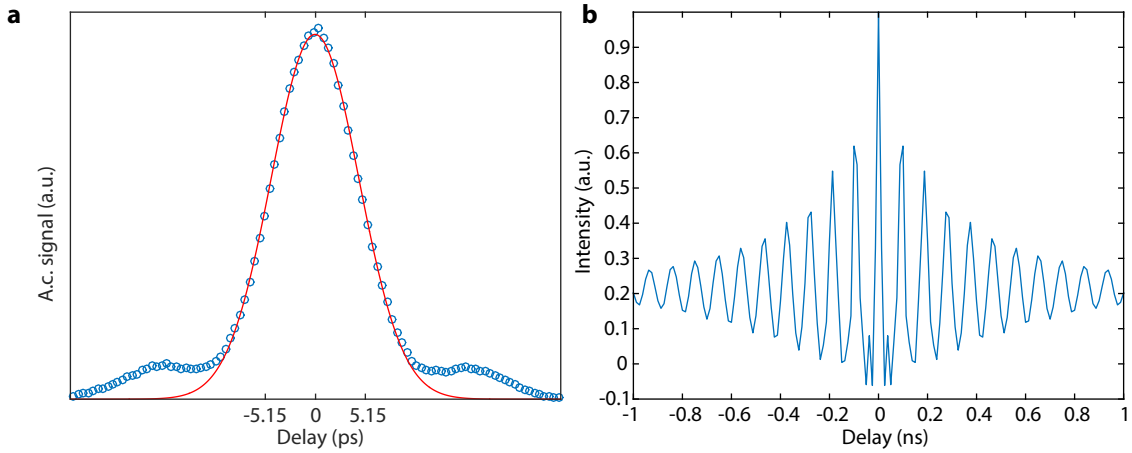

Figure 3.21: a, Pulse shape and duration measured by the intensity auto-correlator with Gaussian fit, and **b,** intensity auto-correlation calculated from the pulse train time trace.

on Figure 3.21b. The amplitude of auto-correlation peaks decays quickly which means that the correlation time is very small, indicating rather poor quality of mode-locking.

The optical spectrum of the pulses Figure 3.22a was narrower than the width of the gratings with FWHM 0.65 nm or 80 GHz, and multipeak structure, which, as we have seen, is characteristic for pulses undergoing periodic transformation between asymptotic parabolic shape of pulses travelling in normal dispersion amplifying media, or laser cavity in this case, and asymptotic Gaussian shape after the strong filtering by the FBGs, which is characteristic for MR. In the power spectrum (Figure 3.22b) the peak at the repetition rate 11 GHz could be seen, which corresponds to the ~240000 harmonics of the fundamental frequency 46.4 kHz for 2.2 km long cavity. The peak is very wide, which can be explained by timing-jitter of the pulse interaction, pulse duration associated timing-jitter due to filtering, and supermode noise. The contrast is rather poor, less than 30 dB. On the inset cavity modes are clearly resolved. Each mode has two side lobes separated by 772 Hz, and asymmetric noise bands. It is possible that parameters of the MR defined by the FBGs width and spectral separation distance are not well suited for the pulse repetition rate, and as a saturable absorption mechanism it is ineffective in suppressing background noise in this case. It should be also noted that no additional measures were introduced to improve the quality of mode-locking, but rather demonstrate that pattern formation by periodic dispersion modulation is possible in such simple experimental configuration.

Different types of instabilities follow different scaling laws with power. For example MI

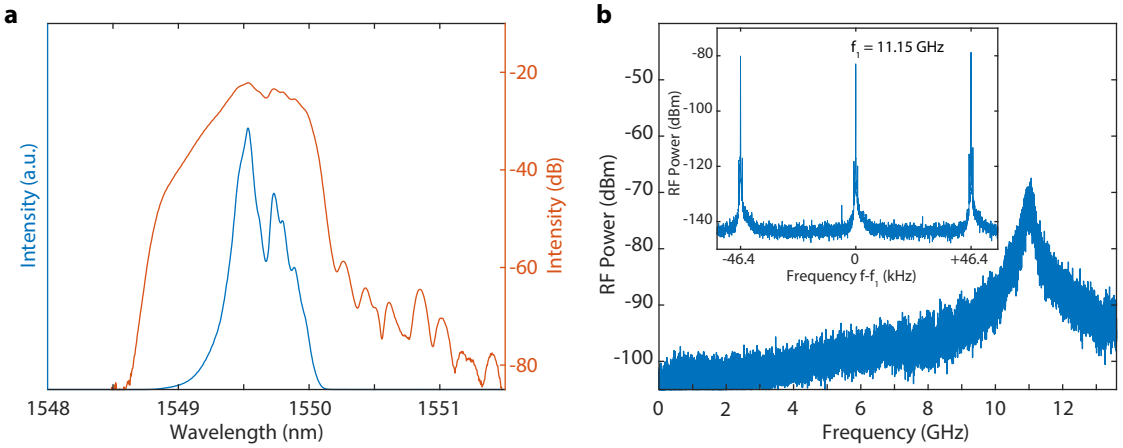

Figure 3.22: a, Optical spectrum in linear and logarithmic scale, and **b,** RF power spectrum with longitudinal cavity modes resolved on the inset (r.b.w. 1 Hz).

scales as a square root of power, both in case of total normal and anomalous dispersion with periodic modulation of dispersion [184]. To investigate the parametric instability frequency scaling, the pump power was varied in two configurations with 1 km of OFS IDF fibre and 2.2 km of Raman fibre with equal total normal dispersion (see table 3.1), which makes the total average dispersion and dispersion modulation depth the same. It is expected for this type of instability that the frequency would scale reciprocally to the square root of power, which is indeed the case Figure 3.23. For the both types of fibre used in the experiments the scaling is well approximated by $P^{-1/2}$.

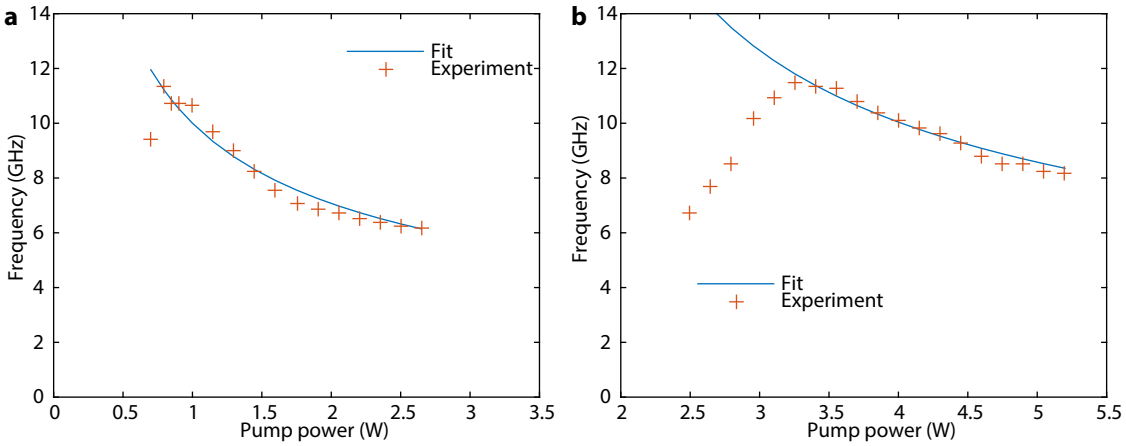

Figure 3.23: The Faraday frequency scaling with pump power for **a,** 2.2 km Raman fibre, and **b,** 1 km of IDF fibre, with 41 ps/nm dispersion spectrally shifted gratings used in both experiments.

In conclusion harmonic mode-locking in all normal dispersion Raman fibre lasers was achieved using Faraday parametric instability for pulse pattern generation and Mamyshev regenerator as a pulse reshaping mechanism. The mode-locking was easy to achieve, with-

out the need to tune the parameters of the system in different experimental realisations. In case of unchirped gratings, the harmonic mode-locking quality was relatively high, with contrast ratios up to 55 dB, although supermode noise and timing-jitter were still very high. In case of chirped gratings, the pattern formed due to parametric resonance process allowed to achieve very high repetition rates of up to 11 GHz, which corresponds to 240000th harmonic of fundamental frequency. The quality of mode-locking was rather poor, but the strength of the method is in simplicity and robustness of the setup, which shows great promise for future improvements.

The spatio-temporal treatment of the output radiation of mode-locked lasers helped to understand the processes responsible for pulse formation and pulse interaction at later stages of laser operation.

Chapter 4

Temporal Regimes of Generation of Random Distributed Feedback Raman Fibre Lasers

Despite their extremely simple design, random distributed feedback Raman fibre lasers allow some control over their generation properties, namely optical spectrum and temporal dynamics. This can be achieved by combination of cavity design and incorporation of different additional optical elements into the laser. The temporal dynamics of long Raman RDFLs are investigated is some detail. Each of the design configurations described in Section 1.3.1 have characteristic pump and Stokes wave power distribution, which allow some design freedom to incorporate control elements into the cavity, or determine the pump and Stokes waves self-organisation processes happening in the laser.

4.1 Temporal Regimes of Generation in a Regular RDFL

To study the temporal dynamics of a RDFL a simple single-arm configuration setup was used (Figure 4.1). An IPG Raman fibre laser connected through an optical switch was used as a pump source, providing up to 5 W of power at 1455 nm. The pump radiation was coupled into a 36.4 km span of anomalous dispersion OFS TrueWave fibre (D = 7.8$\frac{\text{ps}}{\text{nm}\cdot\text{km}}$) with the help of a 1455/1550 nm WDM coupler. The output radiation was monitored in

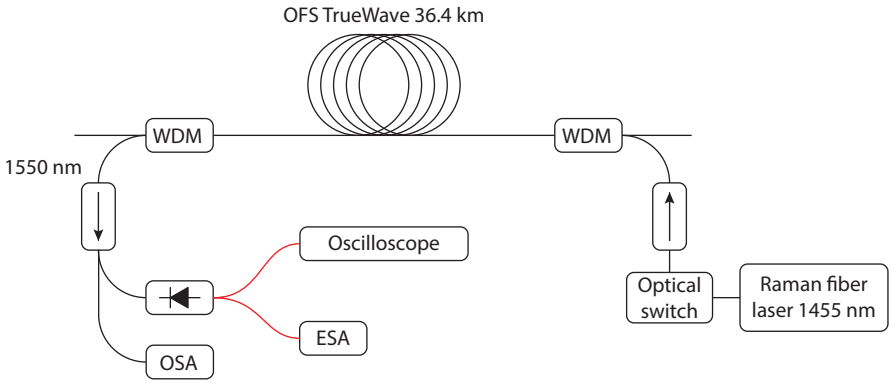

Figure 4.1: Experimental setup. Red lines indicate electrical connection.

the forward direction after filtering out the residual pump and subsequent strong attenuation. Measurements of the temporal dynamics were made using a 50 GHz DC coupled photodetector and a 6 GHz real time digital oscilloscope. Even though the bandwidth of the oscilloscope was much narrower than the optical bandwidth of the laser radiation, it is possible to make some conclusions about the statistical properties of the radiation [175], which can help to reveal extreme events and their nature.

Characterisation of the laser dynamics was performed for different pump powers in the range from 1.2 W which was the laser threshold and up to 5 W maximum available from the pump source. Despite the simplicity of the configuration there are qualitative changes in the temporal and spectral properties of radiation depending on the pump power. Time traces for three pump powers, 2.2, 2.8 and 3.8 W, representative of the different modes of operation are presented in Figure 4.2a. Three 500 ns long time traces normalised to the mean intensity are shown next to each other for easier comparison. At all pump powers the time dynamics look stochastic, without any definite features. Superficially at 3.8 W the time dynamics have higher frequency of intensity variation and more high intensity events, however this is not the case when we look at PDFs (Figure 4.2a inset) calculated for 2^{26} experimental points or 1.67 ms. At lower pump powers 2.2 and 2.8 W PDFs have Gaussian shape for intensities up to two times the mean value and exponential high intensity tail extending up to intensities 6–7 times the mean level for 2.2 W and surprisingly 9–10 times for 2.8 W. At the highest of the three pump power 3.8 W, the high intensity tail decay exponentially right from the most probably intensity. The nature of this change in the shape of PDF and the slope of

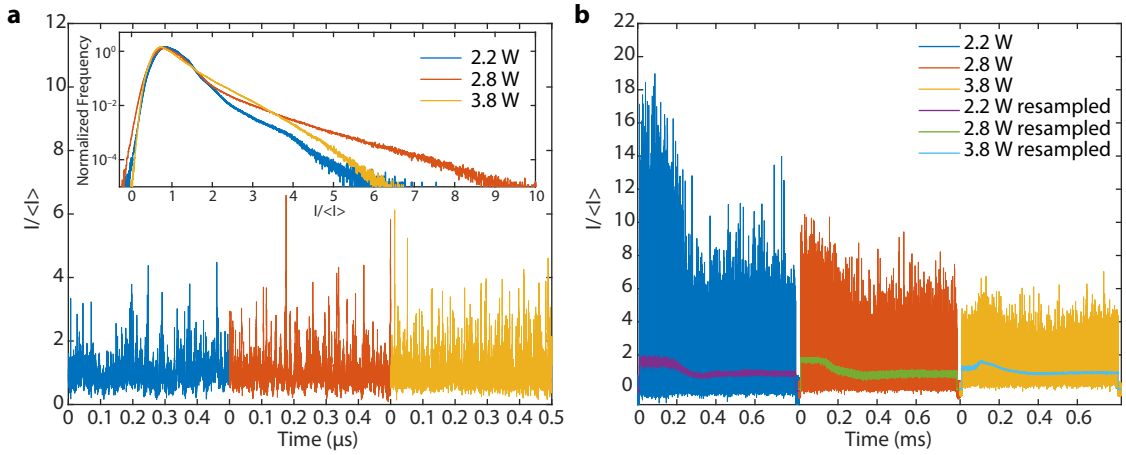

Figure 4.2: a, Time traces for different pump powers, with corresponding PDFs on the inset. **b,** Time dynamics of the radiation build-up after the pump power is switched on. Overlay traces show mean intensity.

high intensity tail is not clear from time traces, but some clues could be found in other measurements, such as optical spectrum, as it would be shown later.

The transitional switch-on temporal dynamics were also registered. Unlike conventional lasers, RDFLs don't have intrinsic periodicity in temporal dynamics associated with cavity round-trip time, and so the spatio-temporal picture of radiation build-up could not be constructed. However, some valuable information could be gained from simple time trace measurements. For all three pump powers the optical switch was used to raise pump power to the operational level for 800 μs, opening in just 200 ns, which is much shorter than the time required for the light to reach the end of the fibre. The time dynamics were measured at the other end of the fibre (Figure 4.2b) and normalised to the mean intensity. The transitional radiation build-up stage has the duration of approximately 180 μs, or the time needed for the light to pass through the fibre and the system to reach the equilibrium. The mean intensity at this stage is almost twice as high as in the steady state. It is important to consider this property when designing Raman fibre lasers for practical applications.

On ACFs Figure 4.3a we can see that the average structure duration decreases from around 1 ns at 2.2 W to 0.5 ns at 3.8 W. A clear modulation period of 3.9 ns or 257 MHz is present at 2.2 W for which we can see clear correspondence in RF spectrum (Figure 4.3b). Comparing the RF spectrum of the pump and of the RDFL, it is clear that this modulation, as well as other main features of the pump laser RF spectrum, such as cavity mode beating

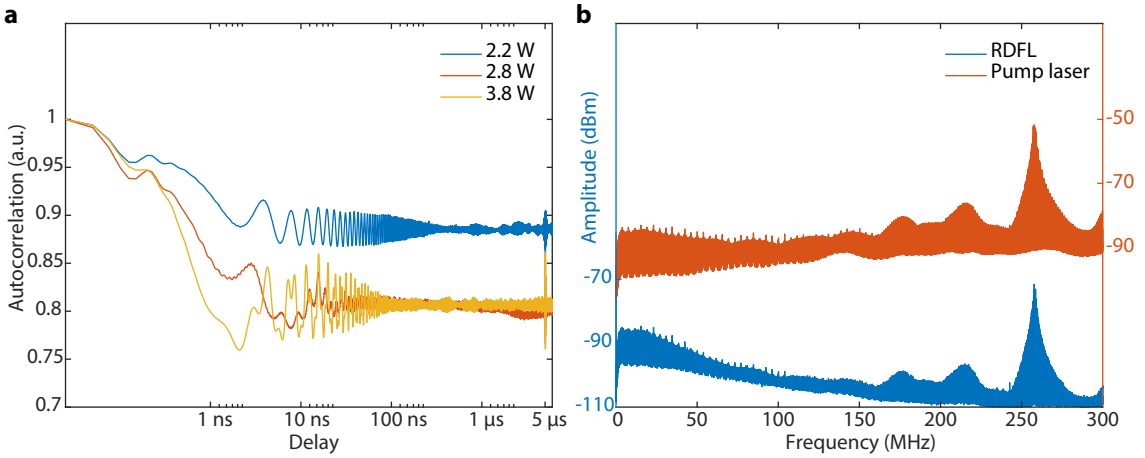

Figure 4.3: a, ACFs of the time traces at different pump powers. **b,** RF spectra of the laser output generation and the pump laser at 2.4 W.

frequency 200 kHz are also present in the RF spectrum of the RDFL. As Raman scattering is a fast process with typical times of less than a picosecond, any pump wave fluctuations could be transferred into fluctuations of the Stokes wave in the process called RIN transfer. This process is known to be a drawback in Raman amplifiers used in telecommunication as it introduces additional noise into amplified signal and was studied in forward pump configuration for different powers and fibre lengths numerically [128]. It was shown that the noise transfer decreases with increase in pump power or cavity length. In agreement with numerical simulations we can see that RIN transfer function is constant at lower frequencies up to tens of MHz, and quickly decrease for higher frequencies. While a drawback in other applications, RIN transfer process could be used as a constructive mechanism. For example by transferring cavity mode-beating or other modulation frequencies from the pump laser as a seed into the laser radiation, where they can be further developed into pulses [169].

The optical spectrum is typical for Raman RDFL, with one peak at 1550 nm at lower pump powers and two peaks corresponding to the maxima of Raman gain at 2.8 W. At higher pump power the laser switches to 1566 nm altogether. This transition between spectra can explain some of the dynamics of the laser. For example at 2.8 W PDF has longer high intensity tail which can be associated with double spectral peak structure observed.

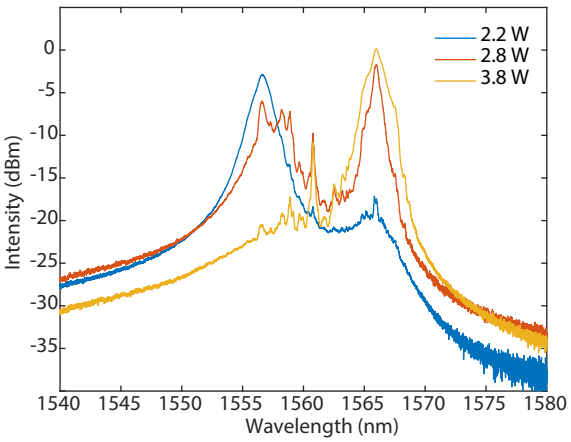

Figure 4.4: Optical spectra at different pump powers.

4.2 Temporal Regimes of Generation in Quasi-Q-Switched RDFL

Despite the growing interest in random distributed feedback fibre lasers, not many works were focused on studying the temporal dynamics of RDFLs. Largely this is due to simplicity of their design, hence the simple stochastic nature of the output radiation. However Raman RDFLs can have complex temporal dynamics, with interesting properties. In [189] authors experimentally demonstrated and studied a relatively short single-arm RDF Raman fibre laser. They observed stable oscillations at the frequency a fraction smaller than the fibre transition times. Numerical simulations of the experiment were presented. The pulsations are reported to be the result of pump and Stokes radiation in the first and second order interaction. In another work passive Q-switching operation of a single-arm double pump configuration RDFL was reported [190]. The laser produced giant pulses at 1550 nm with peak powers of up to 1 kW and average pulse duration around 1 ns from a 10 km long fibre cavity pumped by 2.4 W CW fibre laser. The mechanism responsible for pulse generation was identified as Rayleigh scattering-Stimulated Brillouin scattering cascaded mechanism.

4.2.1 Experiment and Results

To study the temporal dynamics of Raman RDFLs simple double-arm backward pumped configuration was assembled. The schematic diagram of the experimental setup is shown on

the Figure 4.5. The laser consisted of a span of fibre, two wavelength division multiplexing couplers to couple the pump power into the cavity and 4 isolators, two for the pump lasers and two for the outputs, to minimize back-reflections into the cavity, minimise pump and Stokes wave interaction, and to protect the pump lasers from damage in case of high levels of back-reflection. The pump isolators provide at least 25 dB and the output isolators provide at least 55 dB return loss. Anomalous dispersion OFS TrueWave fibre ($D = 7.8\frac{\text{ps}}{\text{nm}\cdot\text{km}}$) was used in the experiment, with the length of fibre varying in the range from 27 to 72 km. IPG Raman fibre lasers were used as pump lasers, each providing up to 5 W of optical power. All connections were made by splicing to minimize parasitic reflections, which could be high compared to the intensity of random Rayleigh scattering. High speed DC coupled 50 GHz photodetector, 6 GHz digital sampling oscilloscope, and 13.6 GHz RF spectrum analyser were used to register the output dynamics of the system. The temporal dynamics of the output radiation were monitored simultaneously from the both ends.

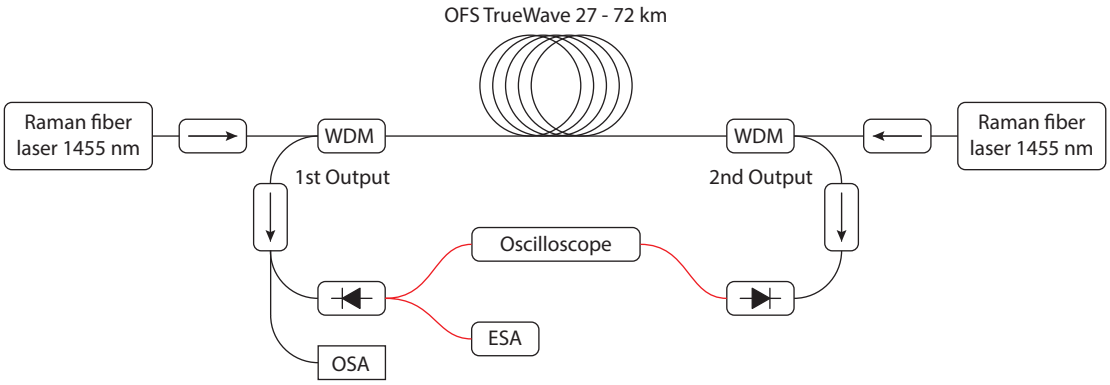

Figure 4.5: Experimental setup. Red lines indicate electrical connection.

Typical optical spectra for different combined pump powers are shown on the Figure 4.6a. At all powers the optical spectrum is typical for Raman RDFL dual peak shape, corresponding to the characteristic for silica glass Raman gain profile. However at pump power below 4 W the peak at 1556 nm is considerably higher than 1565 nm peak. At pump powers higher than 4.4 W the spectral power distribution shifts and the second peak becomes more dominant. This corresponds to the change in the output temporal dynamics, as will be shown later. The power efficiency for all fibre lengths was almost the same, as shown in Figure 4.6b. The lasing threshold was 1.2 W of total pump power and was constant for

all fibre lengths as expected [106]. The slope efficiency reached values of 52% in all cases.

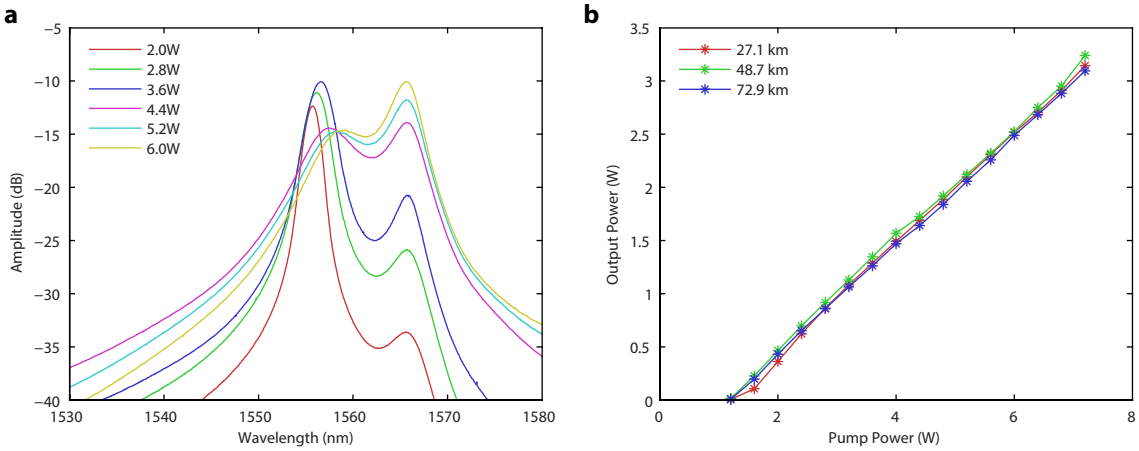

Figure 4.6: a, Typical optical spectrum for different total pump powers for 48.7 km, and **b,** single side power efficiency for different fibre lengths.

Time traces of the output radiation are shown on the Figure 4.7a–f. Temporal dynamics of the output radiation were recorded simultaneously from both outputs. The darker green/red overlay shows the averaged value of the intensity for easier estimation of the shape of the envelope. The noise-like pulses have slowly varying envelope with well defined repetition frequency and stochastic filling, with the shortest structure duration as short as 160 ps, which is probably limited by the measurement equipment. At lower powers pulses leave the cavity synchronously from both ends, and switch into asynchronous and back into synchronous regime with every frequency jump at higher powers. Almost at all pump powers, starting from approximately 2.4 W, pulses leaving from the different ends have different asymmetric shape of the envelope, even though the repetition rate is well defined in both cases. These shapes are the result of interaction of counter-propagating Stokes and pump waves. The break of the symmetry of the output pulses from different outputs is probably connected to the intrinsic asymmetry of the setup, such as slight variation in parameters of the pump power sources and other components. However, shapes of the pulses, and other parameters of the radiation are incredibly stable and repeatable over time and experiment realisations.

The RF spectra at different pump powers for 48.7 km long cavity is shown on the Figure 4.8. The spectrum line-width for the main beating mode is surprisingly narrow at 2 Hz 10 dB level and again the measurements are probably limited by the instrument resolution.

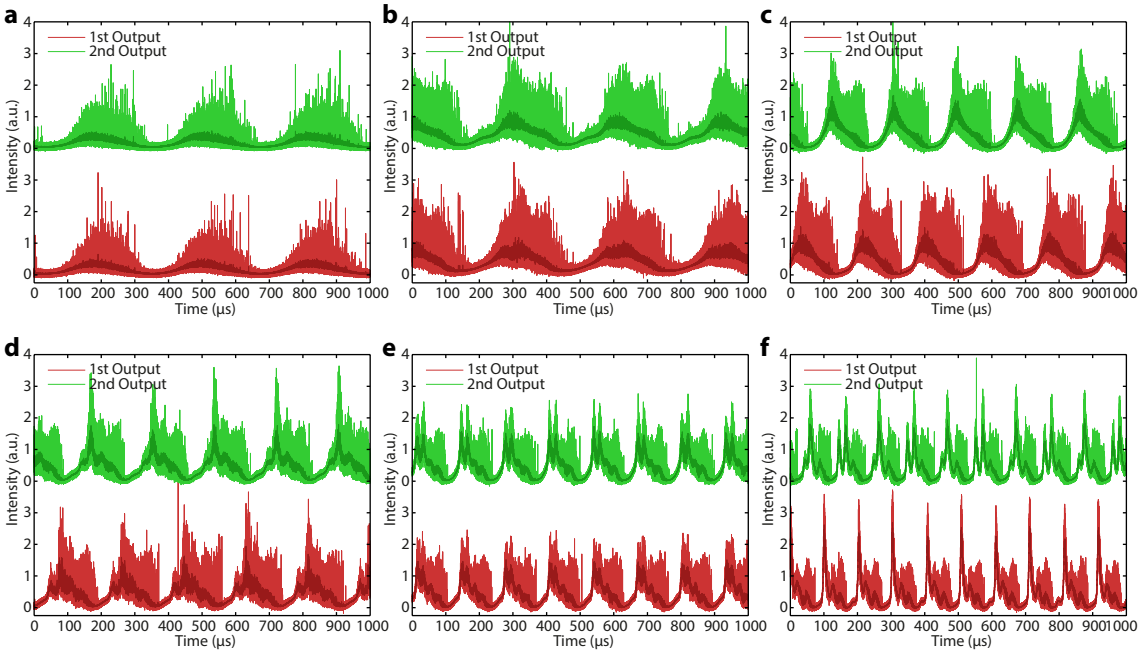

Figure 4.7: Time traces from the experiment for **a,** 2.4 W, **b,** 4 W, **c,** 4.4 W, **d,** 5.6 W, **e,** 6.4 W, and **f,** 7.2 W of pump power.

The contrast is very high and almost reaches 100 dB. All this indicates very high stability of this regime over time. The visible asymmetry of the beating mode could be explained by the asymmetry of the pulses. The front and the tail of the pulse have different timing jitter which is intrinsic to the nature of these pulses. For all pump powers and fibre lengths only 4–5 modes are present in the spectra, with ~20 dB amplitude difference between neighbouring modes. With the increase of pump power transitions to the higher repetition rates occur. These transitions are not smooth and continuous, but happen at the well defined frequencies. The next stable beating mode would appear at the place of a small bump in the RF spectrum, see Figures 4.8a and 4.8b, 4.8b and 4.8c. This indicates some self organisation process of the Stokes and pump waves, which have very stable solutions.

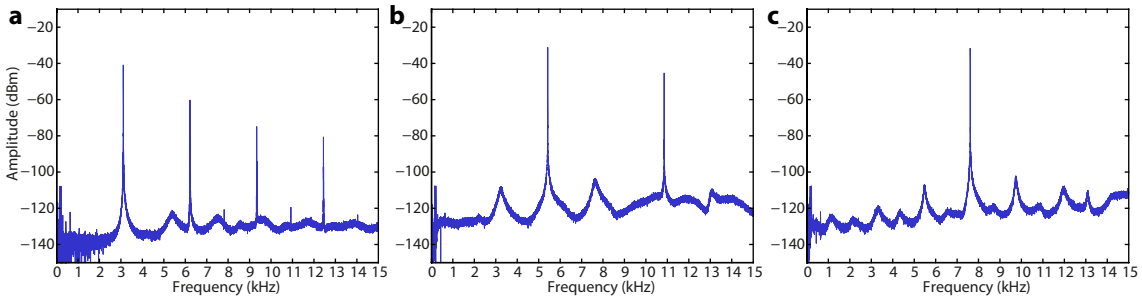

Figure 4.8: RF spectra for the 45 km long cavity at **a,** 2.4 W, **b,** 4.4 W, and **c,** 6.4 W.

Indeed, if we plot repetition rates for all pump powers and different fibre lengths and normalise the frequency to the units $\frac{c}{4Ln}$ we will see clear pattern, Figure 4.9a. The base repetition rate for all fibre lengths up to 48.7 km (fibre length available in the experiment) is close to $\frac{3c}{4Ln}$, or almost 1.5 times higher than the fundamental frequency for the corresponding cavity length, and $\frac{5c}{4Ln}$ for longer spans. With the increase of pump power the repetition rate increases in $\frac{c}{2Ln}$ steps. For the fibres longer than 42.6 km at higher pump powers jumps can occur at $\frac{c}{Ln}$ increments. Interestingly enough, with every $\frac{c}{2Ln}$ increase in the repetition frequency the pulses leaving fibre at different ends change the order from synchronous to antiphase, and vice versa. Repetition rate for a given pump power scales reciprocally to the fibre length as seen on the Figure 4.9b.

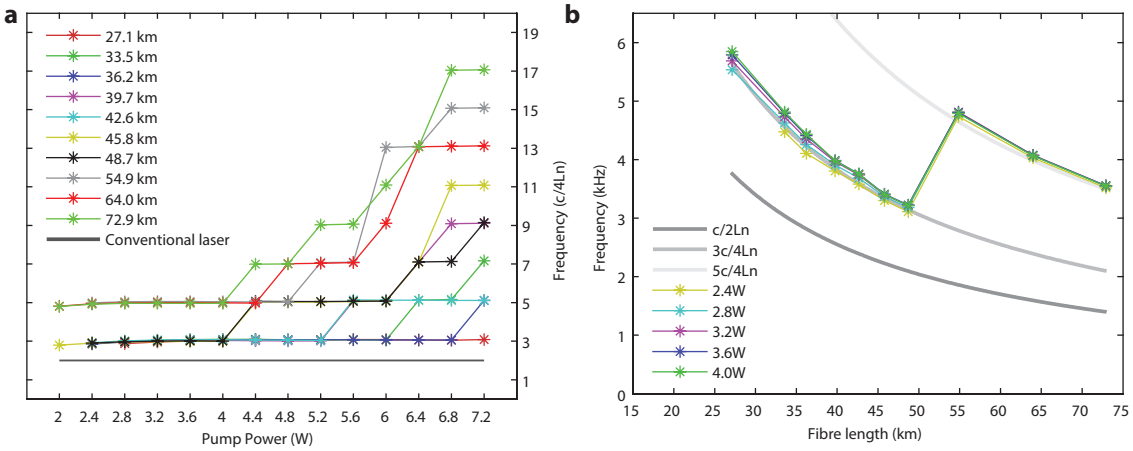

Figure 4.9: a, Scaling of the repetition rate with the total pump power. **b,** Scaling with the fibre length for given total pump power.

Numerical modeling of the temporal dynamics of quasi-q-switch Raman RDFL was done by Prof. Leonid Melnikov and Dr. Yulia Mazhirina. They used power balance equations with added Rayleigh backscattering terms, and solved them numerically by upwind method [191, 192] for spatial derivatives and implicit Euler method for temporal steps:

$$\frac{\partial P_{\mathrm{p}}^{+}}{\partial t}+\frac{\partial P_{\mathrm{p}}^{+}}{\partial z}+\alpha_{\mathrm{p}} P_{\mathrm{p}}^{+}=-g_{\mathrm{R}} P_{\mathrm{p}}^{+}\left(P_{\mathrm{s}}^{+}+P_{\mathrm{s}}^{-}\right), \tag{4.1}$$

$$\frac{\partial P_{\mathrm{p}}^{-}}{\partial t}-\frac{\partial P_{\mathrm{p}}^{-}}{\partial z}+\alpha_{\mathrm{p}} P_{\mathrm{p}}^{-}=-g_{\mathrm{R}} P_{\mathrm{p}}^{-}\left(P_{\mathrm{s}}^{+}+P_{\mathrm{s}}^{-}\right), \tag{4.2}$$

$$\frac{\partial P_{\mathrm{s}}^{+}}{\partial t}+\frac{\partial P_{\mathrm{s}}^{+}}{\partial z}+\alpha_{\mathrm{s}} P_{\mathrm{s}}^{+}=\frac{\lambda_{\mathrm{s}}}{\lambda_{\mathrm{p}}} g_{\mathrm{R}}\left(P_{\mathrm{s}}^{+}+\frac{\hbar \omega_{\mathrm{s}} \Delta \omega_{\mathrm{s}}}{\pi}\right)\left(P_{\mathrm{p}}^{+}+P_{\mathrm{p}}^{-}\right)+r_{\mathrm{s}} \sqrt{P_{\mathrm{s}}^{+} P_{\mathrm{s}}^{-}} \sin [\psi(z)], \tag{4.3}$$

$$\frac{\partial P_{\mathrm{s}}^{-}}{\partial t}-\frac{\partial P_{\mathrm{s}}^{-}}{\partial z}+\alpha_{\mathrm{s}} P_{\mathrm{s}}^{-}=\frac{\lambda_{\mathrm{s}}}{\lambda_{\mathrm{p}}} g_{\mathrm{R}}\left(P_{\mathrm{s}}^{-}+\frac{\hbar \omega_{\mathrm{s}} \Delta \omega_{\mathrm{s}}}{\pi}\right)\left(P_{\mathrm{p}}^{+}+P_{\mathrm{p}}^{-}\right)-r_{\mathrm{s}} \sqrt{P_{\mathrm{s}}^{+} P_{\mathrm{s}}^{-}} \sin [\psi(z)], \tag{4.4}$$

Here $P_{\mathrm{p,s}}^{\pm}$ are powers of pump (p) and Stockes (s) waves, α_{p}, α are the losses for pump and Stokes beams at the fibre length L, g_{R} is the Raman gain, λ_{p}, $\lambda_{\mathrm{s}}=\dfrac{2\pi c}{\omega_{\mathrm{s}}}$ are the wavelengths, $\Delta\omega_{\mathrm{s}}$ is the Raman gain linewidth, + and − superscripts are used for forward and backward waves, r_{s} is Rayleigh back-scattering coefficient, ψ is the phase difference between oppositely running Stokes waves. In these equations z is normalized to L, $0 \leq z \leq 1$, temporal scale unit is round-trip time $T=\dfrac{2L}{v_{\mathrm{gs}}}$, v_{gs} is the group velocity of Stokes waves (for the simplicity $v_{\mathrm{gs}}=v_{\mathrm{gp}}$). The boundary condition are as follows: $P_{\mathrm{p}}^{+}(0)=P_{\mathrm{p0}}^{+}$, $P_{\mathrm{p}}^{-}(1)=P_{\mathrm{p0}}^{-}$, $P_{\mathrm{s}}^{+}(0)=RP_{\mathrm{s}}^{-}(0)$, $P_{\mathrm{s}}^{-}(1)=RP_{\mathrm{s}}^{+}(1)$. Here P_{p0}^{+} and P_{p0}^{-} are the intensities of pumping waves, $R \ll 1$ is the reflection from fibre ends. The term describing Rayleigh scattering corresponds to coupling of amplitudes of forward and backward running waves due to refraction index fluctuations. The phase difference $\psi(z)$ includes the random phase of backscattering and was supposed to be time-independent.

The parameters used in numerical simulations are $L=45$ km, $g_{\mathrm{R}}=0.6\cdot 45$, $\alpha_{\mathrm{p}}=0.055\cdot 45$, $\alpha_{\mathrm{s}}=0.046\cdot 45$, $r_{\mathrm{s}}=\alpha_{\mathrm{s}}/500$, $R=10^{-5}$, $\dfrac{\hbar\omega_{\mathrm{s}}\Delta\omega_{\mathrm{s}}}{\pi}=2\cdot 10^{-7}$.

The results of numerical simulations are shown on the Figure 4.10. The time traces of the slowly varying envelop are in good agreement with experimental data Figure 4.2, with all characteristic features and switching to asynchronous pulse emission present.

In conclusion, very stable quasi-Q-switch operation of a Raman RDFL was achieved in dual backward pumping configuration, with careful control of parasitic back-reflection from the outputs into the cavity and from cavity into the pump lasers. This simple design consisting of only a span of fibre, isolators and pump lasers shows promise in terms of

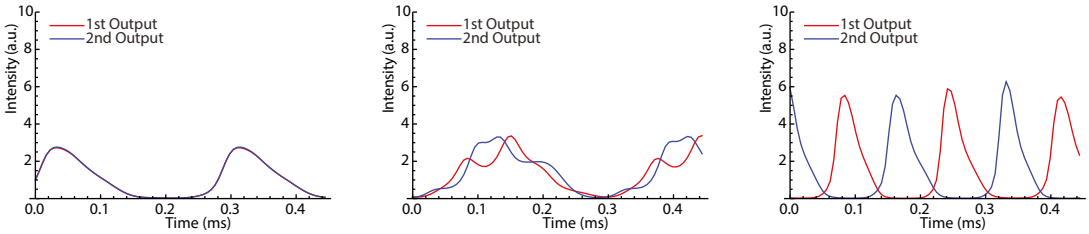

Figure 4.10: Numerically simulated time traces for **a,** 2.4 W, **b,** 4 W, **c,** 4.4 W of pump power.

possible practical applications due to high power, stability and efficiency.

Chapter 5

Conclusions

In conclusion, in this thesis an approach of representing experimental one-dimensional laser intensity data $I(t)$ as two-dimensional spatio-temporal intensity dynamics $I(t, z)$ was described in detail. Using intrinsic periodicity of the laser radiation, evolution of the light in the cavity over many roundtrips can be plotted and spatio-temporal regimes of generation can be revealed.

Using this technique for analysis of radiation from 1 km long Raman fibre laser allowed to observe in experiment the laminar-turbulent transition for the first time. The mechanism responsible for this transition – clustering of dark solitons, was also identified in the experiment, as any coherent structure, such as dark or bright soliton, could be easily tracked on spatio-temporal picture. The observation of such transition, which is analogous to the laminar-turbulent transition in hydrodynamics is very important as it reveals an interesting and potentially useful analogy, yet another common phenomenon between the fields, besides solitons, rogue waves, breathers and others. It is possible, that this technique could lead to the discovery of other physical processes similar in both fields, which might have a high practical impact.

In this work, application of this technique to the analysis of radiation of Raman fibre laser at different pump powers revealed various spatio-temporal regimes of generation, such as partial mode-lock, turbulent and a regime with short-lived pulses over stochastic background. While these regimes look very similar in temporal domain, they are distinctively different in spatio-temporal properties and in this case we can talk about different spatio-

temporal regimes of generation, in contrast with temporal regimes, such as CW, mode-lock or q-switch. Two-dimensional auto-correlation analysis performed on the spatio-temporal pictures allowed to reveal periodicity properties both over fast time and slow evolution coordinate, track changes in the average temporal width and life-time of the emerged structures over the power. Such spatio-temporal treatment of the intensity dynamics is very helpful in the analysis of the complex stochastic radiation of a Raman fibre laser, however its applicability could be extended to any laser system, to obtain extra information about the properties of the radiation.

Further extension of the technique into spectral domain could help in the analysis of spectral fluctuations of the laser output dynamics, which together with the intensity spatio-temporal picture could help to study the fundamental questions of the coherent structures formation from noise, such as solitons and similaritons. Future work will be concentrated on the development of comprehensive comparison between numerical models and experimental data. The power of this approach is in the ability to compare the model and the experiment on short and long time scales simultaneously by simple visual comparison of the spatio-temporal pictures. All of the demonstrated techniques can be successfully applied to other types of lasers, such as semiconductor, solid state etc.

Using MR pulse regeneration mechanism, mode-locking was achieved in a simple linear cavity Raman fibre laser. In the setup consisting of a piece of fibre and two spectrally shifted unchirped FBGs acting as cavity mirrors, 7500 order harmonic mode-locking was achieved, with 80 ps long pulses. The laser readily mode-locks, with no additional polarisation or other degrees of freedom control, as long as the required FBGs spectral separation is set and the pump power is above the threshold. One of the drawbacks of this design is very large supermode noise and the associated jitter, which could be a big limiting factor in applications where stable pulse repetition rate is required. Another drawback is the fact that a lot of energy is filtered out by the gratings and effectively lost in the process of pulse regeneration. This greatly reduces the overall effectiveness of this configuration. By introducing Faraday parametric instability through dispersion modulation even higher up to 240000 order harmonic mode-locking was achieved in the same configuration, with pulse repetition rates as high as 12 GHz and pulse duration 7.3 ps. The proposed design is very

simple, easy to adjust, and stable. However, again, this configuration suffered from the same drawbacks.

Faraday parametric instability, as a method for exciting stable patterns could be extended to other laser systems and configurations, such as for example ring cavity laser with doped fibres as an amplifying media. Future work is aimed at the development of more efficient laser cavity designs to improve the overall efficiency, and jitter suppression, which should greatly increase attractiveness of the proposed mechanism.

By careful control of parasitic back-reflections in double-arm backward pumped random distributed feedback Raman fibre laser, stable quasi-q-switch operation was achieved. Pulse duration and repetition rate depended on pump power and fibre length, and varied from 100–200 μs at low pump powers to 40–50 μs at high pump powers, with scaling experimentally identified. The slope efficiency was as high as 52% with combined output power up to 3.3 W irrespectively of fibre length. Extremely simple configuration and good power scalability make this design particularly interesting for applications were pulsed high power pump source is required, such as material processing. The pulse quality, however, is a considerable drawback of this design. Stochastic, noise-like pulses drastically limit the range of possible applications. The pulse repetition rate, however, was very stable, and repeatable. Results of this work can find applications in the study of stability and noise performance of distributed Raman amplifiers in telecommunications. Future work in this area can be aimed at the development of one sided output for more efficient and convenient utilisation of the output radiation.

Bibliography

[1] Hollenbeck, D. & Cantrell, C. Multiple-vibrational-mode model for fiber-optic raman gain spectrum and response function. *J. Opt. Soc. Am. B* **19**, 2886–2892 (2002).

[2] Raman, C. & Krishnan, K. A new type of secondary radiation. *Nature* **121**, 501–502 (1928).

[3] Shuker, R. & Gammon, R. W. Raman-Scattering Selection-Rule Breaking and the Density of States in Amorphous Materials. *Phys. Rev. Lett.* **25**, 222–225 (1970).

[4] Stolen, R. H. Raman gain in glass optical waveguides. *Appl. Phys. Lett.* **22**, 276 (1973).

[5] Agrawal, G. *Nonlinear fiber optics* (Academic Press, 2000).

[6] AuYeung, J. & Yariv, A. Theory of cw Raman oscillation in optical fibers. *J. Opt. Soc. Am.* **69**, 803–807 (1979).

[7] Hill, K. O., Kawasaki, B. S. & Johnson, D. C. Low-threshold cw Raman laser. *Appl. Phys. Lett.* **29**, 181 (1976).

[8] Kean, P. *et al.* Experimental Evaluation of a Fibre Raman Oscillator Having Fibre Grating Reflectors. *Journal of Modern Optics* **35**, 397–406 (1988).

[9] Grubb, S. G. *et al.* 1.3 μm cascaded raman amplifier in germanosilicate fibers. In *Optical Amplifiers and Their Applications*, PD3 (Optical Society of America, 1994).

[10] Headley, C. & Agrawal, G. P. Unified description of ultrafast stimulated Raman scattering in optical fibers. *J. Opt. Soc. Am. B* **13**, 2170–2177 (1996).

[11] Churkin, D. V., Smirnov, S. V. & Podivilov, E. V. Statistical properties of partially coherent cw fiber lasers. *Opt. Lett.* **35**, 3288–90 (2010).

[12] Churkin, D. V., Gorbunov, O. A. & Smirnov, S. V. Extreme value statistics in Raman fiber lasers. *Opt. Lett.* **36**, 3617–3619 (2011).

[13] Churkin, D. V. & Smirnov, S. V. Numerical modelling of spectral, temporal and statistical properties of Raman fiber lasers. *Opt. Commun.* **285**, 2154–2160 (2012).

[14] Randoux, S., Dalloz, N. & Suret, P. Intracavity changes in the field statistics of Raman fiber lasers. *Opt. Lett.* **36**, 790–2 (2011).

[15] Aguergaray, C., Méchin, D., Kruglov, V. & Harvey, J. Experimental realization of a mode-locked parabolic Raman fiber oscillator. *Opt. Express* **18**, 8680–8687 (2010).

[16] Babin, S. A., Churkin, D. V., Ismagulov, A. E., Kablukov, S. I. & Podivilov, E. V. Four-wave-mixing-induced turbulent spectral broadening in a long Raman fiber laser. *J. Opt. Soc. Am. B* **24**, 1729 (2007).

[17] Chichkov, B. N., Momma, C., Nolte, S., von Alvensleben, F. & Tünnermann, A. Femtosecond, picosecond and nanosecond laser ablation of solids. *Appl. Phys. A* **63**, 109–115 (1996).

[18] Juhasz, T., Kastis, G. A., Suárez, C., Bor, Z. & Bron, W. E. Time-resolved observations of shock waves and cavitation bubbles generated by femtosecond laser pulses in corneal tissue and water. *Lasers in Surgery and Medicine* **19**, 23–31 (1996).

[19] Boivin, L., Wegmueller, M., Nuss, M. C. & Knox, W. H. 110 channels x 2.35 Gb/s from a single femtosecond laser. *Photonics Technology Letters, IEEE* **11**, 466–468 (1999).

[20] Tan, H. N., Inoue, T., Kurosu, T. & Namiki, S. Transmission and pass-drop operations of mixed baudrate Nyquist OTDM-WDM signals for all-optical elastic network. *Opt. Express* **21**, 20313–20321 (2013).

[21] Udem, T., Reichert, J., Holzwarth, R. & Hänsch, T. W. Absolute Optical Frequency Measurement of the Cesium D_1 Line with a Mode-Locked Laser. *Phys. Rev. Lett.* **82**, 3568–3571 (1999).

[22] Schibli, T. R. *et al.* Optical frequency comb with submillihertz linewidth and more than 10 W average power. *Nature Photon.* **2**, 355–359 (2008).

[23] Baumann, E. *et al.* High-performance, vibration-immune, fiber-laser frequency comb. *Opt. Lett.* **34**, 638–640 (2009).

[24] Dudley, J. M., Coen, S., Genty, G. & Coen, S. Supercontinuum generation in photonic crystal fiber. *Reviews of Modern Physics* **78**, 1135–1184 (2006).

[25] Galli, I. *et al.* Molecular Gas Sensing Below Parts Per Trillion: Radiocarbon-Dioxide Optical Detection. *Phys. Rev. Lett.* **107**, 270802 (2011).

[26] Mears, R. J., Reekie, L., Jauncey, I. M. & Payne, D. N. Low-noise erbium-doped fibre amplifier operating at 1.54 μm. *Electronics Letters* **23**, 1026–1028 (1987).

[27] Desurvire, E., Simpson, J. R. & Becker, P. C. High-gain erbium-doped traveling-wave fiber amplifier. *Opt. Lett.* **12**, 888–890 (1987).

[28] Träger, F. *Springer Handbook of Lasers and Optics*, vol. 72 (Springer, 2007).

[29] Gürs, K. & Müller, R. Breitband-modulation durch Steuerung der emission eines optischen masers (Auskopple-modulation). *Phys. Lett.* **5**, 179–181 (1963).

[30] Lamb, W. Theory of an Optical Maser. *Physical Review* **134**, A1429–A1450 (1964).

[31] Agrawal, G. *Applications of nonlinear fiber optics* (Academic Press, 2001).

[32] Smith, P. W., Duguay, M. A. & Ippen, E. P. Mode-locking of lasers. *Progress in Quantum Electronics* **3**, 107–229 (1974).

[33] Hargrove, L. E., Fork, R. L. & Pollack, M. a. Locking of He-Ne laser modes induced by synchronous intracavity modulation. *Appl. Phys. Lett.* **5**, 4–5 (1964).

[34] Crowell, M. Characteristics of mode-coupled lasers. *IEEE J. Quantum Elect.* **1**, 12–20 (1965).

[35] DiDomenico, M. Small-Signal Analysis of Internal (Coupling-Type) Modulation of Lasers. *J. Appl. Phys.* **35**, 2870 (1964).

[36] Huggett, G. R. Mode-Locking of Cw Lasers By Regenerative Rf Feedback. *Appl. Phys. Lett.* **13**, 186 (1968).

[37] Kuizenga, D. I. & Siegman, A. E. Modulator frequency detuning effects in the FM mode-locked laser. *IEEE J. Quantum Elect.* **QE-6**, 803–808 (1970).

[38] Haus, H. Mode-locking of lasers. *IEEE J. Sel. Top. Quant.* **6**, 1173–1185 (2000).

[39] Becker, M., Kuizenga, D. & Siegman, A. Harmonic mode locking of the Nd:YAG laser. *IEEE J. Quantum Elect.* **8**, 687–693 (1972).

[40] Kafka, J. D., Baer, T. & Hall, D. W. Mode-locked erbium-doped fiber laser with soliton pulse shaping. *Opt. Lett.* **14**, 1269 (1989).

[41] Takada, A. & Miyazawa, H. 30 GHz picosecond pulse generation from actively mode-locked erbium-doped fibre laser. *Electronics Letters* **26**, 216 (1990).

[42] Kubota, H., Nakazawa, M., Kimura, Y. & Yoshida, E. Generation of a 170 fs, 10 GHz transform-limited pulse train at 1.55 μm using a dispersion-decreasing, erbium-doped active soliton compressor. *Electronics Letters* **30**, 2038–2040 (1994).

[43] DeMaria, A. J. Self Mode-Locking of Lasers With Saturable Absorbers. *Appl. Phys. Lett.* **8**, 174 (1966).

[44] Ippen, E. Passive mode locking of the cw dye laser. *Appl. Phys. Lett.* **21**, 348 (1972).

[45] Arthurs, E. G., Bradley, D. J. & Roddie, A. G. Buildup of picosecond pulse generation in passively mode-locked rhodamine dye lasers. *Appl. Phys. Lett.* **23** (1973).

[46] New, G. Mode-locking of quasi-continuous lasers. *Opt. Commun.* **6**, 188–192 (1972).

[47] Ippen, E. P. Principles of passive mode locking. *Appl. Phys. B Laser and Optics* **58**, 159–170 (1994).

[48] Ippen, E. P., Eilenberger, D. J. & Dixon, R. W. Picosecond pulse generation by passive mode locking of diode lasers. *Appl. Phys. Lett.* **37** (1980).

[49] Arahira, S., Matsui, Y. & Ogawa, Y. Mode-locking at very high repetition rates more than terahertz in passively mode-locked distributed-Bragg-reflector laser diodes. *IEEE J. Quantum Elect.* **32**, 1211–1224 (1996).

[50] Islam, M. N. *et al.* Color center lasers passively mode locked by quantum wells. *IEEE J. Quantum Elect.* **25**, 2454–2463 (1989).

[51] Keller, U. *et al.* Semiconductor saturable absorber mirrors (SESAM's) for femtosecond to nanosecond pulse generation in solid-state lasers. *IEEE J. Sel. Top. Quant.* **2**, 435–453 (1996).

[52] Guerreiro, P. T. *et al.* PbS quantum-dot doped glasses as saturable absorbers for mode locking of a Cr:forsterite laser. *Appl. Phys. Lett.* **71**, 1595 (1997).

[53] Set, S., Yaguchi, H., Tanaka, Y. & Jablonski, M. Laser Mode Locking Using a Saturable Absorber Incorporating Carbon Nanotubes. *J. Lightwave Technol.* **22**, 51–56 (2004).

[54] Shohda, F., Shirato, T., Nakazawa, M., Mata, J. & Tsukamoto, J. 147 fs, 51 MHz soliton fiber laser at 1.56 microm with a fiber-connector-type SWNT/P3HT saturable absorber. *Opt. Express* **16**, 20943–8 (2008).

[55] von der Linde, D. & Rodgers, K. F. Recovery time of saturable absorbers for 1.06 u. *IEEE J. Quantum Elect.* **9**, 960–961 (1973).

[56] Schmidt, A. *et al.* Passive mode locking of Yb:KLuW using a single-walled carbon nanotube saturable absorber. *Opt. Lett.* **33**, 729–731 (2008).

[57] Schmidt, A. *et al.* Sub-100 fs single-walled carbon nanotube saturable absorber mode-locked Yb-laser operation near 1 μm. *Opt. Express* **17**, 20109–20116 (2009).

[58] Ober, M. H., Keiler, U., Chiu, T. H. & Hofer, M. Self-starting diode-pumped femtosecond Nd fiber laser. *Opt. Lett.* **18**, 1532–1534 (1993).

[59] Doran, N. J. & Wood, D. Nonlinear-optical loop mirror. *Opt. Lett.* **13**, 56–58 (1988).

[60] Blow, K. J., Doran, N. J. & Nayar, B. K. Experimental demonstration of optical soliton switching in an all-fiber nonlinear Sagnac interferometer. *Opt. Lett.* **14**, 754–756 (1989).

[61] Fermann, M. E., Haberl, F., Hofer, M. & Hochreiter, H. Nonlinear amplifying loop mirror. *Opt. Lett.* **15**, 752–4 (1990).

[62] Duling, I. All-fiber ring soliton laser mode locked with a nonlinear mirror. *Opt. Lett.* **16**, 539–41 (1991).

[63] Richardson, D., Laming, R., Payne, D., Phillips, M. & Matsas, V. 320 fs soliton generation with passively mode-locked erbium fibre laser. *Electronics Letters* **27**, 730 (1991).

[64] Nakazawa, M., Yoshida, E. & Kimura, Y. Low threshold, 290 fs erbium-doped fiber laser with a nonlinear amplifying loop mirror pumped by InGaAsP laser diodes. *Appl. Phys. Lett.* **59**, 2073 (1991).

[65] Nakazawa, M., Yoshida, E. & Kimura, Y. Generation of 98 fs optical pulses directly from an erbium-doped fibre ring laser at 1·57 μm. *Electronics Letters* **29**, 63– (1993).

[66] Fermann, M. E. Passive mode locking by using nonlinear polarization evolution in a polarization-maintaining erbium-doped fiber. *Opt. Lett.* **18**, 894 (1993).

[67] Matsas, V., Newson, T., Richardson, D. & Payne, D. Selfstarting passively mode-locked fibre ring soliton laser exploiting nonlinear polarisation rotation. *Electronics Letters* **28**, 1391 (1992).

[68] Tamura, K., Ippen, E. P., Haus, H. A. & Nelson, L. E. 77-fs pulse generation from a stretched-pulse mode-locked all-fiber ring laser. *Opt. Lett.* **18**, 1080 (1993).

[69] Winful, H. G. & Walton, D. T. Passive mode locking through nonlinear coupling in a dual-core fiber laser. *Opt. Lett.* **17**, 1688 (1992).

[70] Cheo, P., Wang, L. & Ding, M. Low-threshold, self-tuned and passively mode-locked coupled-cavity all-fiber lasers. *IEEE Photonic. Tech. L.* **8**, 66–68 (1996).

[71] Hudson, D. D. *et al.* Nonlinear femtosecond pulse reshaping in waveguide arrays. *Opt. Lett.* **33**, 1440–2 (2008).

[72] Snitzer, E. Optical maser action of Nd^{+3} in a barium crown glass. *Phys. Rev. Lett.* **7**, 444–446 (1961).

[73] Loh, W. H. *et al.* All-solid-state subpicosecond passively mode locked erbium-doped fiber laser. *Appl. Phys. Lett.* **63**, 4 (1993).

[74] Okhotnikov, O. G., Gomes, L., Xiang, N., Jouhti, T. & Grudinin, a. B. Mode-locked Ytterbium fiber laser tunable in the 980-1070-nm spectral range. *Opt. Lett.* **28**, 1522–4 (2003).

[75] Cautaerts, V., Richardson, D. J., Paschotta, R. & Hanna, D. C. Stretched pulse Yb(3+)silica fiber laser. *Opt. Lett.* **22**, 316–8 (1997).

[76] de Matos, C. J. S., Chestnut, D. a. & Taylor, J. R. Low-threshold self-induced modulational instability ring laser in highly nonlinear fiber yielding a continuous-wave 262-GHz soliton train. *Opt. Lett.* **27**, 915–7 (2002).

[77] Tang, D. Y. & Zhao, L. M. Generation of 47-fs pulses directly from an erbium-doped fiber laser. *Opt. Lett.* **32**, 41–43 (2007).

[78] Kafka, J. D. & Baer, T. Fiber Raman soliton laser pumped by a Nd:YAG laser. *Opt. Lett.* **12**, 181–3 (1987).

[79] Schröder, J., Coen, S., Vanholsbeeck, F. & Sylvestre, T. Passively mode-locked Raman fiber laser with 100 GHz repetition rate. *Opt. Lett.* **31**, 3489–91 (2006).

[80] Ilday, F. Ö. & Wise, F. W. Nonlinearity management: a route to high-energy soliton fiber lasers. *J. Opt. Soc. Am. B* **19**, 470 (2002).

[81] Chong, A., Renninger, W. H. & Wise, F. W. Properties of normal-dispersion femtosecond fiber lasers. *J. Opt. Soc. Am. B* **25**, 140 (2008).

[82] Fermann, M. E., Kruglov, V. I., Thomsen, B. C., Dudley, J. M. & Harvey, J. D. Self-similar propagation and amplification of parabolic pulses in optical fibers. *Phys. Rev. Lett.* **84**, 6010–3 (2000).

[83] Finot, C., Millot, G., Billet, C. & Dudley, J. Experimental generation of parabolic pulses via Raman amplification in optical fiber. *Opt. Express* **11**, 1547–52 (2003).

[84] Anderson, D., Desaix, M., Karlsson, M., Lisak, M. & Quiroga-Teixeiro, M. L. Wave-breaking-free pulses in nonlinear-optical fibers. *J. Opt. Soc. Am. B* **10**, 1185 (1993).

[85] Tomlinson, W. J., Stolen, R. H. & Johnson, A. M. Optical wave breaking of pulses in nonlinear optical fibers. *Opt. Lett.* **10**, 457 (1985).

[86] Ilday, F., Buckley, J., Clark, W. & Wise, F. Self-Similar Evolution of Parabolic Pulses in a Laser. *Phys. Rev. Lett.* **92**, 1–4 (2004).

[87] An, J., Kim, D., Dawson, J. W., Messerly, M. J. & Barty, C. P. J. Grating-less, fiber-based oscillator that generates 25 nJ pulses at 80 MHz, compressible to 150 fs. *Opt. Lett.* **32**, 2010 (2007).

[88] Buckley, J. R., Wise, F. W., Ilday, F. O. & Sosnowski, T. Femtosecond fiber lasers with pulse energies above 10 nJ. *Opt. Lett.* **30**, 1888–90 (2005).

[89] Renninger, W. H., Chong, A. & Wise, F. W. Self-similar pulse evolution in an all-normal-dispersion laser. *Phys. Rev. A* **82**, 3–6 (2010).

[90] Lefrancois, S. *et al.* High-energy similariton fiber laser using chirally coupled core fiber. *Opt. Lett.* **38**, 43–5 (2013).

[91] Chong, A., Buckley, J., Renninger, W. & Wise, F. All-normal-dispersion femtosecond fiber laser. *Opt. Express* **14**, 10095 (2006).

[92] Nielsen, C. K. *et al.* Self-starting self-similar all-polarization maintaining Yb-doped fiber laser. *Opt. Express* **13**, 9346 (2005).

[93] Prochnow, O., Ruehl, A., Schultz, M., Wandt, D. & Kracht, D. All-fiber similariton laser at 1 mum without dispersion compensation. *Opt. Express* **15**, 6889–93 (2007).

[94] Oktem, B., Ülgüdür, C. & Ilday, F. Ö. Soliton-similariton fibre laser. *Nature Photon.* **4**, 307–311 (2010).

[95] Finot, C. & Millot, G. Synthesis of optical pulses by use of similaritons. *Opt. Express* **12**, 5104–9 (2004).

[96] Castellani, C. E. S. *et al.* Ultrafast Raman laser mode-locked by nanotubes. *Opt. Lett.* **36**, 3996 (2011).

[97] Kruglov, V. I., Méchin, D. & Harvey, J. D. All-fiber ring Raman laser generating parabolic pulses. *Phys. Rev. A* **81**, 023815 (2010).

[98] Finot, C., Dudley, J. M. & Millot, G. Generation of dark solitons by interaction between similaritons in Raman fiber amplifiers. *Optical Fiber Technology* **12**, 217–226 (2006).

[99] Ruehl, A. *et al.* Parabolic Pulse Regime of an Ultrafast Fiber Laser. In *Advanced Solid-State Photonics*, vol. 1, TuB2 (OSA, Washington, D.C., 2007).

[100] Nyushkov, B. N. *et al.* Gamma-shaped long-cavity normal-dispersion mode-locked Er-fiber laser for sub-nanosecond high-energy pulsed generation. *Laser Physics Letters* **9**, 59–67 (2012).

[101] Pitois, S., Finot, C., Provost, L. & Richardson, D. J. Generation of localized pulses from incoherent wave in optical fiber lines made of concatenated Mamyshev regenerators. *J. Opt. Soc. Am. B* **25**, 1537 (2008).

[102] Letokhov, V. Generation of Light by a Scattering Medium with Negative Resonance Absorption. *Soviet Journal of Experimental and Theoretical Physics* **26**, 835 (1968).

[103] Gouedard, C., Auzel, F., Migus, A., Husson, D. & Sauteret, C. Generation of spatially incoherent short pulses in laser-pumped neodymium stoichiometric crystals and powders. *J. Opt. Soc. Am. B* **10**, 2358–2363 (1993).

[104] Lawandy, N. M., Balachandran, R. M., Gomes, A. S. L. & Sauvain, E. Laser action in strongly scattering media. *Nature* **368**, 436–438 (1994).

[105] Turitsyn, S. K. *et al.* Random distributed feedback fibre laser. *Nature Photon.* **4**, 231–235 (2010).

[106] Churkin, D. *et al.* Raman fiber lasers with a random distributed feedback based on Rayleigh scattering. *Phys. Rev. A* **82**, 033828 (2010).

[107] Turitsyn, S. K. *et al.* Random distributed feedback fibre lasers. *Physics Reports* **542**, 133–193 (2014).

[108] Barnoski, M. K., Rourke, M. D., Jensen, S. M. & Melville, R. T. Optical time domain reflectometer. *Appl. Opt.* **16**, 2375–2379 (1977).

[109] Chen, C.-J., Lee, H. K. & Cheng, Y.-J. Instability in Raman Amplifiers Caused by Distributed Rayleigh Reflection. In *Optical Fiber Communication Conference*, TuC2 (Optical Society of America, 2003).

[110] Turitsyn, S. *et al.* 270-km Ultralong Raman Fiber Laser. *Phys. Rev. Lett.* **103**, 133901 (2009).

[111] Babin, S. A. *et al.* Turbulent broadening of optical spectra in ultralong Raman fiber lasers. *Phys. Rev. A* **77**, 33803 (2008).

[112] Churkin, D. V., El-Taher, a. E., Vatnik, I. D. & Babin, S. a. Study of the longitudinal distribution of power generated in a random distributed feedback Raman fibre laser with unidirectional pumping. *Quantum Electronics* **42**, 774–777 (2012).

[113] Churkin, D. V. *et al.* Experimental and theoretical study of longitudinal power distribution in a random DFB fiber laser. *Opt. Express* **20**, 11178–88 (2012).

[114] Sugavanam, S., Tarasov, N., Shu, X. & Churkin, D. V. Narrow-band generation in random distributed feedback fiber laser. *Opt. Express* **21**, 16466–16472 (2013).

[115] Sugavanam, S., Yan, Z. & Kamynin, V. Multiwavelength generation in a random distributed feedback fiber laser using an all fiber Lyot filter. *Opt. Express* **22**, 2839–44 (2014).

[116] Yan, Z. *et al.* All-fiber polarization interference filters based on 45°-tilted fiber gratings. *Opt. Lett.* **37**, 353–355 (2012).

[117] Yan, Z., Zhou, K. & Zhang, L. In-fiber linear polarizer based on UV-inscribed 45° tilted grating in polarization maintaining fiber. *Opt. Lett.* **37**, 3819–3821 (2012).

[118] Babin, S. A., El-Taher, A. E., Harper, P., Podivilov, E. V. & Turitsyn, S. K. Tunable random fiber laser. *Phys. Rev. A* **84**, 21805 (2011).

[119] Reeves-Hall, P. C. & Taylor, J. R. Wavelength tunable CW Raman fibre ring laser operating at 1486-1551 nm. *Electronics Letters* **37**, 491–492 (2001).

[120] Yeo, K. S., Mahdi, M. A., Mohamad, H., Hitam, S. & Mokhtar, M. Widely tunable Raman ring laser using highly nonlinear fiber. *Laser Physics* **19**, 2200–2203 (2009).

[121] Zhu, Y. Y., Zhang, W. L. & Jiang, Y. Tunable Multi-Wavelength Fiber Laser Based on Random Rayleigh Back-Scattering. *Photonics Technology Letters, IEEE* **25**, 1559–1561 (2013).

[122] Vatnik, I. D., Churkin, D. V., Babin, S. A. & Turitsyn, S. K. Cascaded random distributed feedback Raman fiber laser operating at 1.2 μm. *Opt. Express* **19**, 18486–18494 (2011).

[123] Pinto, A. M. R., Frazão, O., Santos, J. L. & Lopez-Amo, M. Multiwavelength fiber laser based on a photonic crystal fiber loop mirror with cooperative Rayleigh scattering. *Appl. Phys. B* **99**, 391–395 (2010).

[124] El-Taher, A. E. *et al.* Effect of Rayleigh-scattering distributed feedback on multiwavelength Raman fiber laser generation. *Opt. Lett.* **36**, 130–132 (2011).

[125] Pang, M. *et al.* Rayleigh scattering-assisted narrow linewidth Brillouin lasing in cascaded fiber. *Opt. Lett.* **37**, 3129–31 (2012).

[126] Rao, Y. J. *et al.* Hybrid lasing in an ultra-long ring fiber laser. *Opt. Express* **20**, 22563–22568 (2012).

[127] Pinto, A. M. R., Lopez-Amo, M., Kobelke, J. & Schuster, K. Temperature Fiber Laser Sensor Based on a Hybrid Cavity and a Random Mirror. *J. Lightwave Technol.* **30**, 1168–1172 (2012).

[128] Nuño, J., Alcon-Camas, M. & Ania-Castañón, J. D. RIN transfer in random distributed feedback fiber lasers. *Opt. Express* **20**, 27376–27381 (2012).

[129] Wiersma, D. S. Disordered photonics. *Nature Photon.* **7**, 188–196 (2013).

[130] Vatnik, I. D., Churkin, D. V. & Babin, S. a. Power optimization of random distributed feedback fiber lasers. *Opt. Express* **20**, 28033–8 (2012).

[131] Cao, H. *et al.* Spatial Confinement of Laser Light in Active Random Media. *Phys. Rev. Lett.* **84**, 5584–5587 (2000).

[132] Mujumdar, S., Ricci, M., Torre, R. & Wiersma, D. S. Amplified Extended Modes in Random Lasers. *Phys. Rev. Lett.* **93**, 53903 (2004).

[133] Türeci, H. E., Ge, L., Rotter, S. & Stone, A. D. Strong Interactions in Multimode Random Lasers. *Science* **320**, 643–646 (2008).

[134] Fallert, J. *et al.* Co-existence of strongly and weakly localized random laser modes. *Nature Photon.* **3**, 279–282 (2009).

[135] Stano, P. & Jacquod, P. Suppression of interactions in multimode random lasers in the Anderson localized regime. *Nature Photon.* **7**, 66–71 (2013).

[136] Wang, Z., Jia, X., Rao, Y., Jiang, Y. & Zhang, W. Novel long-distance fiber-optic sensing systems based on random fiber lasers. In *Proc. SPIE*, vol. 8351, 835142–835144 (2012).

[137] Vanneste, C., Sebbah, P. & Cao, H. Lasing with Resonant Feedback in Weakly Scattering Random Systems. *Phys. Rev. Lett.* **98**, 143902 (2007).

[138] Berger, G. A., Kempe, M. & Genack, A. Z. Dynamics of stimulated emission from random media. *Phys. Rev. E* **56**, 6118–6122 (1997).

[139] Wu, X., Andreasen, J., Cao, H. & Yamilov, A. Effect of local pumping on random laser modes in one dimension. *J. Opt. Soc. Am. B* **24**, A26—-A33 (2007).

[140] Xie, Y. & Liu, Z. A new physical model on lasing in active random media. *Physics Letters A* **341**, 339–344 (2005).

[141] Jiang, X. & Soukoulis, C. M. Time Dependent Theory for Random Lasers. *Phys. Rev. Lett.* **85**, 70–73 (2000).

[142] Lü, J., Liu, J., Liu, H., Wang, K. & Wang, S. Theoretical investigation on temporal properties of random lasers pumped by femtosecond-lasing pulses. *Opt. Commun.* **282**, 2104–2109 (2009).

[143] Andreasen, J. & Cao, H. Numerical study of amplified spontaneous emission and lasing in random media. *Phys. Rev. A* **82**, 63835 (2010).

[144] Smirnov, S. V. & Churkin, D. V. Modeling of spectral and statistical properties of a random distributed feedback fiber laser. *Opt. Express* **21**, 21236–21241 (2013).

[145] Smith, R. G. Optical Power Handling Capacity of Low Loss Optical Fibers as Determined by Stimulated Raman and Brillouin Scattering. *Appl. Opt.* **11**, 2489–2494 (1972).

[146] Mermelstein, M. D., Posey, R., Johnson, G. A. & Vohra, S. T. Rayleigh scattering optical frequency correlation in a single-mode optical fiber. *Opt. Lett.* **26**, 58–60 (2001).

[147] Zervas, M. N. & Laming, R. Rayleigh scattering effect on the gain efficiency and noise of erbium-doped fiber amplifiers. *IEEE J. Quantum Elect.* **31**, 468–471 (1995).

[148] Suret, P., Doutté, A. & Randoux, S. Influence of light polarization on dynamics of all-fiber Raman lasers: theoretical analysis. *Opt. Lett.* **29**, 2166–2168 (2004).

[149] Dianov, E. M., Luchnikov, A. V., Pilipetskii, A. N. & Prokhorov, A. M. Long-range interaction of picosecond solitons through excitation of acoustic waves in optical fibers. *Appl. Phys. B Photophysics and Laser Chemistry* **54**, 175–180 (1992).

[150] Fellegara, A. & Wabnitz, S. Electrostrictive cross-phase modulation of periodic pulse trains in optical fibers. *Opt. Lett.* **23**, 1357–1359 (1998).

[151] Jang, J. K., Erkintalo, M., Murdoch, S. G. & Coen, S. Ultraweak long-range interactions of solitons observed over astronomical distances. *Nature Photon.* **7**, 657–663 (2013).

[152] Jaouën, Y., du Mouza, L. & Debarge, G. Electrostriction-induced acoustic effect in ultralong-distance soliton transmission systems. *Opt. Lett.* **23**, 1185–1187 (1998).

[153] Dianov, E. M., Luchnikov, A. V., Pilipetskii, A. N. & Starodumov, A. N. Electrostriction mechanism of soliton interaction in optical fibers. *Opt. Lett.* **15**, 314–316 (1990).

[154] Melloni, A., Frasca, M., Garavaglia, A., Tonini, A. & Martinelli, M. Direct measurement of electrostriction in optical fibers. *Opt. Lett.* **23**, 691–693 (1998).

[155] Fellegara, A., Melloni, A. & Martinelli, M. Measurement of the frequency response induced by electrostriction in optical fibers. *Opt. Lett.* **22**, 1615–1617 (1997).

[156] Biryukov, A. S., Sukharev, M. E. & Dianov, E. M. Excitation of sound waves upon propagation of laser pulses in optical fibres. *Quantum Electronics* **32**, 765 (2002).

[157] Audouin, O. *et al.* Introduction of electrostriction-induced acoustic interaction in modeling of high-capacity long-haul transmission systems. *Selected Topics in IEEE J. Quantum Elect.* **6**, 297–307 (2000).

[158] Turitsyna, E. G. *et al.* The laminar-turbulent transition in a fibre laser. *Nature Photon.* **7**, 783–786 (2013).

[159] Avila, K. *et al.* The onset of turbulence in pipe flow. *Science (New York, N.Y.)* **333**, 192–6 (2011).

[160] Garnier, J., Lisak, M. & Picozzi, A. Toward a wave turbulence formulation of statistical nonlinear optics. *J. Opt. Soc. Am. B* **29**, 2229–2242 (2012).

[161] Picozzi, A. *et al.* Optical wave turbulence: Towards a unified nonequilibrium thermodynamic formulation of statistical nonlinear optics. *Physics Reports* **542**, 1–132 (2014).

[162] Barviau, B., Kibler, B. & Picozzi, A. Wave-turbulence approach of supercontinuum generation: Influence of self-steepening and higher-order dispersion. *Phys. Rev. A* **79**, 63840 (2009).

[163] Churkin, D. V. *et al.* Stochasticity, periodicity and localized light structures in partially mode-locked fibre lasers. *Nat. Commun.* **6**, 7004 (2015).

[164] Walczak, P., Randoux, S. & Suret, P. Optical Rogue Waves in Integrable Turbulence. *Phys. Rev. Lett.* **114**, 33–35 (2015).

[165] Randoux, S. & Suret, P. Experimental evidence of extreme value statistics in Raman fiber lasers (2012).

[166] Wabnitz, S. Optical turbulence in fiber lasers. *Opt. Lett.* **39**, 1362–5 (2014).

[167] Randoux, S. & Suret, P. Toward passive mode locking by nonlinear polarization evolution in a cascaded Raman fiber ring laser. *Opt. Commun.* **267**, 145–148 (2006).

[168] Boucon, a. *et al.* Noise-like pulses generated at high harmonics in a partially-mode-locked km-long Raman fiber laser. *Appl. Phys. B* **106**, 283–287 (2012).

[169] Luo, Z. Q. *et al.* Raman fiber laser harmonically mode-locked by exploiting the intermodal beating of CW multimode pump source. *Opt. Express* **20**, 19905–19911 (2012).

[170] Luo, Z. *et al.* Intermode beating mode-locking technique for O-band mixed-cascaded Raman fiber lasers. *Opt. Lett.* **40**, 502–505 (2015).

[171] Garbin, B., Javaloyes, J., Tissoni, G. & Barland, S. Topological solitons as addressable phase bits in a driven laser. *Nat. Commun.* **6**, 5915 (2015).

[172] Runge, A. F. J., Boderick, N. G. R. & Erkintalo, M. Observation of soliton explosions in a passively mode-locked fiber laser. *Optica* **2**, 36–39 (2015).

[173] Chouli, S. & Grelu, P. Rains of solitons in a fiber laser. *Opt. Express* **17**, 11776–11781 (2009).

[174] Chouli, S. & Grelu, P. Soliton rains in a fiber laser: An experimental study. *Phys. Rev. A* **81**, 63829 (2010).

[175] Gorbunov, O. a., Sugavanam, S. & Churkin, D. Revealing statistical properties of quasi-CW fibre lasers in bandwidth-limited measurements. *Opt. Express* **22**, 28071 (2014).

[176] Chamorovskiy, A. *et al.* 1.38-μm mode-locked Raman fiber laser pumped by semiconductor disk laser. *Opt. Express* **18**, 23872–23877 (2010).

[177] Menyuk, C., Levi, D. & Winternitz, P. Self-similarity in transient stimulated Raman scattering. *Phys. Rev. Lett.* **69**, 3048–3051 (1992).

[178] Kruglov, V. I., Peacock, A. C., Dudley, J. M. & Harvey, J. D. Self-similar propagation of high-power parabolic pulses in optical fiber amplifiers. *Opt. Lett.* **25**, 1753–5 (2000).

[179] Kivshar, Y. S. & Turitsyn, S. K. Vector dark solitons. *Opt. Lett.* **18**, 337–339 (1993).

[180] Kivshar, Y. Dark optical solitons: physics and applications. *Physics Reports* **298**, 81–197 (1998).

[181] Pang, M. *et al.* Stable subpicosecond soliton fiber laser passively mode-locked by gigahertz acoustic resonance in photonic crystal fiber core. *Optica* **2**, 339–342 (2015).

[182] von der Linde, D. Characterization of the noise in continuously operating mode-locked lasers. *Appl. Phys. B* **39**, 201–217 (1986).

[183] Smith, N. J. & Doran, N. J. Modulational instabilities in fibers with periodic dispersion management. *Opt. Lett.* **21**, 570–2 (1996).

[184] Conforti, M., Mussot, A., Kudlinski, A. & Trillo, S. Modulational instability in dispersion oscillating fiber ring cavities. *Opt. Lett.* **39**, 4200 (2014).

[185] Mamyshev, P. All-optical data regeneration based on self-phase modulation effect. In *24th European Conference on Optical Communication. ECOC '98 (IEEE Cat. No.98TH8398)*, vol. 1, 475–476 (1998).

[186] Papadopoulos, D. N. *et al.* Generation of 63 fs 4.1 MW peak power pulses from a parabolic fiber amplifier operated beyond the gain bandwidth limit. *Opt. Lett.* **32**, 2520–2 (2007).

[187] Plotski, a. Y. *et al.* Experiments on the generation of parabolic pulses in fibers with length-varying normal chromatic dispersion. *JETP Letters* **85**, 319–322 (2007).

[188] Abdullaev, F., Darmanyan, S., Kobyakov, A. & Lederer, F. Modulational instability in optical fibers with variable dispersion. *Physics Letters A* **220**, 213–218 (1996).

[189] Zhang, H., Xiao, H., Zhou, P., Wang, X. & Xu, X. Random Distributed Feedback Raman Fiber Laser With Short Cavity and Its Temporal Properties. *IEEE Photonic. Tech. L.* **26**, 1605–1608 (2014).

[190] Ravet, G., Fotiadi, A., Blondel, M. & Mégret, P. Passive Q-switching in all-fibre Raman laser with distributed Rayleigh feedback. *Electronics Letters* **40**, 528 (2004).

[191] Courant, R., Isaacson, E. & Rees, M. On the solution of nonlinear hyperbolic differential equations by finite differences. *Communications on Pure and Applied Mathematics* **5**, 243–255 (1952).

[192] Melnikov, L. A. & Mazhirina, Y. A. Dynamical model of Raman fiber lasers. In *Proc. SPIE*, vol. 9031, 903116 (2014).

Appendix: Examples of Spatio-temporal Dynamics

Below are the typical spatio-temporal pictures for simple cases: empty cavity (Figure A1), anomalous and normal dispersion fibre (Figure A2). The pictures were numerically generated using NLSE for one km long cavity. The fibre parameters were $\beta_2 = 56$ ps^2/km for normal dispersion, $\beta_2 = -10$ ps^2/km for the anomalous, and $\gamma = 3$ (W$\cdot$ km)$^{-1}$ for both cases. The fibre was set to have zero losses and zero gain for simplicity. Figure A3 is the spatio-temporal dynamics of an IPG Raman pump laser which was used in the experiments, with no particular features present.

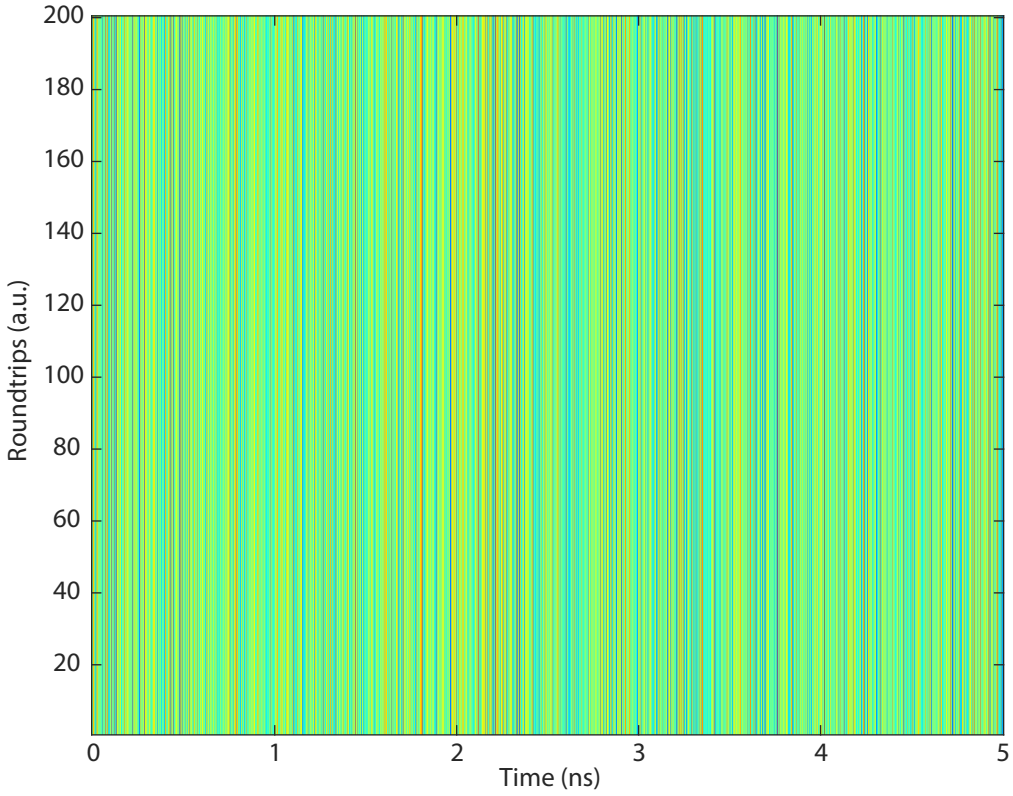

Figure A1: The spatio-temporal picture of a continuous wave with 20 dB Gaussian noise propagating between two ideal mirrors, without dispersion or nonlinearity.

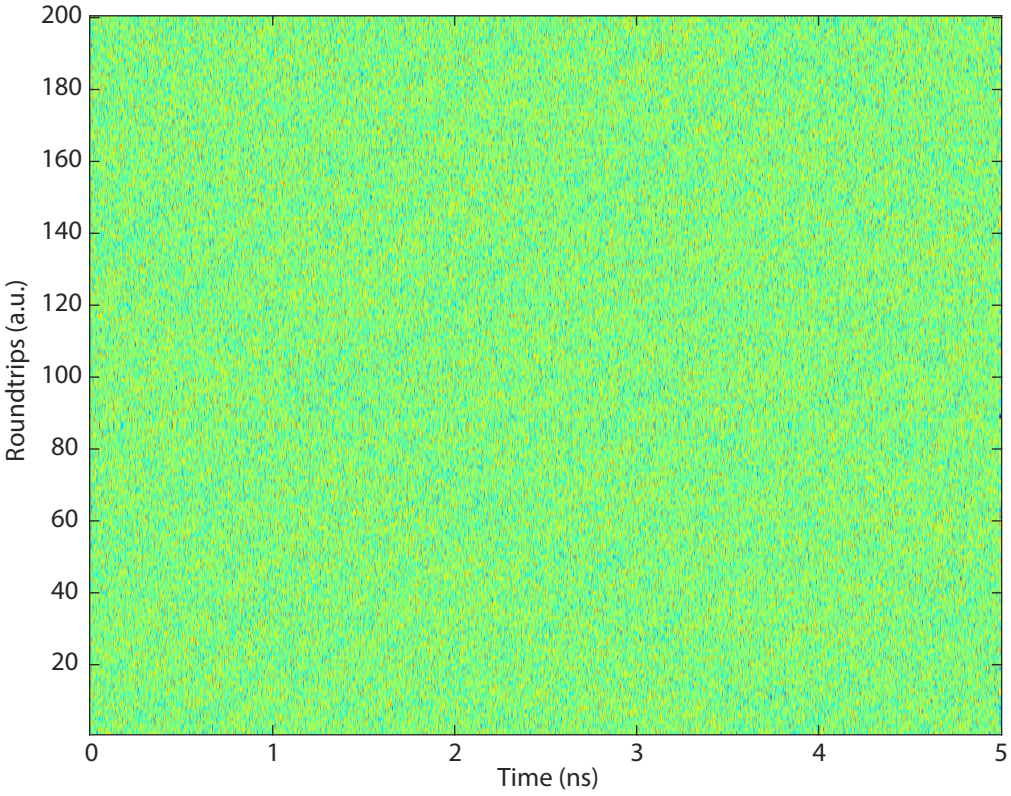

Figure A2: The spatio-temporal picture of a continuous wave with 20 dB Gaussian noise propagating between two ideal mirrors, in an optical fibre. The picture is similar for both normal and anomalous dispersion.

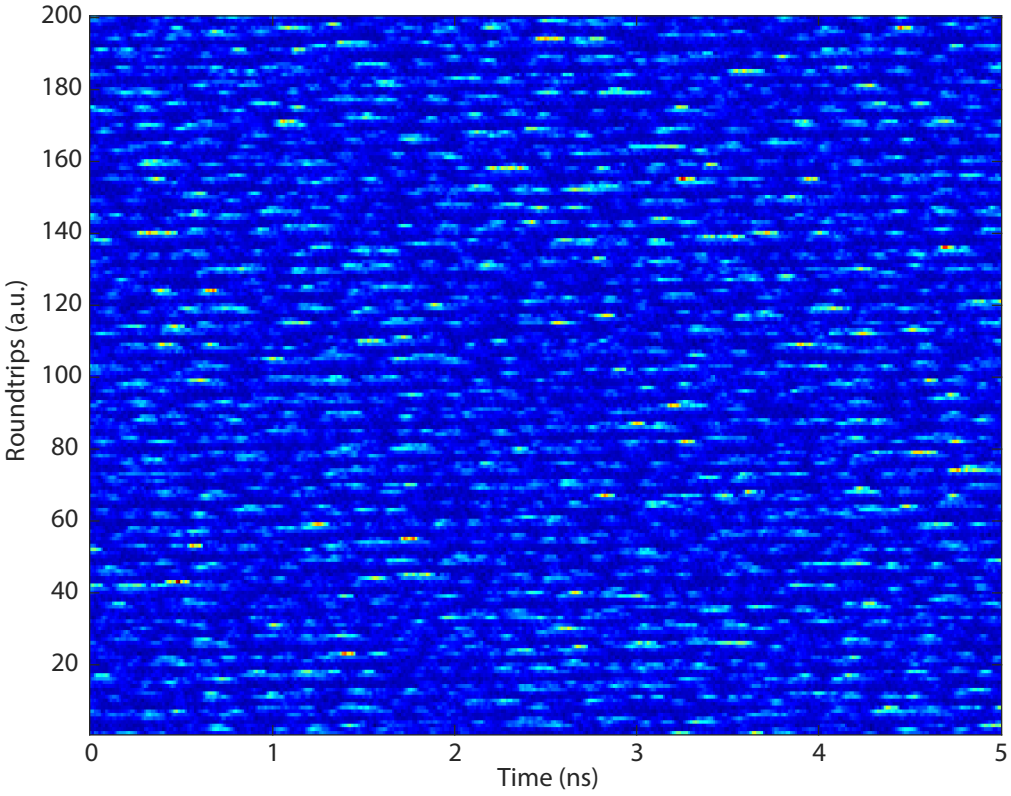

Figure A3: The spatio-temporal picture of the stochastic radiation from an IPG Raman pump laser.